FREQUENCY DOMAIN METHODS FOR PREDICTING THE TRANSPORT OF NON-UNIFORM FLOW THROUGH TURBOMACHINERY COMPRESSORS

by

Matthew D. Small

Thesis Submitted to the Faculty of the
Virginia Polytechnic Institute and State University
in partial fulfillment of the requirements for the degree of

MASTER OF SCIENCE
in
Mechanical Engineering

APPROVED:

_____

W.F. O'Brien, Committee Chair

_____ _____

P.S. King C.L. Dancey

May, 2001
Blacksburg, Virginia

Frequency Domain Methods for Predicting the Transport of Non-Uniform Flow Through Turbomachinery Compressors

by

Matthew D. Small

Committee Chair: W. F. O'Brien

Mechanical Engineering

(ABSTRACT)

A new method to predict the transport of non-uniform total pressure distributions through an axial flow compressor is presented. The method relies on frequency-domain transformations of total pressure distortion patterns, and the use of digital filter techniques to capture the effect of a blade row on the total pressure distortion. Compressor characteristics, described by a frequency response function, are obtained from experimental data and are related to fundamental blade row flow phenomena. When excited by a total pressure distribution with unknown response, the blade row's frequency response function can serve to predict the downstream total pressure profile.

This work covers the application of frequency response functions for turbomachinery blade rows, and includes the development of a process that improves the capability of linear response functions to model nonlinear flow behavior. The process is empirically based and relies on several original correlation parameters. Developed frequency domain modeling methods are applied to a rotor of modern design with promising results.

ACKNOWLEDGEMENTS

I would like to thank my graduate committee for serving in this capacity. Particular acknowledgement is due to Dr. O'Brien; without whose enthusiasm for turbomachinery I would never have come to Virginia Tech.

Dr. Doug Rabe of the Compressor Research Facility (CRF) at Wright- Patterson Air Force Base deserves special thanks for funding this project. Carl Williams, also of the CRF, was instrumental in providing experimental data sets in a timely and efficient manner.

The support of Chunill Hah of NASA's Lewis Research Center is appreciated for providing numerical solutions of the rotor flow field for comparison.

A thanks goes to the undergraduates and exchange students who have assisted me with often tedious and repetitious portions of this work; Carter Shields, Jason Gilley and Phil Crowle.

Thanks to Maj. Keith Boyer, USAF, for providing data from SLCC runs.

The camaraderie and friendship of everyone in the Turbolab is greatly appreciated and has made the thousands of hours spent in the basement of Randolph pass agreeably as though they were merely several hundred. Thank-you Dr. King, Alexandre, Drew, Grant, Joe, Jon, Karl, Keith, Mac, Scott and Wayne.

Finally, an especially heartfelt thanks goes to my parents and brother. Without their guidance and support I would not have had the will to attempt this project, the strength of character to finish it, or be journeying toward such an expansive and vibrant horizon.

TABLE OF CONTENTS

LIST OF FIGURES

LIST OF EQUATIONS

LIST OF TABLES

1 Introduction

Early design and analysis methods for turbomachinery compressors traditionally relied on the assumption of axisymmetric flow upstream of the compressor. This flow condition allows for circumferentially uniform aerodynamic and structural loading of blade row airfoils. However, by the mid 1960's the limitations of this assumption were becoming increasingly apparent as the performance of gas turbine engines and the aircraft they powered were being pushed to greater extremes than ever before. New flight conditions and airframe configurations began to create strongly nonuniform time dependent flow conditions at the engine inlet. The performance requirements of modern propulsion systems continue to make non-uniform engine inlet flow an operational reality. Aggressive aircraft maneuvers and sustained supersonic flight combined with serpentine inlet geometry, wake ingestion from forward airframe components, and armament firing are some of the phenomena that can produce non-axisymmetric engine inlet flow conditions. These conditions affect both the thermodynamic performance of the compressor, in terms of its pressure and temperature ratios and efficiency, as well as its mechanical operation, through the possible excitation of blade vibrational modes.

Compressor operation with distorted inlet flow typically results in decreased thermodynamic performance. Decreases in pressure ratio and efficiency, compared to that of operation with uniform flow, are accompanied by a loss of stall margin. Stall margin reduction with increasing distortion intensity is shown as a percentage of design stall margin in Figure 1.1. If stall occurs, the compressor looses its ability to maintain design pressure ratio, which can lead to the condition of engine surge, characterized by flow reversal and possible engine flame-out. Note also that increased distortion intensity, as a percentage of inlet average total pressure, decreases the available pressure ratio at a given mass flow.

When combined with other destabilizing factors, the reduction in stall margin due to distortion becomes significant. Figure 1.2 shows some of the many phenomena that affect the stalling behavior of a compressor. Note that these factors tend to drive the stall line toward the operating line.

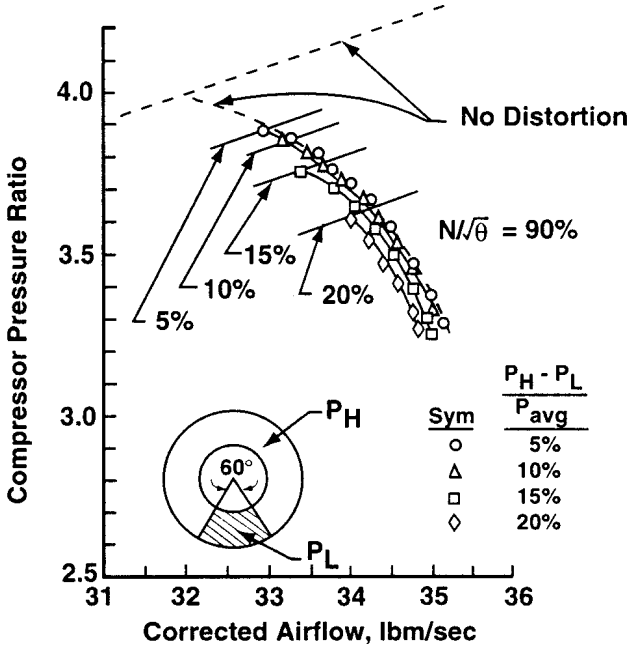

Figure 1.1: Effect of Distortion on Compressor Performance Map (Kimzey, 1977)

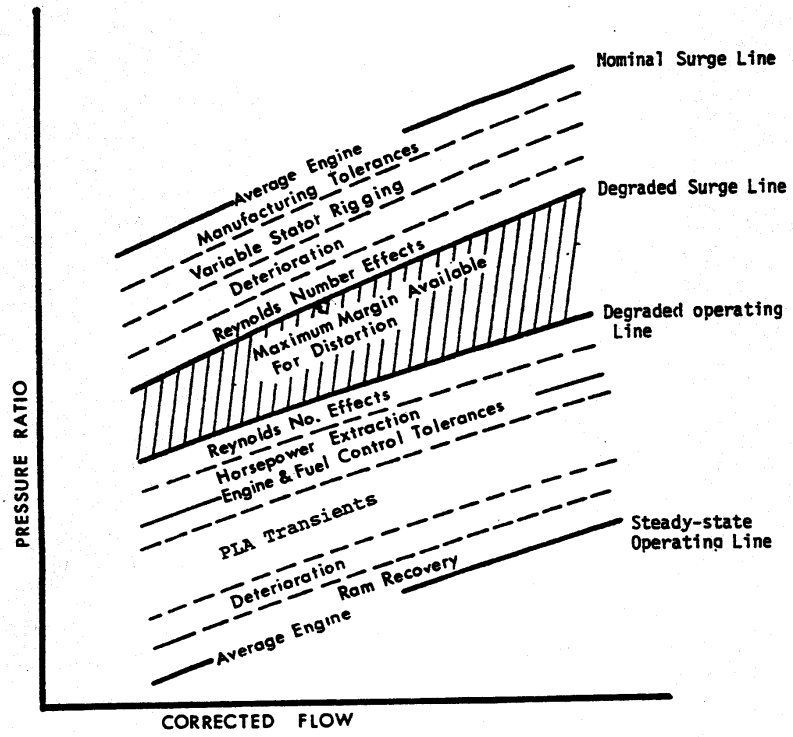

Figure 1.2: Compressor Destabilizing Factors (SAE, 1999)

Mechanical damage can also be caused by the excitation of blade vibrational modes. Typically this is a concern for rotor airfoils since their relative motion, when combined with annular flow nonuniformity, create a periodic driving function which can excite component airfoils. However, stator vanes are not immune to this problem and can be driven by both downstream convecting wakes and upstream propagating potential and acoustic forcing functions. When combined with thin, transonic blade geometry and reduced damping at the rotor hub caused by modern integrally- bladed disks, or “blisks”, blade row airfoil high cycle fatigue (HCF) becomes a significant problem. The prediction of blade row forcing functions and the resulting mechanical response has become an area of active research.

The relationship between blade mode, rotor speed and excitation frequency is often illustrated on a Campbell Diagram. One such diagram is shown in figure 1.3a. Excitation frequency is plotted versus rotor speed and overlaid with lines of constant “per-rev” forcing functions- caused by a given number of disturbances per rotor revolution. The intersection of these lines with blade mode lines (1F- first flex, 2F- second flex, 1T-first torsion, 2S- second stripe) shows combinations of rotor speed and forcing function at which blade vibrational modes are excited. As shown in figure 1.3b, increased distortion intensity causes a corresponding increase in resulting vibratory stress. Improved understanding of distorted flow behavior is critical to controlling HCF.

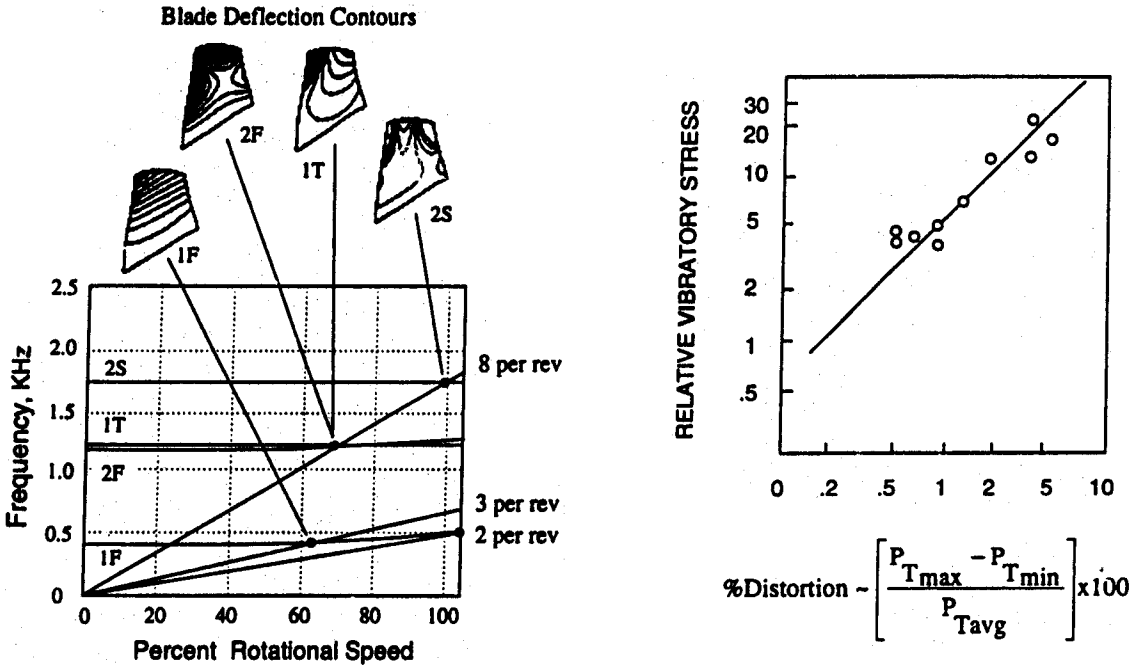

(a) (b)

Figure 1.3: Campbell Diagram (Manwaring et al.,1996) and Blade Vibration Amplitude Variation with Distortion Intensity (Danforth, 1975)

Methods to predict the behavior of circumferential nonuniform flows in turbomachines were originally focused on thermodynamic performance calculations, as a means of avoiding stall and surge. Although a given distortion profile can affect both thermodynamic and mechanical performance, the maximum response of both performance parameters are driven by different kinds of nonuniformities. Figure 1.4 shows the divergent effects of different distortions on compressor cycle performance and blade excitation. Low engine order distortion produces the greatest effect on available pressure rise, while typically higher engine order patterns are required to excite blade modes.

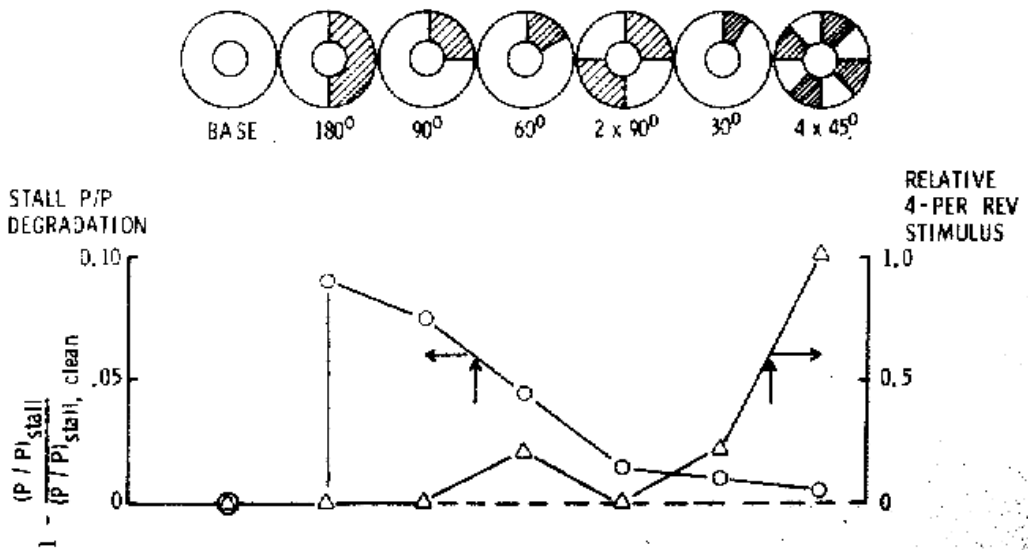

Figure 1.4: Divergent Effects of Distortion on Stall Margin and HCF Excitation (Danforth,1975)

As HCF prevention becomes more important, methods to predict the fluid dynamic drivers in modern transonic compressors are required. Current computational fluid dynamics (CFD) techniques are in their infancy, require vast computational resources and are slow to converge. There remains a need for a quick, easily applied and accurate method to predict nonuniform total pressure behavior through blade rows.

This work presents a method that predicts the transport of nonuniform flow through a compressor rotor of modern design. Investigations of two kinds of frequency domain models are presented, and their abilities investigated. A method is developed with general applicability to the inherently nonlinear flow in axial turbomachinery compressors. The method utilizes an empirically derived frequency-domain technique and includes “tuning” of the model to allow prediction of operating conditions dissimilar to those from which the model was derived. Accuracy of the model’s nonuniform total pressure predictions is good, and shows signs of robustness.

2 Literature Review

Experimental and analytical research into compressor response to distorted flow has an extensive history. The effects of numerous steady and time dependent pressure and temperature distortions on compressor and gas turbine performance, stability and mechanical integrity have been investigated for over forty years. Despite this, the "problem" of distorted inlet flow still exists. Modern performance and operating requirements have increased the sensitivity of propulsion systems to off-design flow conditions of both temperature and pressure. This study concentrates on steady, annular total pressure distortions and their effect on compressor blade row aerodynamic and mechanical response.

Total pressure distortion at the engine (compressor) inlet in flight takes many forms including symmetrical and asymmetrical patters. Figure 2.1 shows measured patterns that were designed to simulate operational conditions.

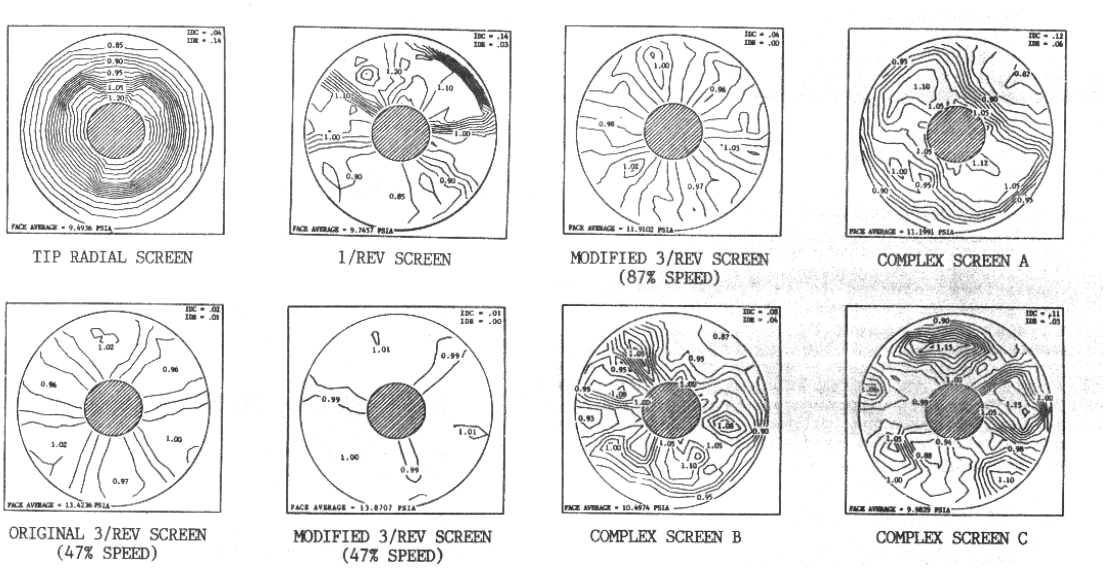

Figure 2.1: Distortion Screen Generated Total Pressure Distortions (Datko et al. 1987)

A traditional, and still widely used, technique of generating total pressure distortion upstream of a test compressor or engine has been through the use of distortion-generating screens. Typically these are wire mesh screens of varying porosity and

produce steady total pressure nonuniformity. Screens to reproduce complex distortion patters like those shown in figure 2.1 have been constructed. Distortion screens are often configured to create circumferential distortion patterns. These are characterized by regions of radially uniform distortion intensity distributed about the circumference in sectors. A circumferential screen with a single distorted sector with an extent of approximately 110^0 is illustrated in figure 2.2. Circumferential distortion patterns are widely used for both performance and aeromechanical studies.

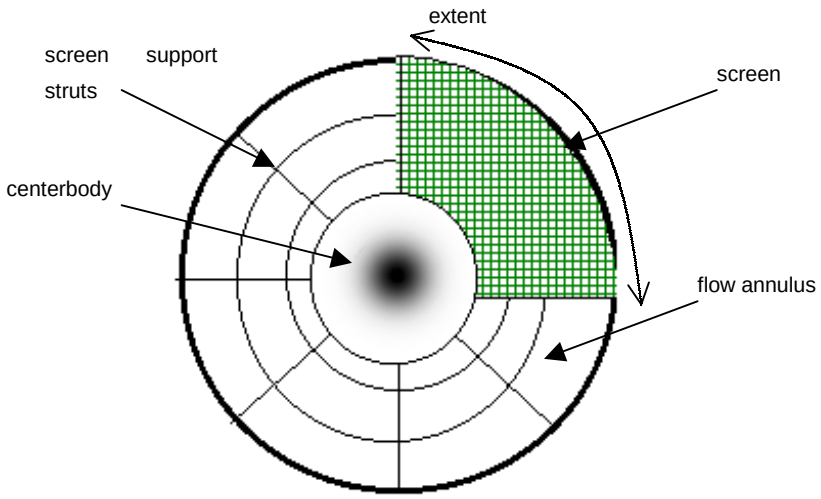

Figure 2.2: Example Circumferential Distortion Screen

Literature for this survey is grouped into four categories: The initial category includes cited references giving an overview or qualitative analysis of engine and compressor flow distortion issues. This is followed by two categories; one each for experimental and analytical studies of distorted flow in compressors and a final section reviewing work directed specifically toward high cycle fatigue.

2.1 Overview of Distortion Concerns for Aeromechanical and Aerothermal Compressor Performance

As early as the mid 1970's, the divergent requirements of thermodynamic and aeromechanical performance as they relate to distorted inlet conditions were being

recognized. Danforth (1975) examined several mechanisms that could possibly excite blade vibration, including that induced by circumferential distortion and its harmonic content. He questioned the ability of stall-related distortion indices and test programs to fully capture blade row HCF response, the divergent requirements of which are shown in figure 1.4. He argued that increased inlet measurement spatial resolution, over that required for stall, is needed to fully describe inlet blade row forcing functions. He suggested the use of five radial immersions and the measure of the first eight component frequencies (minimum of 16 circumferential stations) to capture inlet excitation flows. Recently, Ludwig (1999) proposed the use of 16 circumferential stations as well, but with only two radial immersions. The document governing compressor distortion testing, Society of Automotive Engineers Aerospace Information Report (SAE AIR) 1419, originally issued in 1983, was developed for stall and surge investigation. It recommends the use of eight circumferential probes containing five radial immersions each. It is widely recognized that this is inadequate for HCF studies.

Greitzer et al. (1994) examined the effect of distorted flow on compressor aeromechanical excitation and overall compression system instability. They separated distorted flows into three groups corresponding to the length scale of the disturbance.

"Small" length scale disturbances- at least an order of magnitude smaller than the pitch or chord dimension- are associated with wake and boundary layer turbulence. "Large" scale phenomena include low engine order forced vibration, rotating stall and surge, whose characteristic lengths are approximately an order of magnitude larger than a blade passage. According to Greitzer et al., the impact of both of these length scale disturbances on performance is well understood and documented. However, the impact of disturbances with a "medium" characteristic length scale- on the order of circumferential blade spacing- is less well known. These disturbances include upstream potential effects, wake velocity distributions, and tip clearance vortices.

Aeromechanical response can be exited by disturbances of both medium and large length scales. Although the present frequency-domain study is performed using large length scale disturbances, the method developed is not inherently restricted to this length scale. Medium length scale total pressure disturbances can also be investigated; the data

used here simply did not contain any higher engine order phenomena of significant magnitude.

Greitzer et al. also noted that since the late 1960's several hundred failure incidents of varying severity have occurred in U.S. Air Force aircraft engines. The cause of most of these incidents was attributed to high cycle fatigue, the high frequency vibratory excitation of blade row airfoils. Furthermore, while dynamic blade stress can be predicted with current methods, they contended that prediction of aerodynamic forcing functions is not mature. Compounding the problem is poor understanding of blade aerodynamic and mechanical damping.

In a seminal work, Reid (1969) examined the effect of sector configuration and extent on the stability of a six-stage test compressor. Figure 2.3 illustrates the detrimental effect on compressor surge pressure ratio caused by increasing the extent of the distorted sector. A “critical angle” is also shown, beyond which the surge margin is not affected by further increases in sector width. The concept of a critical angle, and the resulting nonlinearly, is attributed to a time dependent blade response. Thus, the critical angle is that which provides sufficient rotor “dwell time” in the distorted region for the blade response to be maximized.

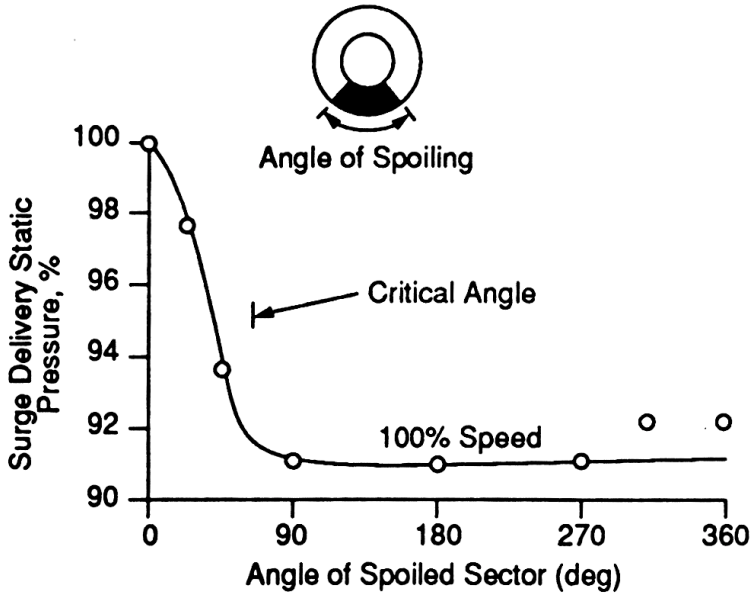

Figure 2.3: Effect of Spoiled Sector Width (Reid, 1969)

This effect is also seen in figure 2.4, which shows the effect of multiple sectors on surge margin. It is seen that it is the extent of an individual sector (and thus the corresponding dwell time) and not the total spoiled area that is causing surge margin reduction. Although each case has a total of 90^0 of distortion, the sector with the largest continuous distortion causes the greatest reduction in surge margin.

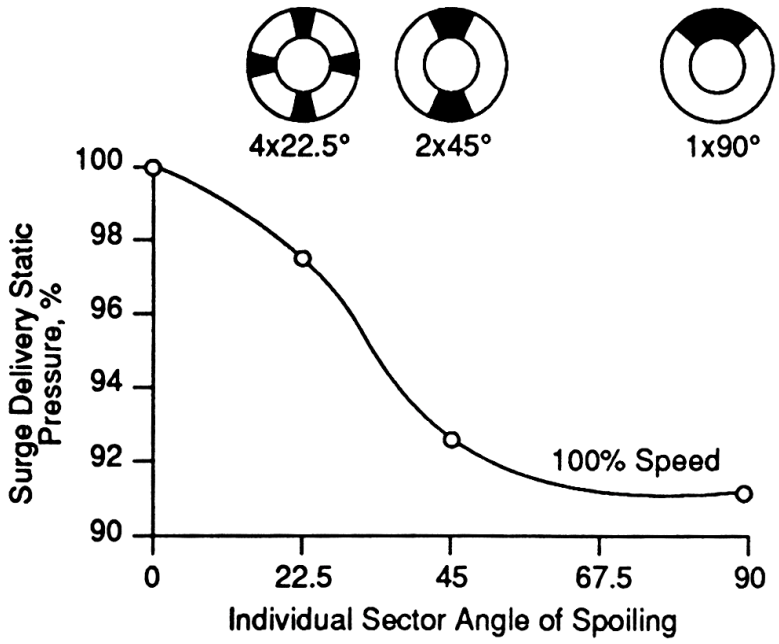

Figure 2.4: Effect of Contiguous Spoiled Sector Width (Reid, 1969)

Longley and Greitzer (1992) provide a summary of two of the most widely used distortion indices, which describe the extent of a given distortion. What they term the "K" series has many variations and is typically referred to as *reduced frequency*. In general, this parameter gives a ratio between rotor dwell time and blade response time. Thus values larger than 1 would indicate maximal response, while lower values would suggest that the distortion extent is smaller than the critical angle. The other parameter reviewed is known collectively as the "DC" distortion indices. These are identical to the "K" indices in most respects. Instead of using each distorted sector to define the distortion, the sector of a given extent with strongest intensity is used.

With some of the fundamental concepts of distorted flow in turbomachinery outlined, including typical distortion patterns and distortion screen configurations, characterizing parameters and typical operational effects, the next section presents a survey of modeling methods.

2.2 Review of Aerodynamic Performance Experimental Studies

A large number of experimental investigations into the effect of distortion on compressor performance (both thermodynamic and mechanical) have been undertaken in the past four decades. Many of these were performed with the aim of developing correlations between the severity (variously defined) of a given inlet distortion and the resulting reduction in surge margin.

In an early study by Ashby (1957) the wake of a ¼ inch diameter rod was measured both upstream and downstream of a subsonic rotor. The subsequent impact on velocity diagrams was studied, using both isolated and staged rotors at several different mass flow rates. He found that the greatest attenuation of the total pressure distortion due to the rod wake occurred when the angle between the relative and absolute velocity vectors (at either the inlet or outlet) was ninety degrees.

Graber et al. (1974) used both distortion- generating screens and airjets to induce circumferential total pressure distortions upstream of a single spool turbojet and a double spool turbofan. The effect of various combinations of distortion intensity and extent were investigated. Seven surge and stall correlation indices were examined and it was found that the parallel compressor theory could predict the engine's surge point well.

Peacock and Overli (1976) installed distortion screens upstream of a single stage low speed compressor to induce square and sine wave distortions. Three main areas were investigated, the rotor's influence upstream influence on the distortion, performance degradation and resulting blade surface unsteady pressures. They found that a square wave screen did not produce a purely square wave distortion, instead finding the distortion pattern shown in figure 2.5 downstream of the screen. Note that the sharp edges of the square wave have been smoothed by leakage around the edges the screen and

downstream blockage from stalled blades. (Circles show measured total pressure and triangles represent static pressure measurements.) This is typical of distortion- generating screens and needs to be considered when designing a screen to create a desired pattern. Like Reid, Peacock and Overli found that breaking a distorted sector into multiple sectors reduced the effect of the distortion on the compressor's pressure rise.

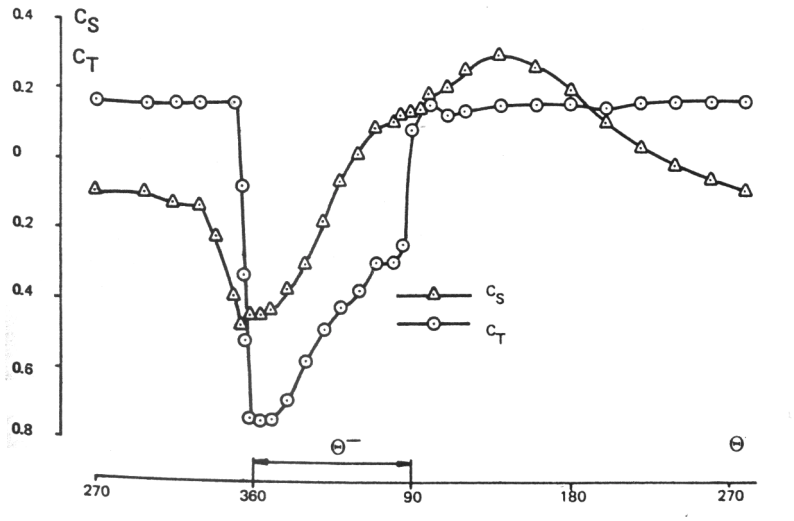

Figure 2.5: Pressure Distribution Downstream of Square- Wave Screen, (Peacock and Overli, 1976)

Additionally, to quantify blade surface pressure values, Peacock and Overli defined an instantaneous normal force coefficient

$$C_n = \frac{\int_{x=0}^{x=c} p\, dx}{(1/2\rho V^2)_\theta}$$

Equation 2.1

where c= chord
p= static pressure
ρ= density
V= inlet relative velocity
θ= avg. about circumference

They found that as a blade passed into a distorted region there first was a drop in C_n, which was followed by a sharp increase in incidence and a correspondingly sharp

increase in Cn. This transient behavior did not follow steady state behavior, but instead showed a 100% increase in Cn over that recorded for steady incidence angles. This is shown in figure 2.6 for incidence angles from –10 to 30 degrees.

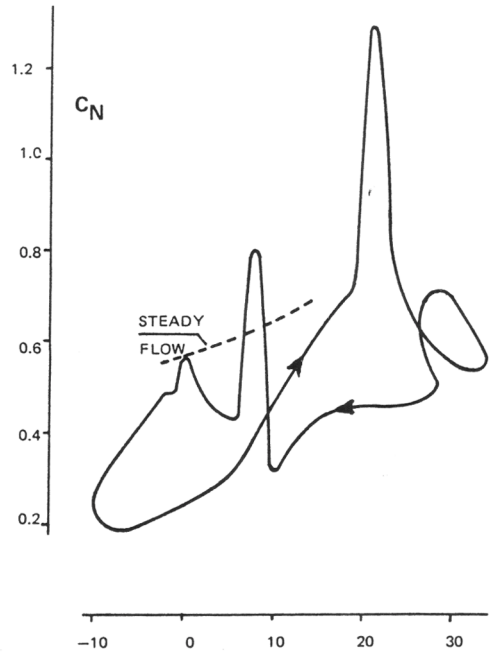

Figure 2.6: Unsteady Variation in Cn versus Incidence Angle, (Peacock and Overli, 1976)

Colpin and Kool (1978) examined the propagation of a circumferential distortion of 90-degree extent through a single stage subsonic rotor. A significant finding from this study was that the gradient of the inlet relative flow angle had a large influence on blade row behavior. This is one of the first experimental programs to indicate that a distortion descriptor should include information about the rate of change of the upstream distortion.

Yocum and Henderson (1980) measured the flow field upstream and downstream of an isolated rotor operating in the subsonic regime with various geometrical configurations and inlet flow distortions. The facility had a secondary fan that created flow through the test section without the compressor rotor installed. This test configuration was used to make measurements of the distortion profile and thereby determine the effect of the rotor on the upstream distortion pattern. The first fifteen component frequencies of a four per rev distortion with and without the rotor installed is

shown in figure 2.7. (A_n = amplitude of n^{th} frequency component) Location 1-D is rotor inlet and location 15 is rotor exit. Note that there are significant differences in the harmonic content between the installed and uninstalled cases for both total pressure and velocity distributions.

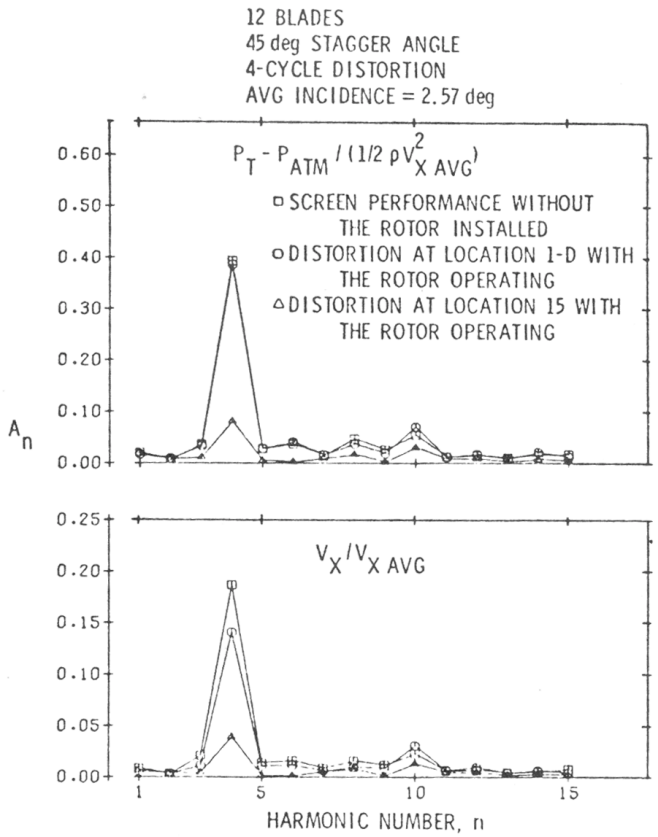

Figure 2.7: First Fifteen Component Frequencies of Total Pressure and Velocity Forcing Functions Caused by a Four/Rev Distortion, (Yocum and Henderson, 1980)

With the test rotor installed and operating, circumferential measurements of rotor inlet and outlet axial velocity and total pressure were made to examine distortion attenuation for various values of incidence and stagger angle and blade loading. It was found that stagger angle had the strongest influence on distortion attenuation, which was also a function of the ratio of blade spacing to distortion wavelength. They note that any unsteady blade response models should not use unsteady isolated airfoil analysis, since this will not capture the blade spacing/ distortion wavelength phenomenon.

Andrew (1988) measured dynamic total pressure and velocity in the rotor blade passage of a single stage subsonic compressor operating with distortion- induced rotating stall. He found that isolated airfoil theory could be applied to blade rows, provided that the blade spacing was not too fine. Results indicated that isolated airfoil theory was extendable to a rotor with solidity of one.

Kaya et al. (1993) studied the flow field of a variable pitch rotor operating with screen induced distortion of thirty-degree extent. They found that greater distortion attenuation occurred when the blades were scheduled to produce high aerodynamic loading.

2.3 Review of Aerodynamic Performance Modeling Studies

The use of accurate, applicable models in lieu of engine testing often reduces development time and required hardware, resulting in large cost savings. Model development is advantageous because it often requires developing an insight into the behavior of the physical system under consideration. Improved understanding of the underlying physical phenomena can lead to improvements in the system that otherwise would not have been possible.

The majority of modeling studies reviewed here were developed specifically for prediction of performance degradation due to distorted inlet flow. The prevailing distortion types are very low engine order, often with distortions of only one or two cycles per revolution. While these low frequency distortions strongly affect the compressor's aerodynamic performance, generally it is forcing functions with higher frequency content that are of concern for high cycle fatigue.

The archetypal technique for modeling compressor fluid response to non-uniform flow is the parallel compressor model, originally developed by Pearson and McKenzie (1959). Used to model performance degradation caused by circumferential distortions, the model relies on five assumptions: 1) the distorted compressor consists of two or more independently operating sub-compressors, 2) all sub-compressors have individually uniform inlet conditions and operate on the undistorted compressor characteristic, 3) no

circumferential cross- flow exists between sub-compressors, 4) exit static pressure of all sub-compressors is equal, 5) the entire compressor stalls when an individual compressor reaches the undistorted stall pressure ratio. A diagram of this approach for a single distorted region is shown in figure 2.8.

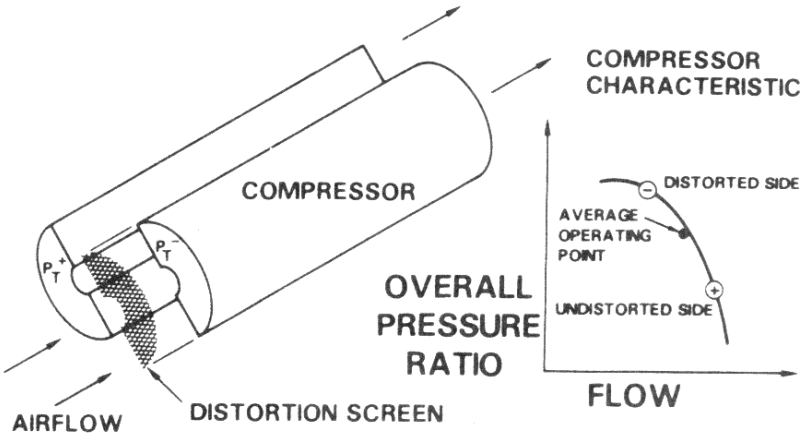

Figure 2.8: Parallel Compressor Model for Single Distorted Sector, (Reid, 1969)

A further assumption is implied by condition two. For each sub-compressor to have uniform inlet conditions, the blade rows of the real compressor must respond instantaneously to a disturbance. This non-physical requirement, and others, have been impetuses for many improvements and modifications to the technique.

Braithwaite et al. (1973) used a simplified parallel compressor technique to model the behavior of a single 180^0 extent circumferential total pressure distortion through a eight stage compressor. Simplifications included the assumption of uniform compressor exit total pressure. The model did a good job predicting the distorted stall pressure ratio for constant corrected speeds.

Roberts et al. (1968) found that the parallel compressor model did not predict the change in shape of the distortion as it passed through successive stages. The model was quite poor in this regard, since it inherently always predicts a square wave distortion

pattern, figure 2.9. They attributed this to neglecting circumferential cross flows, a required assumption if using an unmodified parallel compressor model.

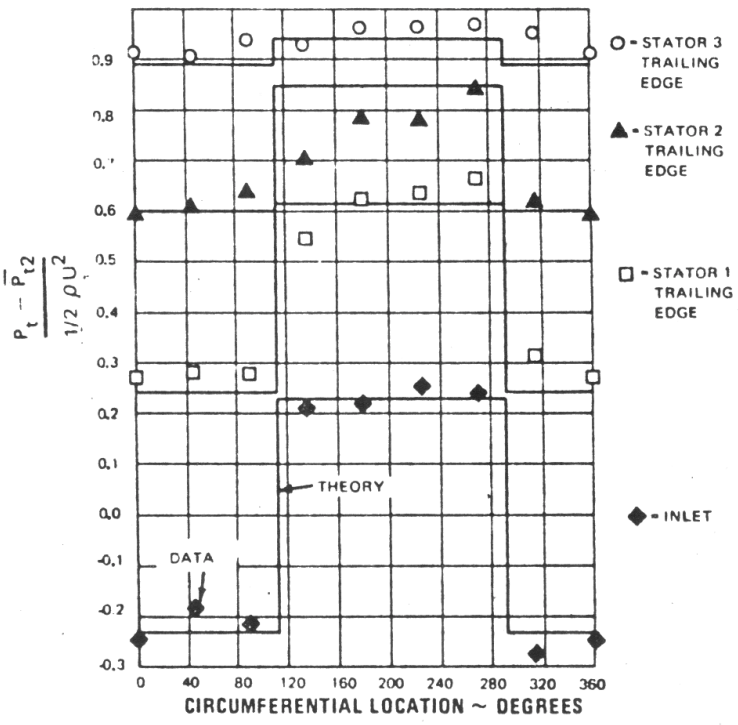

Figure 2.9:Experimental Data and Parallel Compressor Prediction (Roberts et al., 1968)

In addition, Roberts et al. investigated blade time response to a disturbance, also seen by Reid, by varying rotor and stator chord lengths in the test compressor. They found that the compressor was most tolerant to distortion when the rotor was fitted with blades having a longer chord. This suggests a time lag between distortion initiation and maximum blade response, most likely caused by the downstream convecting disturbance taking a finite time to propagate through the blade passage. It was seen that the model did a better job predicting the behavior of shorter chord blading; blades whose response more closely approximates the instantaneous response assumed by the parallel compressor model.

Blade time response to distortion was quantified by Roberts et al. using the reduced frequency parameter, which they defined by equation 2.2.

$$k = \frac{B \cdot \Omega}{V}$$

Equation 2.2

where

k= reduced frequency
V= average velocity of the air relative to the rotor
B= one half of the rotor chord length
Ω= Frequency of the circumferential disturbance with a window of periodicity of one revolution (rad/sec)

Note that blade response and reduced frequency are inversely proportional. For example, low values of reduced frequency (perhaps due to high fluid velocity) indicate increased rotor response (caused by the distortion quickly propagating through the blade row).

Many variants of the reduced frequency parameter have been developed. The version developed by Mikolajczak and Pfeffer (1974) is defined in equation 2.3

$$k = \frac{b}{r} \cdot \frac{360}{\theta} \cdot \frac{U}{V_m}$$

Equation 2.3

where

b= axial projection of the rotor chord
r= compressor radius at the blade section
θ= distortion extent in degrees
U= tangential blade speed
V_m=mean axial air velocity

Bruce (1979) proposed yet another definition.

$$k = \frac{\upsilon C}{2 V_m}$$

Equation 2.4

where

υ= distortion frequency, υ= (2πU/L)
U= tangential blade speed
L= distortion wavelength

C= rotor chord length
V_m=mean axial fluid velocity

This representation is very intuitive and is illustrated in figure 2.10. A square-wave disturbance (solid line) is shown in the time domain and is overlaid with the response of blades (dashed lines) with two different fluid transport (response) times. Note that the blade with the shorter response time, relative to the time spent in the distorted sector, has a greater response than that with the longer response time.

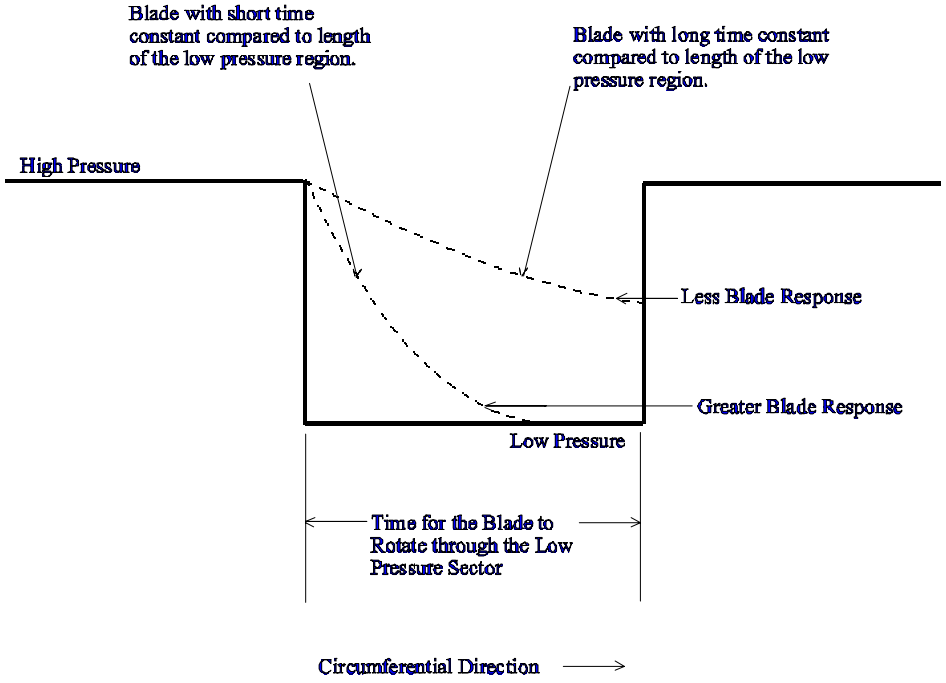

Figure 2.10: Blade Response Time (Howard, 1999)

Knowing that the blade response is time dependent, much work has been done to account for this in compressor models. One early effort is by Carta (1972) who used isolated airfoil data to empirically correlate time dependent flow with rotor performance. The method employed was, for a given (time dependent) angle of attack, to look up lift and drag coefficients from a table of unsteady airfoil data with were then used to compute circumferential total pressure and temperature distributions. He decided this was not an optimal approach, and consequently abandoned it.

Another approach that relied on unsteady cascade data is that of Kimzey (1977). Instead of assuming that the lift coefficient to angle of attack relationship in a compressor with time dependent inlet flow (Kimzey was working with time varying mass- averaged inlet flows) is the same as that for steady flow, a first order lag equation was used to relate dynamic lift to steady state data. However, his approach is one-dimensional and therefore cannot model circumferential distortions.

Barr (1978) developed a method based on an unsteady cascade approach that is applicable to distorted flow. Fundamental flow equations were developed for incompressible, inviscid flow through blade rows. Resulting downstream total pressure profiles are related, using an energy method, to the unsteady circulation around (and therefore the lift of) blade row airfoils.

Adamczyk (1974) improved the original parallel compressor model by allowing for 1) circumferential variation in static pressure at the exit, 2) time dependent flow through both the rotor and stator blade rows and 3) large amplitude distortions. The model divides the flow into two regions: that interior to the blade row and that upstream and downstream of the blade row. The intrablade flow model allowed for time dependent flow and included the effects of cascade loss and turning. Interblade flow was modeled as inviscid and incompressible with no radial variations. A lack of experimental data prevented direct comparisons of model predictions with measurements. Adamczyk claims that the results show good qualitative agreement with available data.

Mazzawy (1977) took a more radical approach to improving the parallel compressor model by replacing the sub-compressors with multiple pseudo-streamtubes. The result was increased circumferential resolution as well as a reduction in the number of restrictions from five, in classic parallel compressor theory, to one. The only restriction Mazzaway placed on this model was that the distortion's circumferential extent spans several blade passages. This precludes the use of this model for higher engine order excitations, making it of limited use for HCF work. Although the resulting model did a good job of predicting compressor performance and downstream total pressure profiles. To model the blade time response to distortion Mazzawy used a first-order decay equation with an empirically derived time constant. This is an important improvement over classical parallel compressor theory, which assumes instantaneous blade response.

The resulting downstream total pressure profiles, figure 2.11, were of higher fidelity than those from the simpler model of Roberts et al., figure 2.9.

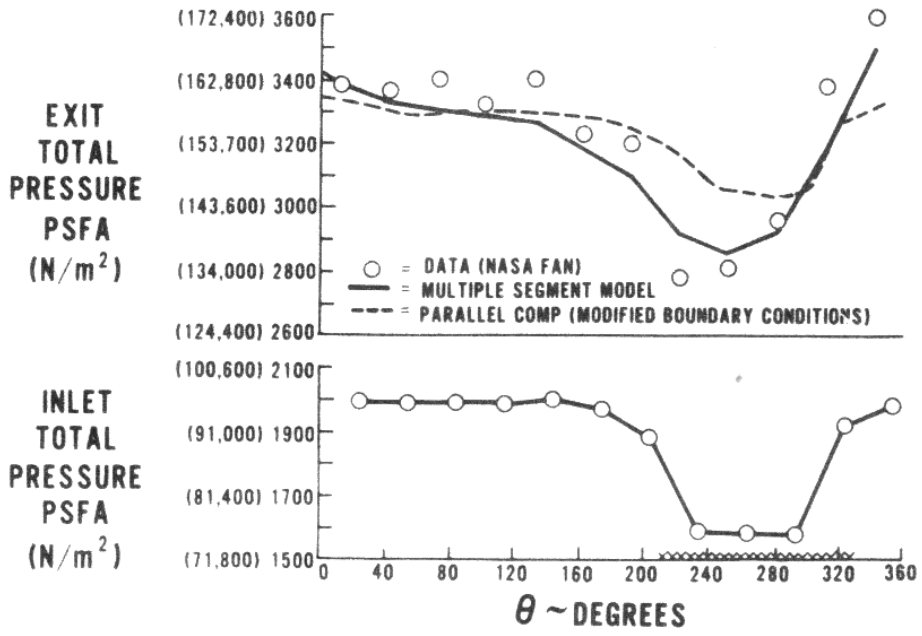

Figure 2.11: Experimental Data and Modified Parallel Compressor Prediction, (Mazzaway, 1977)

Melick (1973) combined parallel compressor theory with a time dependent lift coefficient. He postulated that a given value of lift was a function of the instantaneous angle of attack (AOA), the inertia of the fluid's mass surrounding the blade and trailing edge vortex shedding. The resulting model was analogous to a damped mass/ spring system; the lift coefficient being described by a second order equation whose two time constants were determined empirically. A search of published experimental data indicated that the two constants were equal to each other.

Lecht (1986) furthered this work by incorporating the concept of lift overshoot, the phenomenon of an airfoil momentarily exceeding its maximum lift coefficient without stalling, into the model. The model did a good job predicting the pressure rise, mass flow characteristic of two single stage transonic compressors operating with single sector circumferential distortion.

The approach taken by Melick and Lecht defined a time domain transfer function (exponential decay) between the steady state and effective angle of attack. This is

illustrated in figure 2.12a, where the actual step input is compared to the "path" of the effective input. The resulting function acts on an input, figure 2.12b, to change a continuous ramp in angle of attack to an output (actually the resulting blade input AOA) that more closely follows the blade response.

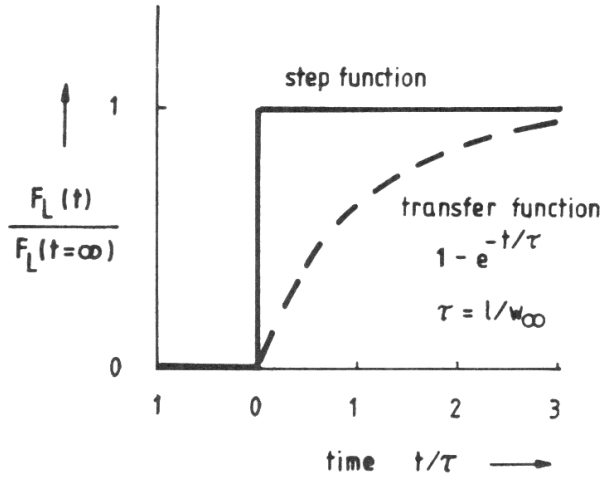

Figure 2.12a: Exponential Decay Transfer Function, (Lecht, 1986)

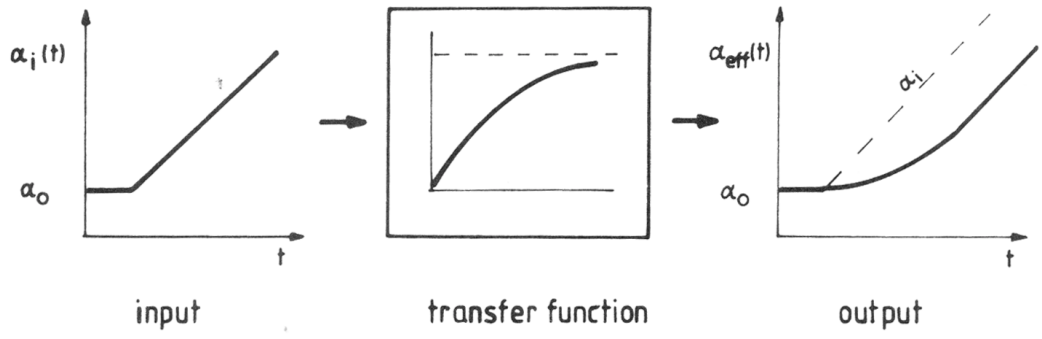

Figure 2.12b:Transfer Function Defines Effective AOA for a Given AOA, (Lecht, 1986)

Andrew (1988) used the Melick model to examine the effect of reduced frequency on distortion attenuation. He defined yet another version of reduced frequency as

$$k = \frac{c/V}{\theta/\omega}$$

Equation 2.5

where

k= reduced frequency
V= average velocity of the air relative to the rotor
c= rotor chord length
θ= disturbance circumferential extent
ω=relative disturbance frequency

With this definition, the reduced frequency is the ratio of fluid residence time in the blade passage (assuming constant axial velocity) to the amount of time a blade passage spends in a distorted sector. Distortion amplitude ratio, defined as rotor outlet distortion amplitude ratioed to that at the inlet is plotted as a function of reduced frequency in figure 2.13. This analytically computed data is shown for several values of time constant, τ.

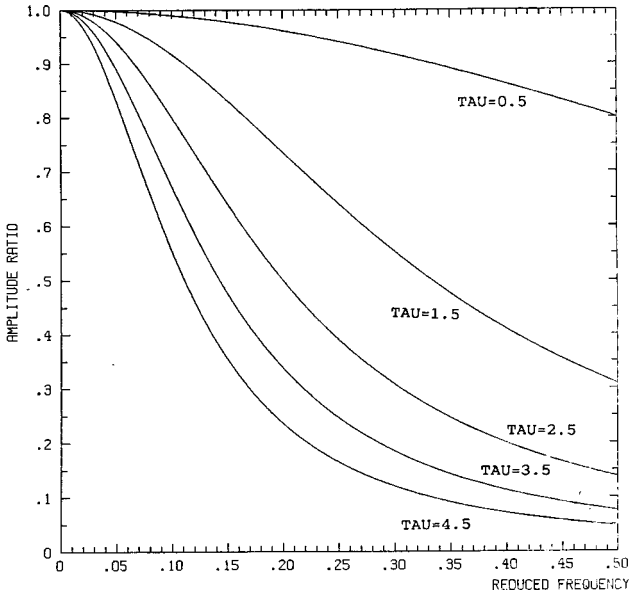

Figure 2.13: Theoretical Distortion Attenuation as a Function of Reduced Frequency and Blade Response Time Constant, (Andrew, 1988)

Distortion attenuation increases as reduced frequency increases. This is expected, since a lower fluid transport time through the rotor would allow the blade to fully respond to the distortion, causing stronger attenuation due to increased aerodynamic loading. Lower values of reduced frequency show little or no attenuation.

Another family of compressor modeling techniques uses a discontinuity (actuator disk) to introduce the effect of blade rows to the model. Greitzer (1973) developed an analytical technique using this approach to model inviscid, incompressible flow through an isolated rotor. He used an actuator disk to introduce circumferential velocity and pressure rise in the flow field.

Henderson and Shen (1981) included unsteady rotor response in their actuator disk analysis and compared their results to experimental data for an isolated rotor operating with incompressible, distorted flow. They examined only sinusoidal disturbances and noted that actual distortions would contain many other harmonics. Maximum distortion attenuation was found to occur when the ratio of blade spacing to distortion wavelength was one-half. Barr (1978) observed the same phenomenon and attributed it to the unsteady response of adjacent blades being 180 degrees out of phase with each other. This serves to minimize distortion transport through the rotor.

Colpin (1978) derived a transfer function to model total enthalpy change across the actuator disk. The transfer function was derived from governing fluid dynamic equations, with the assumptions of inviscid, two-dimensional flow with large length scale (much greater than blade pitch) disturbances. As with other studies that modeled only low engine order excitation, this work is of limited use in HCF studies. Predictions of rotor exit total pressure profiles, figure 2.14, show fair agreement with measured data from a single stage subsonic compressor. Results are shown at three span locations, R=0.2, 0.15 and 0.1m. Note that the prediction has introduced spurious frequency components into the profile.

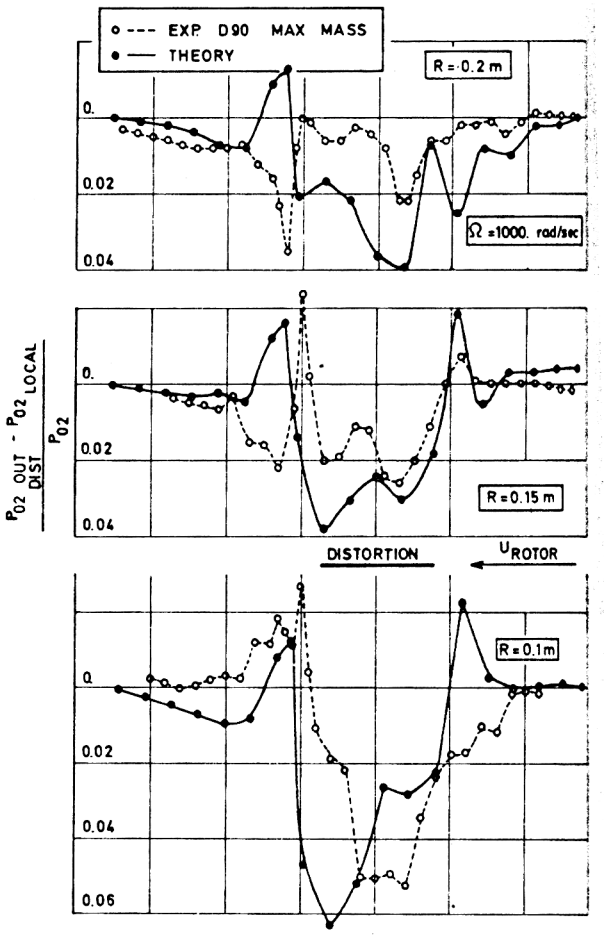

Figure 2.14: Dynamic Total Pressure Prediction Accuracy at Three Span Locations from an Actuator Disk Based Model, (Colpin and Kool, 1978)

Post-stall modeling does not have as extensive history as that of pre-stall modeling. Mokelke (1974) provides a review of early post-stall research. These efforts are characterized by linearized, small perturbation analyses, with used semi-actuator disks to add blade row work and rotation simultaneously. Nagano and Takata (1970) expanded this type of approach by using non-linear equations of motion and first order response functions to model unsteady phenomena.

Frequency response functions were used in lieu of first order functions to model blade dynamic response by Sexton and O'Brien (1980). Frequency response functions were developed using quasi-steady total pressure loss as the forcing function and the dynamic total pressure loss as the response function. Cousins and O'Brien (1985) developed a post-stall compressor model using this function. Dynamic loss response

through the model's actuator disk was calculated by driving the experimentally derived transfer function with quasi-steady variations in total pressure loss.

Hurad (1986) also used a transfer function to model (unstalled) compressor response to nonuniform inlet flow. A time domain, analytical representation of relative blade flow angles versus circumferential position was Fourier decomposed. Since the inlet distortion (a sine wave) was dominated by the first term of its decomposition, only the first term of the inlet flow angle decomposition was used. The rotor outlet distortion profile contained the majority of its frequency content in the first two terms. Consequently, two Fourier terms were used to model relative blade outlet flow angle. The resulting transfer function between the inlet and outlet flow angles was calculated using experimental data from a single stage compressor. The model did a fair job predicting rotor outlet angles over a range of unsteady inlet angles.

2.4 Review of Aeromechanical Studies

As HCF became a major operational concern for the U.S. Air Force in the 1980's, increased research activity was focused on this area. This section presents several studies performed to gain an understanding of the nature of blade row forcing functions and the resulting mechanical response. A numerical technique is also reviewed which was developed with the aim of fully characterizing non-uniform flow through the compressor.

Fleeter et al. (1978) measured the fluctuating pressure distribution on a stator vane row, caused by downstream convecting rotor wakes in a single stage low speed research compressor. Unsteady blade surface pressures were compared to those predicted by a flat plate analysis with generally good agreement. Note that this work was concerned with high engine order forcing functions (blade passing frequency and above).

Lower engine order forcing functions were examined by Manwaring and Fleeter (1989), (1990) in a low speed research compressor. The forcing function under investigation was the velocity defect caused by two upstream distortion sectors of 90-degree extent. Rotor blade unsteady surface pressure was measured as a response function. The harmonic content of both functions was analyzed. As expected, it was

found that a two per rev component dominated the forcing function. The chordwise distribution of surface pressure was also investigated. Results included the finding that the unsteady pressure difference between the pressure and suction sides decreased with increasing chord.

Various distortion profiles and the resulting vibratory response of a first stage fan integrally bladed disk (blisk) was investigated for an advanced transonic compressor by Datko and O'Hara (1987). Total pressure distortions at the inlet of the two-stage compressor, shown in figure 2.1, were induced by upstream distortion generating screens. The forcing functions investigated were of low engine order (eight per rev and below). Blisk response was measured by blade mounted strain gauges.

Rabe et al. (1995) investigated four resonance conditions of a transonic fan blisk excited by sinusoidal distortions in total pressure. A Campbell diagram showing the blade vibratory modes investigated is shown in figure 1.3a. Instead of using strain gauges, blade mechanical response was measured using surface mounted static pressure probes. This permitted investigation of the distribution of the response function along the blade chord. A static pressure wave was seen to travel through the blade passage, being amplified as it propagated aft.

Manwaring et al. (1996) reported results from the same experimental program as that of Rabe (1995). However, unlike the previously reported work, all three important aspects of airfoil forced response were included in the paper. Included were the forcing function (total pressure distortion annular profile), and two measures of response (unsteady blade surface pressures and strain gauge measurement of the resultant blade deflection). Experimental results were compared with those from mechanical and fluid numerical models. Good agreement was seen between theory and experiment of blade surface pressure measurements for off resonance conditions.

Numerical techniques have recently been advanced to allow the computation of flow-field properties through turbomachinery blade rows. Hah et al. (1996) presented the results of a numerical solution of the Reynolds- averaged Navier- Stokes equations for the flow through the same rotor investigated by Rabe et al. (1995) and Manwaring et al. (1996). Comparisons to experiment were used to validate the numerical procedure. Clean inlet cases were modeled using a steady solver, while an unsteady solver was used to

model distorted flow conditions. An assumed symmetry condition was imposed for the distorted case: two blade passages were used to model the rotor since an eight per rev distortion was investigated and the rotor contained 16 blades. The numerical model did a good job of predicting the flow field, including unsteady surface pressure difference between the pressure and suction surfaces of the rotor blades for distorted flows, although the peak-to peak value was under predicted. Additionally, it was found that aerodynamic losses were increased by interactions between the blade passage shock and boundary layer.

The same unsteady numerical code was extended to produce a full annular solution in Rabe et al. (1999). In this study, a three per rev distortion was modeled Results are qualitatively good, although the harmonic content of the blade surface unsteady pressure distributions was not predicted well. The authors speculate that a finer computational mesh would correct this problem.

2.5 Conclusions from Literature Review

Despite the large amount of work that has been done regarding compressor response to distorted inlet flow the effects of distortion, especially as it relates to HCF, continue to be an major operational concern. The types of distortion that cause severe aerodynamic and mechanical performance problems are often quite different (low vs. high engine order), making the large body of work done to improve aerodynamic performance of limited use in combating HCF.

Specific conclusions that can be drawn from the literature reviewed include the following.

- The effects of large length and small length scale disturbances on performance are well understood. Numerous analytical studies have been conducted to predict the impact of large length scale (very low engine order) distortion on performance.

- The effects of medium length scale (on the order of blade spacing) disturbances on both performance and HCF are not as well understood. Both large and medium length scale disturbances are HCF drivers.
- Blade aerodynamic response to distortion is highly time dependent. Response models have been developed using first and second order decay equations with empirical time constants and with cascade correlation data.
- Reduced frequency quantifies the relative time between blade passage transport time and disturbance sector residence time. It has many variations.
- Aeromechanical studies directed specifically at understanding HCF phenomena are concerned with characterizing both the blade row forcing and response functions. The forcing function has been measured either as a velocity or total pressure deficit. Blade response is typically measured as unsteady blade surface static pressure or as mechanical deflection.
- Fully 3-D, unsteady numerical models of full annulus turbomachinery blade rows require further development.
- Inlet probe configuration, as recommended in SAE AIR1419, is inadequate for HCF forcing function investigation. Several authors suggest doubling the number of probes to allow investigation of higher forcing function harmonics.

3 Frequency Response Function Modeling

As a means of gaining further insight into non-uniform flow through axial compressors a new modeling technique has been developed which relies on frequency domain transformations of upstream and downstream total pressure profiles. The present work is based, in part, on experimental work done by Boller (1998) and Schwartz (1999) and an analytical study by Howard (1999). These authors performed fundamental investigations of using frequency domain methods to predict the flow behavior of axial compressors, which serves as impetus for the present study.

Boller and Schwartz carried out studies on an isolated, subsonic rotor operating with screen-induced total pressure distortion. Several flow properties were modeled, including total and static pressures, velocity and angle of attack. They found that not only were the models most accurate when total pressure was used, but that total pressure was the most highly correlated flow parameter between rotor upstream and downstream measurement locations. A frequency domain modeling method was developed with the aim of predicting the annular distribution of flow properties at the rotor exit. Although they found the model to be dependent on compressor operating point, distortion intensity and span, no systematic methods were developed to adjust the model accordingly. Data resolution was not high enough to produce a rigorous account of flow behavior.

Howard analytically investigated the capability of frequency- domain models to capture blade row and compressor unsteady response. He found that the modeling technique used by Boller and Schwartz did a better job predicting certain time dependent phenomena than a first- order lag model, used in some earlier work. Data from the Boller experiments were used to create frequency domain models and it was found that rudimentary predictions had reasonable agreement with measurements.

The frequency domain models developed by these three authors and those used in the present study are based on frequency response functions. This section presents the basics of frequency response function development and their basis, Fourier Transforms, and the application of frequency domain methods to compressor modeling. It concludes by outlining the approach and goal of the current work.

3.1 Fourier Transforms and the Frequency Response Function

Fourier Transform methods are widely used in all branches of engineering and the sciences. These methods are based on the Fourier series, which permit any function to be written as an infinite sum of sine and cosine waves. Four different forms of the method are available, the appropriate choice dictated by the type of data to be transformed. Data used in this study consist of periodic discrete measurements, making the Discrete Fourier Transform (DFT), shown at the bottom of figure 3.1 the appropriate form to use.

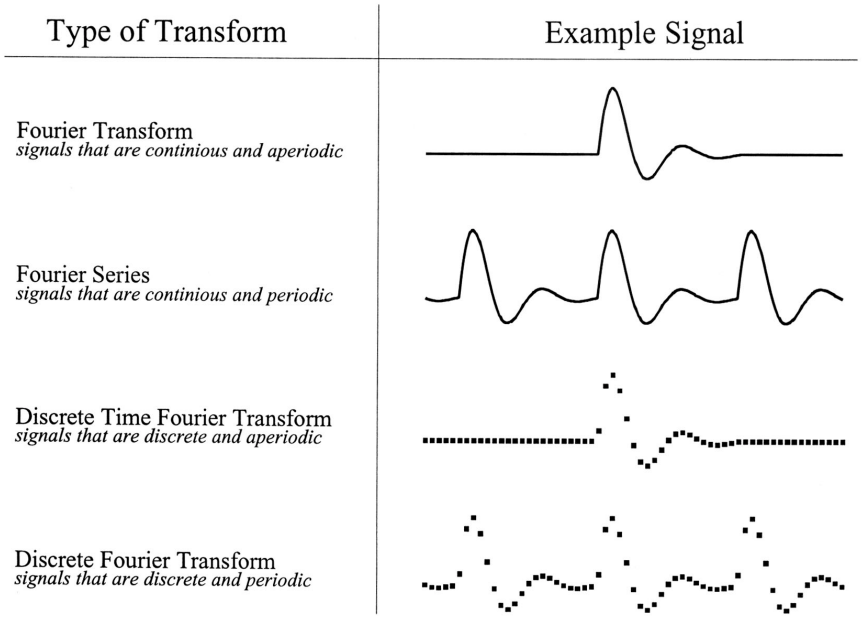

Figure 3.1: Illustration of the Four Fourier Transforms (Smith, 1999)

Fourier transforms are based on the Fourier series representation of functions, shown in equation 3.1a. For discrete functions, such as f(t) with period T, containing L sample points, the Fourier series of order N is defined as

$$S(t) = \frac{a_o}{2} + \sum_{j=1}^{N} a_j \cos(j\omega t) + \sum_{j=1}^{N} b_j \sin(j\omega t)$$

Equation 3.1a

where

$\omega = 2\Pi/T$

$$a_j = \frac{1}{L} \sum_{k=0}^{M} f(t_k) \cos(j\omega k) \qquad \text{for j} = 0,1,2...N$$

Equation 3.1b

$$b_j = \frac{1}{L} \sum_{k=0}^{M} f(t_k) \sin(j\omega k) \qquad \text{for j} = 1,2,...N$$

Equation 3.1c

Any arbitrary function can be exactly represented by a Fourier series of order N= infinity. Note that a_o is the average value, or DC component, of the function. The normalization factor 1/L is arbitrary and is not standardized. Any given commercial DFT subroutine might use (1/L), a different factor, or no factor at all.

The Fourier series and associated transforms can be used to convert a time domain function to its equivalent form in the frequency domain. The DFT does this for discrete data and is calculated by correlating a given input function with sine and cosine basis functions, shown in equations 3.1b and 3.1c. Using phasor notation, figure 3.2, frequency domain amplitude and phase can be extracted from a_j and b_j. For notational convenience these terms are often interpreted as the real and imaginary components, respectively, of the transformed function. (This is not to be confused with the complex DFT, which is not considered here). The magnitude and phase of the j^{th} component frequency of the original discrete time domain function are computed using equations 3.2 and 3.3.

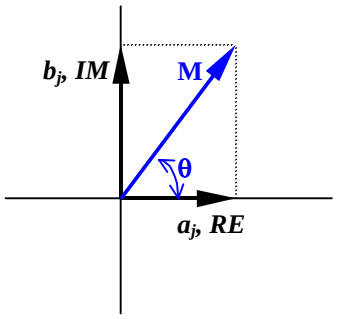

Figure 3.2: Phasor Notation

$$\text{Magnitude} \qquad M_j = [(a_j{}^2) + (b_j{}^2)]^{\frac{1}{2}}$$

Equation 3.2

$$\text{Phase} \qquad \theta_{\,j} = \arctan\frac{b_j}{a_j}$$

Equation 3.3

Resulting frequency- domain resolution is a function of the time domain sampling rate. The frequency domain will be discritized into N compartments, each Δf wide and this is the spacing between successive spectral components.

$$\Delta f = \frac{1}{\mathrm{T}}$$

Equation 3.4

Nyquist sampling theory limits the highest useful frequency component to one-half of the sampling frequency. In equation form this is described by

$$f_{\text{max analysis}} = \frac{f_{\text{sample}}}{2} = \frac{\Delta f * \mathrm{N}}{2}$$

Equation 3.5

Flow measurements in this study were made circumferentially around the compressor annulus (see section 3), creating naturally periodic data with a period of T= 1 rotor revolution. Therefore, the resulting DFT resolves frequency components in 1/rev increments. Measured data is reduced to N= 360 equally- spaced measurement locations, producing a maximum useable analysis frequency of 180cycles/rev.

Aliasing, the appearance of spurious frequency component magnitudes due to undersampling a given function, is not a concern in this study. No anti- aliasing filtering is required since magnitudes of both the upstream and downstream total pressure profiles were found to quickly decay after the twentieth component frequency, and effective sampling occurs to the 180^{th} frequency. Additionally, the data's natural periodicity eliminates the need for time domain windowing functions. Used to pre-process aperiodic data for use in periodic transforms, windowing functions require the use of amplitude and bandwidth correction factors and can distort frequency content, further complicating data reduction.

An inverse transform procedure exists, the Inverse Discrete Fourier Transform (IDFT), which permits movement from the frequency to the time domain. The inverse and forward transforms form a *transform pair*. The inverse transform can be used to reconstruct a time domain signal from its frequency domain representation. It is given in complex exponential form for discrete data by equation 3.6

$$x_n(t) = \frac{1}{L}\sum_{k=0}^{N-1} X_k e^{i\omega kj} \qquad \text{for j} = 0,1,2...,\text{N -1}$$

Equation 3.6

Frequency domain methods and Fourier Transformations are frequently used to measure, specify and predict the actions of physical systems. The characteristics of mechanical or electrical systems are often described by a frequency response function (FRF), defined as the frequency domain ratio of a response function (RF) to a forcing function (FF).

$$FRF = \frac{\text{Response Function}}{\text{Forcing Function}} = \frac{RF_j(M,\theta)}{FF_j(M,\theta)} \quad \text{for } j = 0,1,2...M$$

Equation 3.7

The system's effect on each component frequency of a given excitation is captured by this function. For example, the FRF of an electronic filter would characterize the filter's response in terms of its DC offset (magnitude at zero frequency), amplification or attenuation, and phase shift for each of the component frequencies of an input signal. The FRF's magnitude and phase values at each frequency are calculated independently

$$M_{FRF} = \frac{M_{RF}}{M_{FF}}$$

Equation 3.8

$$\theta_{FRF} = \theta_{RF} - \theta_{FF}$$

Equation 3.9

Like the Fourier Transforms of its response and forcing functions, the FRF's computed in this study describe the first 180 component frequencies of the "true" FRF. As shown in chapter 5, this is adequate resolution for the low engine order excitation examined.

Equations 3.1a, 3.1b, 3.2, 3.3, and 3.6 through 3.9 were coded into a Fortran 90 program to analyze the data used in this study.

3.2 Compressor Flow Modeling using Frequency Response Functions

An analogy can be drawn between the action of an electronic filter and that of a compressor operating with distorted inlet conditions. A compressor is viewed as a "fluid filter" in the following manner: time dependent flow fields upstream and downstream can

be considered blade row forcing and response functions, respectively, and the pressure ratio interpreted as the DC offset. Fourier decomposition of inlet and exit flow-field properties permits the amplification, attenuation and phase shift of each component frequency of the flow to be examined. Likewise, the compressor's FRF can be calculated, which fully captures the compressor's response at a given operating condition. The analogous actions of an electronic filter and fluid compressor are illustrated in figure 3.3.

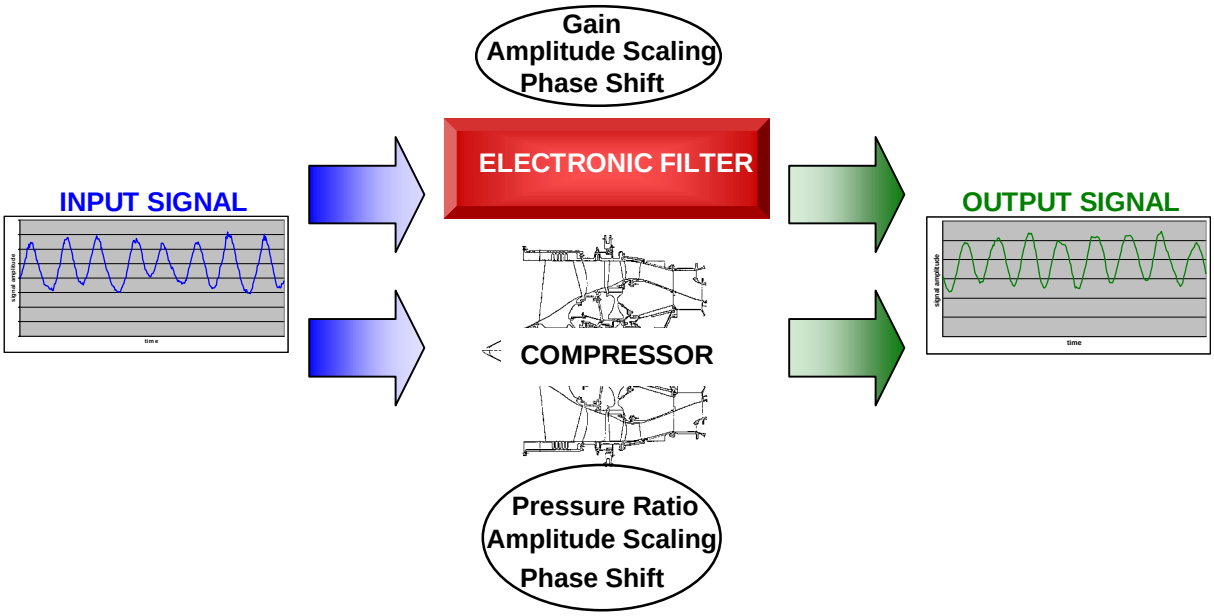

Figure 3.3:Analogous Behavior of Electronic Filter and Fluid Compressor

Since total pressure distortion is an HCF driver, and Schwarz and Howard found that rotor inlet and outlet total pressure to be highly correlated, the time dependent flow-fields (input and output signals) considered in this study are the annular total pressure distributions upstream and downstream of the compressor rotor. Although only steady distortions are considered, they appear as periodic time signals in the rotor coordinate frame. This natural periodicity makes them easily transformable using Fourier methods, which require the use of periodic functions.

While capturing system behavior in a relatively compact, easily acquired form appears auspicious, Fourier Transformations and FRF's have an important limitation.

They are exact representations only of linear systems. A system is defined as linear if it has two properties: homogeneity and additivity. Systems that exhibit homogeneity generate amplitude changes in their output that are of constant proportionality to amplitude changes in their input. Additive systems pass multiple signals simultaneously without having them interact- the combined output of a linear system is equal to the sum of outputs due to individual excitations. Consider as a system a simple resistor and its input (voltage) and output (current). Ohm's law provides that changes in input voltage will produce a corresponding change in current, always in the same proportion. Likewise, two or more separate voltages applied across the resistor will result in a current identical to the sum of currents produced if the input voltages were applied individually. Therefore, a simple resistor with input voltage and output current displays both homogeneity and additivity and is a linear system.

Although many electronic filters are linear, fluid compressors are not. While this does restrict the applicability of FRF methods to compressor modeling, it does not prohibit it.

Systems, and portions of system operation, that are not perfectly linear, may behave in a *nearly* linear fashion. This behavior is termed weakly non-linear. Depending on the degree of non-linearity, good results can be obtained using FRF methods for this type of system. For the input and output signals considered in this study, portions of the compressor operating region exhibit weakly non-linear behavior. For those regions that do not, a technique has been developed to "correct" the linear FRF and make it generally applicable.

In summary, Fourier Transform methods combined with FRF techniques describe how a system acts on each calculated component frequency of a given input signal. *The frequency response function fully captures system behavior at the operating condition investigated.* While their strict formulation restricts the use of FRF's only to linear systems, this study investigates their application to areas of weakly non-linear fluid compressor behavior and develops a method that allows their use in the prediction of strongly non-linear fluid behavior. This forms the basis of FRF compressor flow modeling.

3.3 Approach and Goals of Current Study

The current study seeks to develop a technique to predict the transport of nonuniform flow through a transonic compressor of modern design using frequency response function based models. The current work extends and improves earlier studies done by Boller, Schwartz and Howard by examining the general applicability of the technique to high fidelity data from a compressor of modern design. A process is developed to overcome the restriction of linearity, allowing the FRF method to model inherently non-linear compressor flow behavior for various dissimilar operating conditions and distortions. Specifically, this study endeavors to do the following.

- Investigate the frequency content of total pressure annular profiles both upstream and downstream of first and second stage rotors in a transonic compressor of modern design operating with screen- induced circumferential distortion.
- Calculate the frequency response functions of the investigated turbomachinery rotors at multiple operating points on their compressor's mass flow\ pressure rise characteristic with several different distortion screens.
- Examine dependence of the computed FRF's on blade row aerodynamic loading, rotor rotational speed, span position and distortion type.
- Analyze the ability of these computed FRF's to predict annular total pressure profiles for operating points and distortion types similar to and dissimilar from those at which they were computed.
- Develop an empirical method that allows general applicability of the FRF-based model to any compressor operating point and distortion type.

The remainder of this monograph reports on the experimental procedure used to gather data for this study, the computed FRF's, results of using them to predict flow behavior, the development of the FRF tuning method and consequent results.

4 Experimental Procedure and Data Acquisition

4.1 Experimental Facility

Data to develop and verify a frequency response function modeling technique was acquired from tests performed at the Compressor Research Facility (CRF) at Wright-Patterson Air Force Base, OH. A two- stage transonic, low aspect ratio compressor of modern design was operated at several points on its characteristic map.

The CRF consists of three main buildings: the test building housing office space and data acquisition and control computers; the electrical building housing transformers and power supplies for the test article drive motors; and the operations building which houses the test section, flow conditioners, electrical drive motors and associated equipment.

The test section, shown in figure 4.1, is an open- loop design where atmospheric air is drawn into the facility by the action of the test compressor. The test chamber is 20 feet in diameter and 65 feet long. Air enters through filters and throttle valves, which set the pressure upstream of the compressor. Flow conditioning elements straighten the flow before it is introduced to the compressor bellmouth.

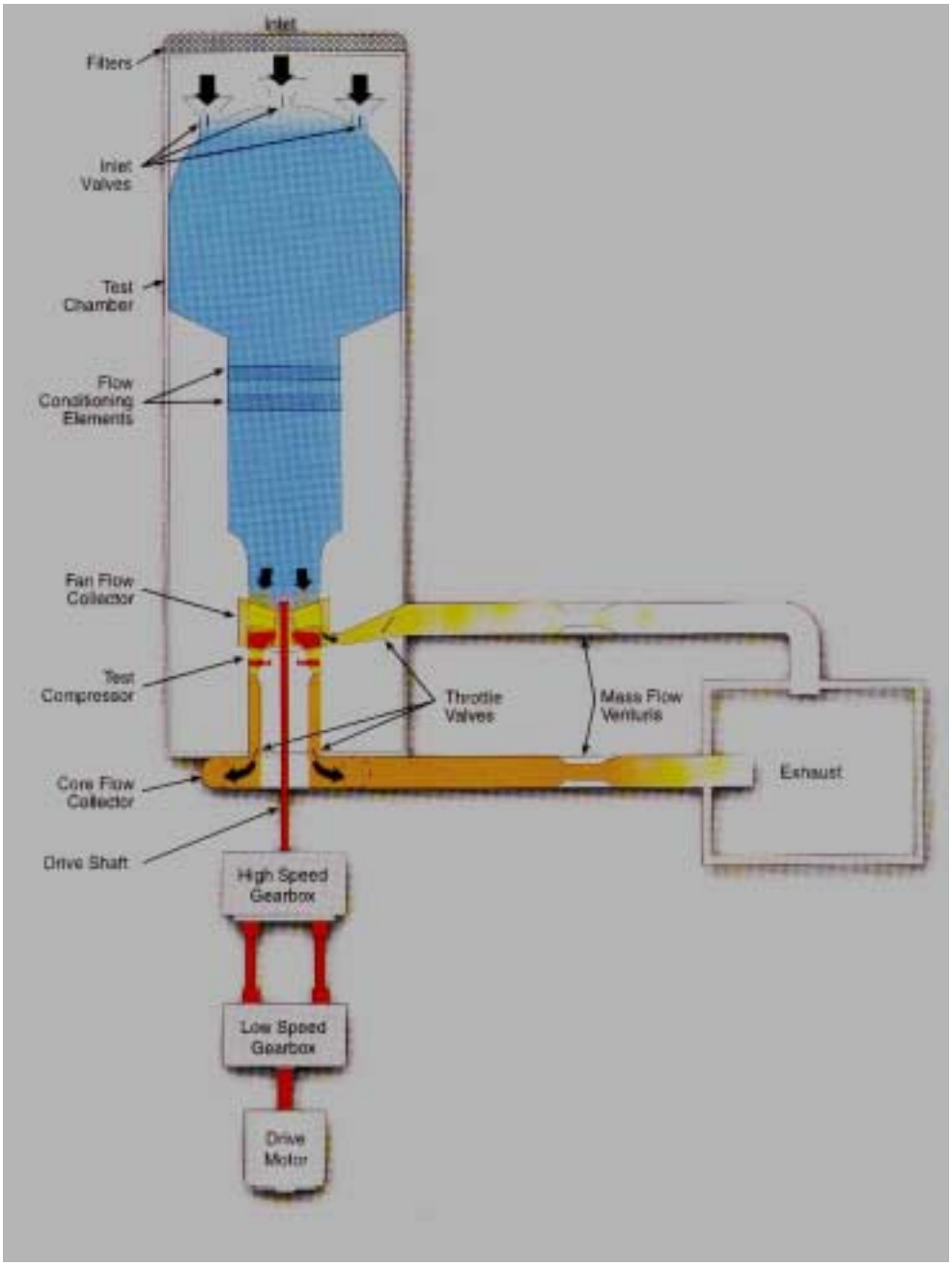

Figure 4.1: CRF Test Facility

4.2 Test Article Configuration

The test article component configuration as used for these experiments is shown in figure 4.2. A distortion generating device is installed downstream of the bellmouth and approximately 1.5 diameters upstream of the leading edge of rotor 1. Total pressure

is measured at the inlet measurement location by means of radial immersion probes located approximately ½ diameter upstream of rotor 1.

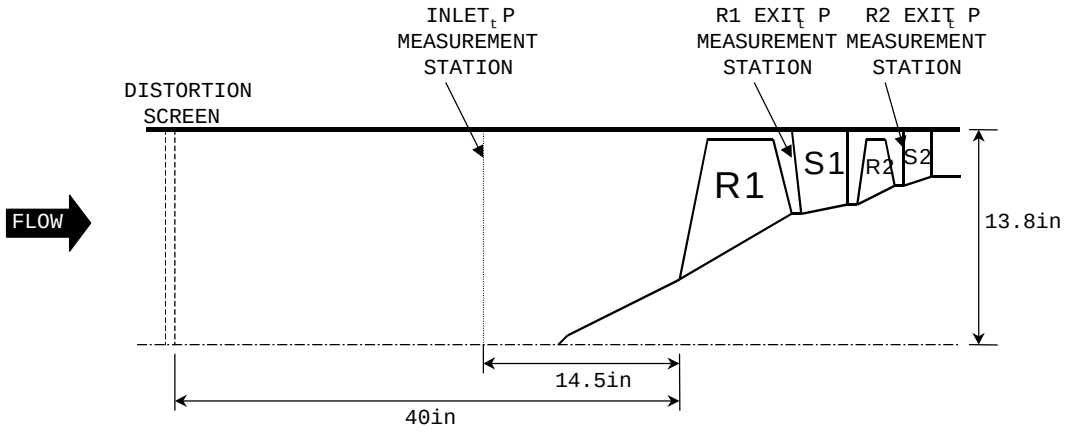

Figure 4.2: Test Article Configuration

No inlet guide vanes (IGV's) are used in this study. Total pressure and temperature at the exits of rotor 1 and 2 are measured at the leading edges of the corresponding downstream stator vanes. After exiting the test article, the flow passes through discharge valves, which set the downstream pressure, and are used to control the compressor pressure ratio. Discharge flow exits through venturis before being exhausted through a vertical flue. The facility is capable of mass flows from 0-500 lbm/s.

Test articles are driven by either of two 30,000 horsepower synchronous electric motors through high and low- speed gearboxes. Selecting the appropriate motor- gearbox combination sets desired test speed range. Speed control is through the CRF Variable Speed Drive control system, which sets test speed, controls speed transients and provides automatically engaged safety coast- down modes.

The first stage rotor blisk used for the majority of this study is shown mounted in the test compressor in figure 4.4. The blisk consists of 16 low aspect ratio blades of modern design. Geometric characteristics of this rotor are shown in Table 4.1. At the design operating point, relative rotor velocities exceed Mach 1 above 45% span for inlet temperatures near 300K.

Figure 4.3: First Stage Blisk Mounted in Test Rig

Parameter	Value
Average Aspect Ratio	1.22
Rotor Tip Radius, in	13.87
Inlet Radius Ratio	0.33
Average Radius Ratio	0.47
Average Tip Solidity	1.50
Max. Thickness/Chord	0.028

Table 4.1: Rotor 1 Geometry (Rabe et al.,1999)

The first stage stator vane assembly, forward looking aft, is shown in figure 4.4. It consists of 41 sets of fixed and variable geometry vanes. The variable geometry vanes provide a means of controlling the aerodynamic loading of the first and second stage

rotors. A detailed view of the stator configuration (aft looking forward) is shown in figure 4.5. Forward vanes are fixed, while the aft vanes are variable. Variable vanes are connected to a gang ring on the exterior of the test compressor, which is actuated by a hydraulic system. Vane scheduling can be controlled by the CRF test control computer system or by the test operator. One of the three instrumented vanes is noted in the figure.

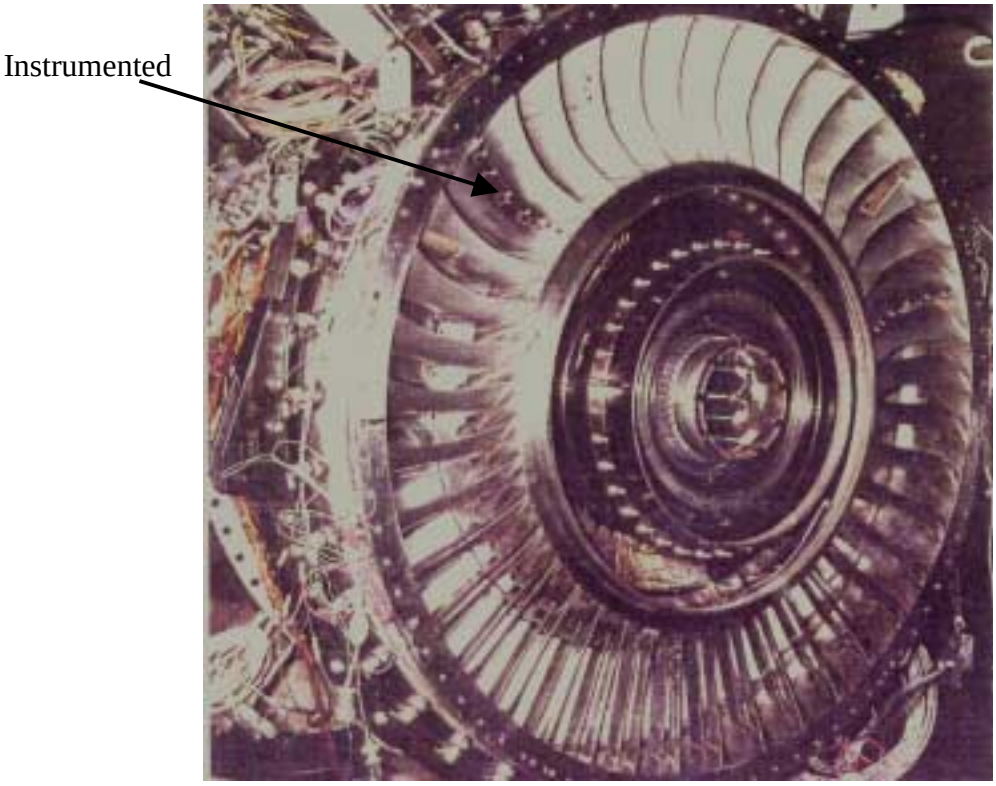

Figure 4.4: First Stage Stator Assembly

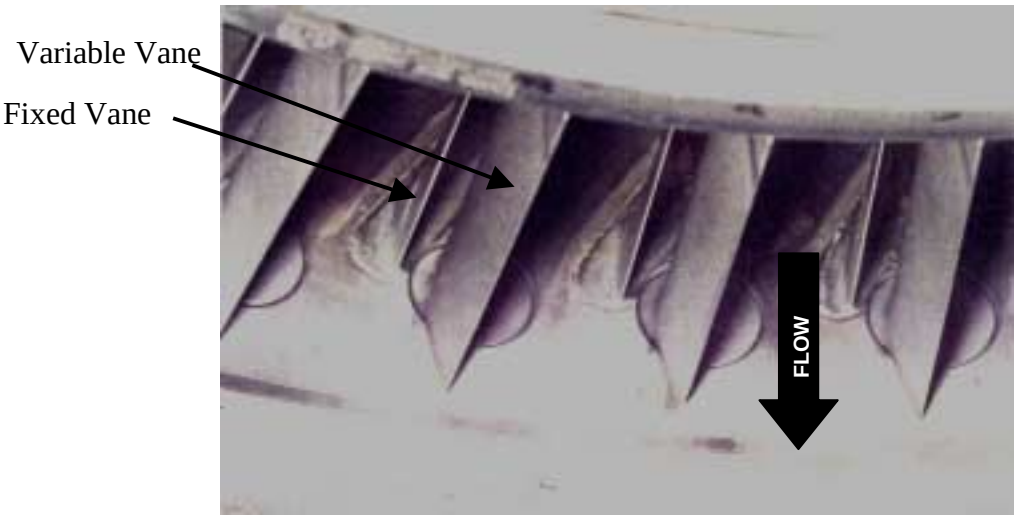

Figure 4.5: First Stage Stator Variable Geometry

The second stage rotor, shown in figure 4.6, consists of 40 blades mounted on a disk using a conventional dovetail arrangement. The second stage rotor is driven by the same shaft as the first stage rotor.

Figure 4.6: Second Stage Rotor

The second stage stator vane assembly, shown in figure 4.7 forward looking aft, contains 60 fixed geometry vanes. One of the three instrumented stator vanes is noted in the figure.

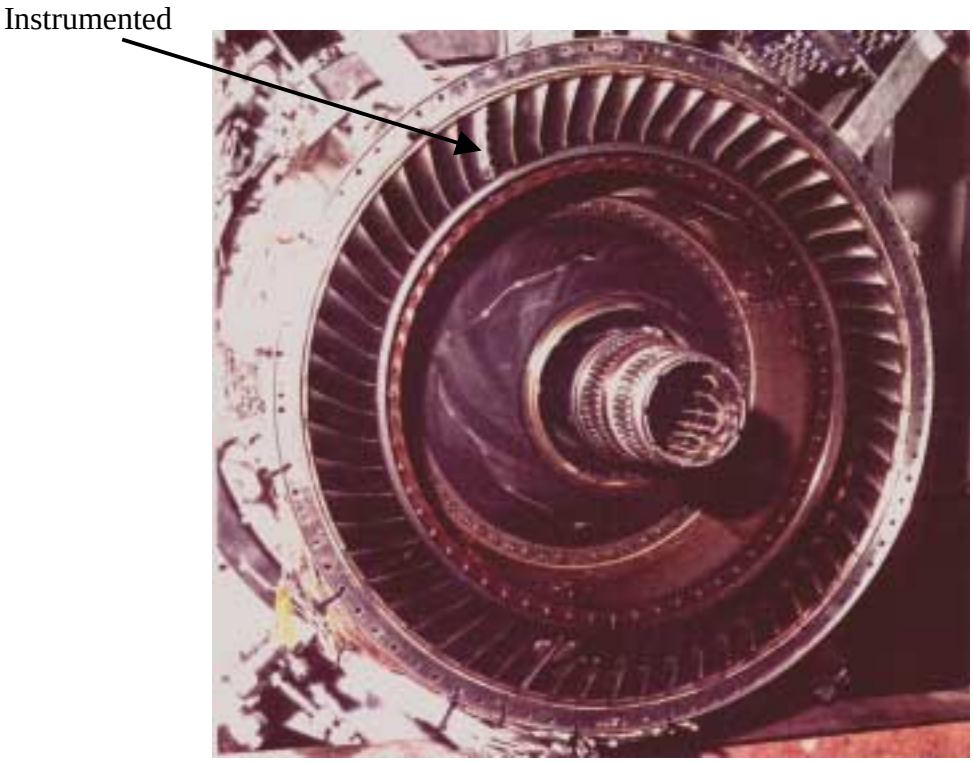

Figure 4.7: Second Stage Stator Assembly

Rotor inlet nonuniformity is created with a distortion generating device located upstream of the compressor inlet. Specifically, this is a wire mesh screen of varying porosity mounted to a screen rotator. Pictured in figure 4.8, the screen rotator consists of a backup screen supported by radial struts. A drive motor, located outboard of the flow path rotates the screen about the compressor centerline. The wire mesh screen creates downstream regions of reduced axial velocity and thus reduced total pressure. A typical 3/rev distortion screen is shown in figure 4.9. Note that the screen porosity has been varied about the circumference to create a sine- type distortion.

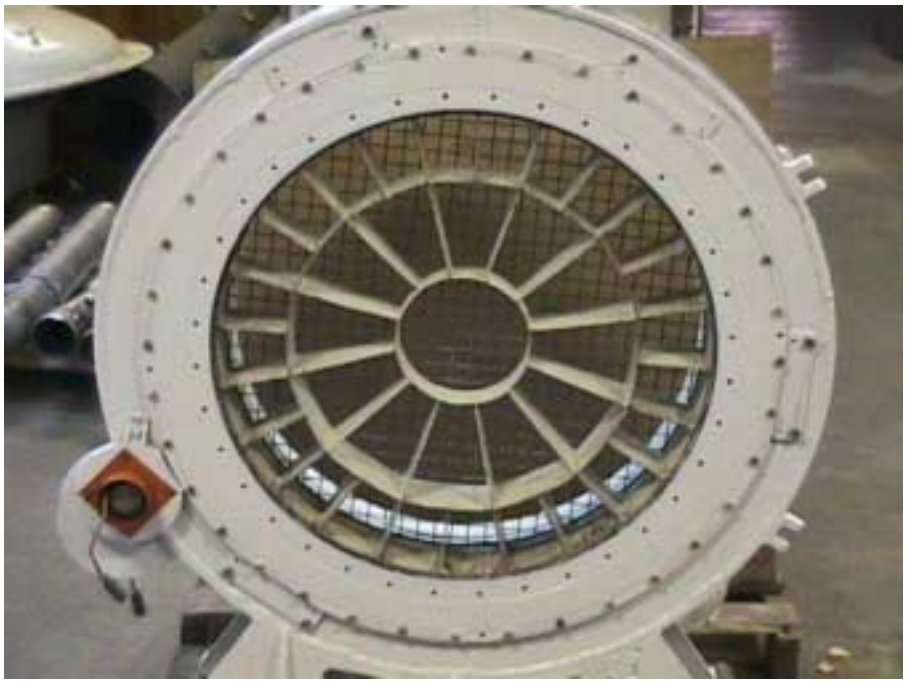

Figure 4.8: Screen Rotator

Figure 4.9: 3/rev Distortion Screen

4.3 Instrumentation

Large amounts of data are available from CRF test runs. The facility has the capability to simultaneously acquire over 1300 channels of data. Only instrumentation used in this study is described here.

An array of 49 thermocouples, figure 4.10, in the flow conditioning barrel provide radial and circumferential measurement of the inlet flow temperature profile. The bellmouth upstream of the compressor is instrumented with 4 static pressure taps at equal circumferential spacing along the wall and 4 pitot- static rakes containing six immersions each. The configuration is shown in figure 4.11. The probes are located a distance (z) of 77.67 inches upstream of the hub leading edge of rotor 1.

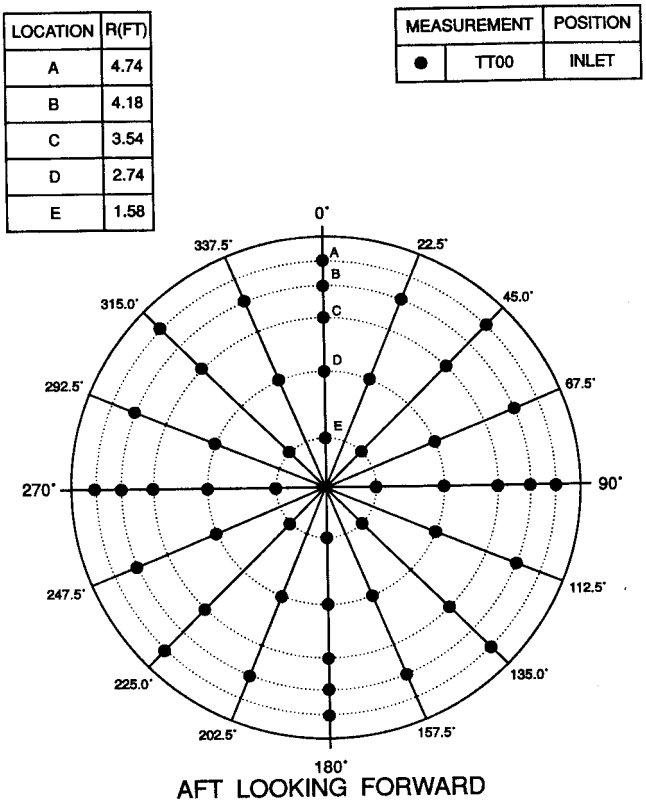

Figure 4.10: Flow Conditioning Barrel Thermocouple Array

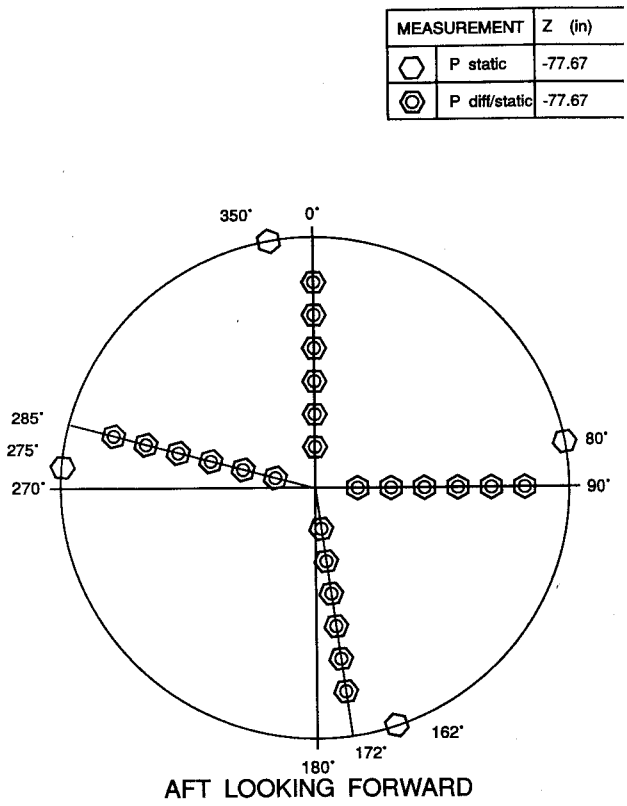

Figure 4.11: Bellmouth Pressure Probe Array

Test section mass flow is calculated using the bellmouth pressure and flow conditioning barrel temperature measurements. Since no work is done on the flow between the bellmouth and the upstream total temperature measurement location, with the assumption of incompressible flow, the total temperature at the bellmouth pressure measurement location is the same as that measured upstream.

Compressor inlet flow-field measurements occur 14.47 inches upstream of the hub leading edge of rotor 1. This corresponds to approximately 25 inches downstream of the distortion generating device. The probe configuration is shown in figure 4.12. Eight total pressure radial rakes with five radial immersions each are equally spaced about the circumference. The five radial immersions correspond to centers of equal mass flow annuli. Eight static pressure probes are equally spaced about the duct wall. Probe positions are given in table 4.2.

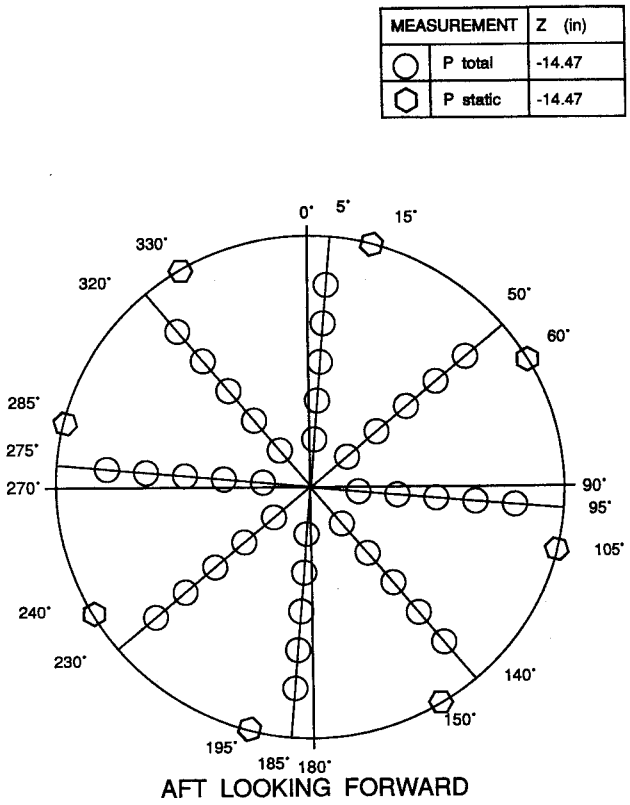

Figure 4.12: Distortion Measurement Station Probe Array

Immersion	Radial, in (from OD)
1	0.74
2	2.31
3	4.11
4	6.33
5	9.57

Table 4.2: Distortion Measurement Station Probe Position

Rotor 1 and rotor 2 total pressure exit measurements are made at the leading edges of their respective stator vane stages. The three measurement locations of the first and second stage stators are noted in figures 4.4 and 4.7, respectively. Probe positions for

stator 1 leading edge instrumentation is shown in figure 4.13. Three equally- spaced stator vanes are instrumented with probes at seven radial immersions. The radial and axial positions of these probes are given in table 4.3.

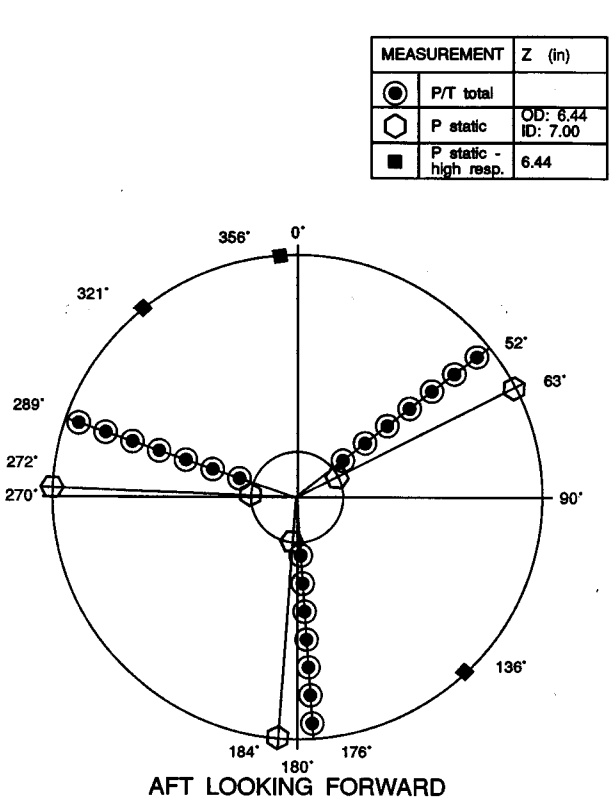

Figure 4.13: First Stage Stator Leading Edge Probe Array

Immersion	Radial, in (from OD)	Axial, in (from R1 LE)
1	0.315	6.60
2	0.662	6.80
3	1.577	7.05
4	2.577	7.27
5	3.573	7.29
6	4.241	7.16
7	4.595	7.10

Table 4.3: First Stage Stator Leading Edge Probe Position

An instrumented stator vane representative of both the first and second stages is shown in figure 4.14. Note the seven radial measurement locations of total pressure and temperature and the probe leads exiting the vane at the case outer diameter interface.

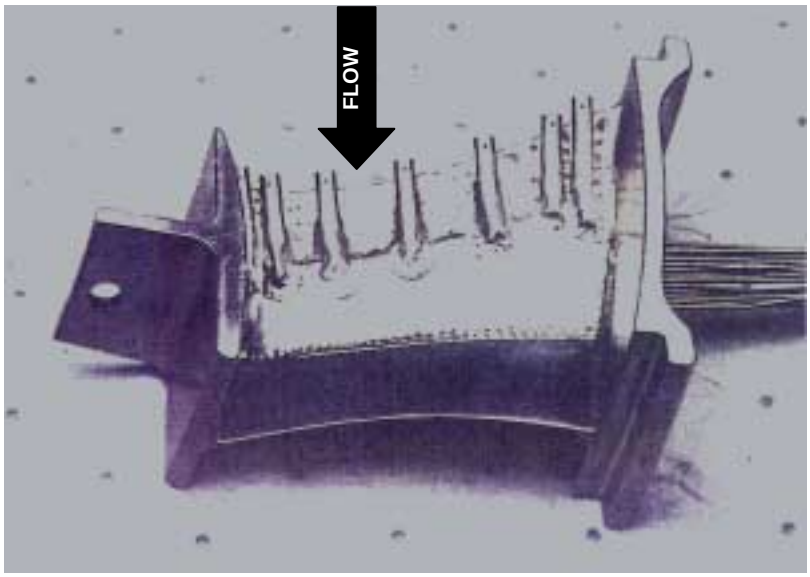

Figure 4.14: Instrumented Stator Vane

The second stage stator leading edge instrumentation is configured similarly to that of the first stage. Figure 4.15 shows the three circumferential positions of leading edge probes, each having seven radial immersions. Table 4.4 gives the location of each probe.

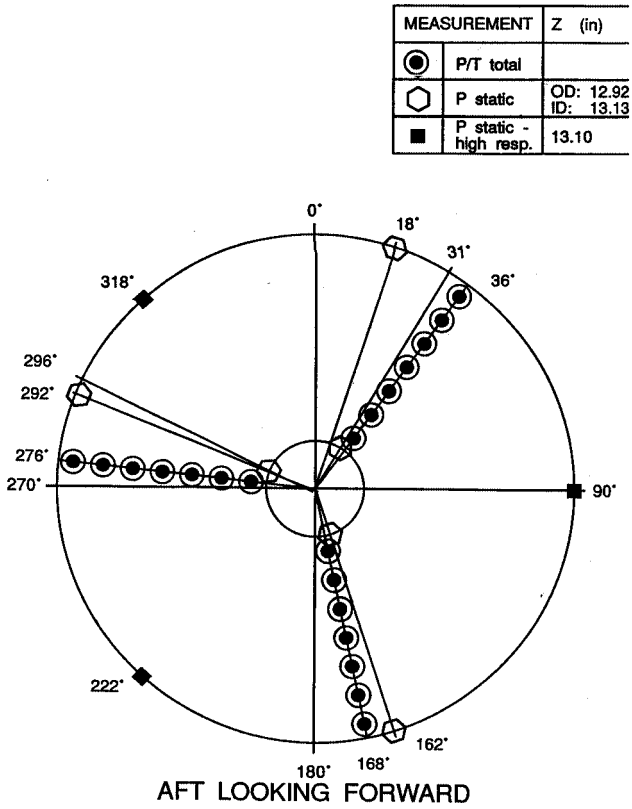

Figure 4.15: Second Stage Stator Leading Edge Probe Array

Immersion	Radial, in (from OD)	Axial, in (from R1 LE)
1	0.271	13.07
2	0.479	13.12
3	0.903	13.22
4	1.479	13.30
5	2.011	13.30
6	2.430	13.26
7	2.650	13.22

Table 4.4: Second Stage Stator Leading Edge Probe Position

Data sets for this study were calculated by averaging measurements from all available circumferential rake probes (typically eight upstream of rotor 1 and three each at stator 1 and 2 leading edges) to create an "equivalent" span rake probe at a single circumferential position. This served to eliminate some high frequency (on the order of 100/rev) noise from the data. Additionally, averaging several probes filled in a ten degree "hole" in each data set, caused by limitations of the distortion generating device.

Screen rotation provides a means of acquiring very high spatial circumferential data resolution while using a relatively small number of probes. If a static screen were used, an individual probe would be required for each spatial position at which a measurement is desired. Data acquisition with abundant spatial resolution circumferentially and radially would require an unreasonable number of probes, making data acquisition difficult and introducing unacceptable flow blockage. By rotating the screen, a single probe location can acquire as much data (or more) than multiple probes used in conjunction with a static screen. While the screen is rotating, data from a single probe located at a fixed circumferential position is sampled in time to measure the spatial flow-field properties. High temporal sampling thereby provides high spatial resolution.

The assumption required to use this technique that the screen is rotated slowly enough that the distortion pattern is quasi- steady as it passes through the compressor. Williams (1999) has found that a rotation rate of approximately two degrees per second is sufficient for this compressor to consider the distortion pattern as being quasi- steady. Figure 4.16 shows that measurements taken with eight circumferentially- spaced probes with a static upstream distortion screen (red squares) agree to within measurement uncertainty to those taken with a single probe while distortion screen was rotating (blue line). In this case, the upstream distortion screen was configured to create two regions of distorted flow (decreased total pressure), shown on the vertical axis, about the flow annulus, shown on the horizontal axis. Note that by using a single probe the entire flow field at a given radial position can be mapped.

Data for this study was sampled several times per second to yield nearly 900 circumferential measurements or one approximately every 0.35-0.40 degrees at each probe location. This raw data was reduced to 360 equally- spaced measurements before being used in the frequency- domain transformations and FRF models. There are two

reasons for this. First, 360 data points provide adequately high frequency resolution to eliminate the need for anti- aliasing filters (see section 3.1). Second, the discrete Fourier methods used in this study require that data points be equally spaced- in this instance temporally- which corresponds to equal spatial resolution in this measurement scheme.

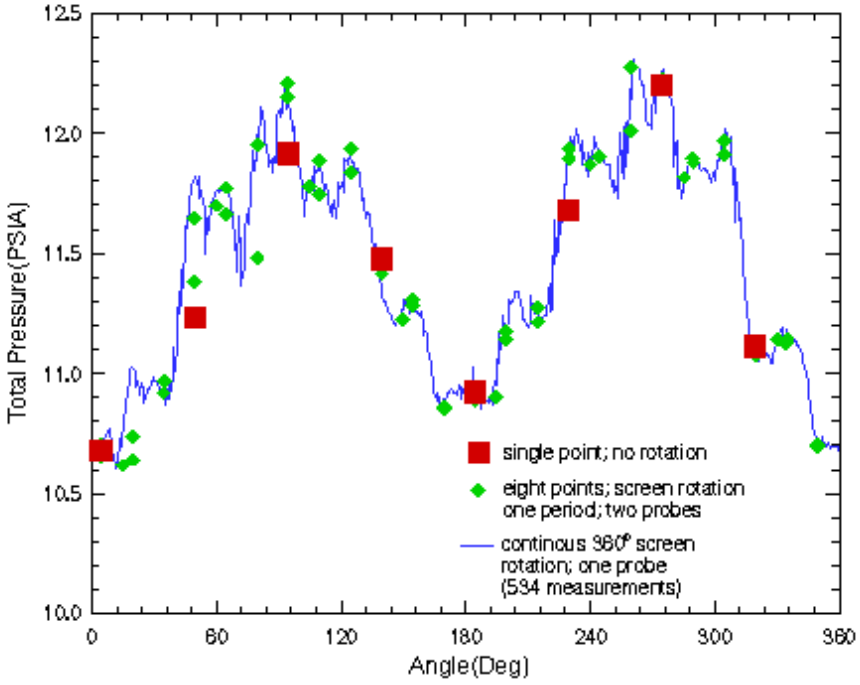

Figure 4.16: Comparison of Measurement Accuracy with and without Screen Rotation (Williams, 2000)

4.4 Streamline Curvature Method

Flow properties not available directly from test article measurement, namely streamline position, blade passage velocity and shock Mach number, were calculated using a streamline curvature (SLC) method. Wu (1951) was the first to formulate the method, which requires the assumption of steady, adiabatic, inviscid and axisymmetric flow with negligible body forces.

Streamline curvature methods rely on an iterative procedure to calculate streamline radial positions through successive turbomachinery stages. Governing equations are derived by combining the continuity equation and axial, radial and circumferential momentum equations in cylindrical coordinates with energy expressions, including the

thermodynamic equation of state and the Euler pump equation. Entropy and enthalpy changes through blade rows are determined from models and correlations. When streamline projections are mapped onto the r-z plane the result is a first-order, nonlinear differential equation (Novack, 1967).

Details of the specific SLC code used in this study can be found in Boyer (2001), who also made significant improvements to the code for transonic applications. The solution method used here proceeds as follows. Streamline positions at the upstream computational boundary are selected so they are centered on annuli of equal mass flow. Since the mass flow at this location is radially uniform and purely axial, equal mass flow annuli correspond to equal area annuli. Overall mass flow rate and total pressure and temperature are also specified. Appropriate analytical models and empirical correlations replicate the effect of the blade rows. Blade row exit meridional velocity is iterated upon until proper mass flow rate at that axial location is achieved. Radial adjustment of streamline position is then performed to create streamtubes having the originally specified mass flow rate. In this study and that of Boyer, calculation occurs at 19 axial stations, and streamline position is interpolated between stations to map continuous streamlines, as illustrated in figure 4.17. Note that the inner and outermost streamlines represent boundary layer growth through the stage.

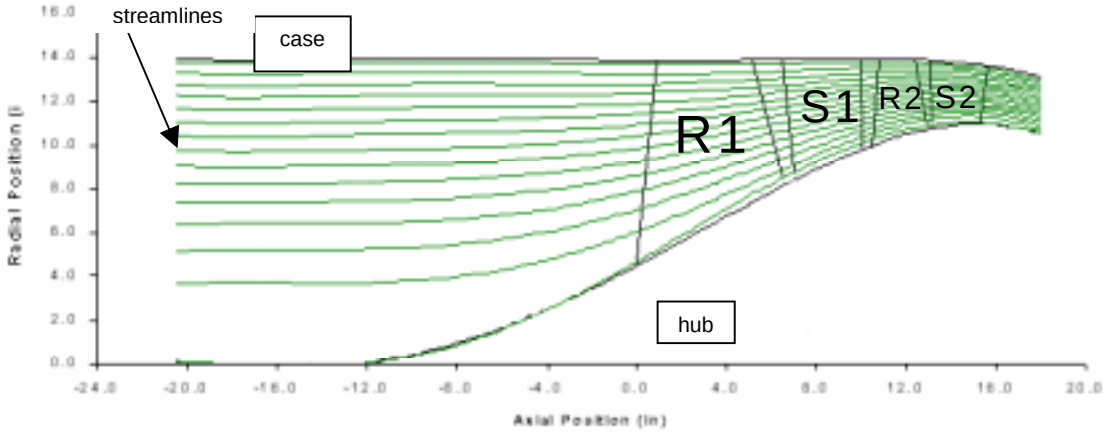

Figure 4.17: SLC Computed Streamline Position Through Compressor

Although CFD methods are now beginning to have the capability of performing axisymmetric and non-axisymmetric multistage analysis, the use of an SLC approach for this study is still justified. Considerable time and cost savings are achieved by using an SLC method in lieu of a CFD solver and Boyer has shown that acceptable prediction accuracy can be maintained. Results from the SLC method compare favorably to those from a three-dimensional, steady, Reynolds- averaged Navier- Stokes model of the first stage rotor used in this study.

For clean inlet conditions, spanwise distributions of CFD and SLC adiabatic efficiency predictions at 98.6% corrected speed are compared to measured data in figure 4.18. Distributions at first stage rotor (R1) exit are shown for peak efficiency and near stall throttle settings.

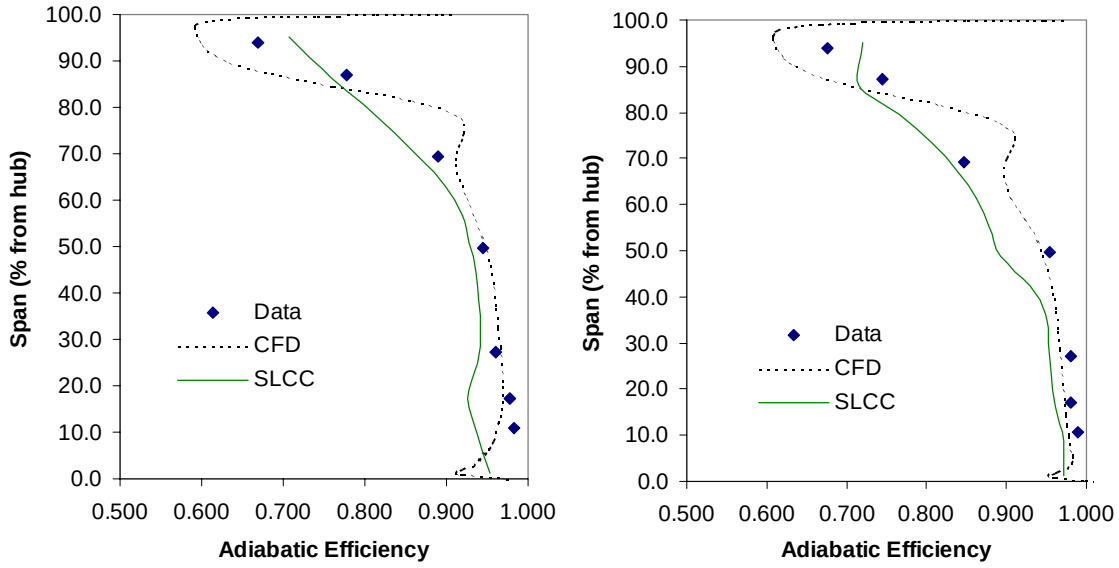

a. 98.6% Nc, peak efficiency

b. 98.6% Nc, near stall

Figure 4.18: Spanwise Comparisons of CFD and SLC Rotor 1 Clean Inlet Adiabatic Efficiency Prediction (Boyer, 2001)

As shown in figure 4.19, for clean inlet conditions, the SLC code successfully predicts total pressure ratio and adiabatic efficiency behavior along a single speed line of the CRF test compressor. Results are shown at 98.6% corrected speed. Solid diamonds indicate measured values and a solid line illustrates the SLC prediction. Aerodynamic

loading points (NS, NOL, etc.) are defined on page 61. Note that the overall trends and behavior are predicted very well. Boyer attributes the over- estimated performance as the fan loading increases to a lack of sophistication in the secondary loss model.

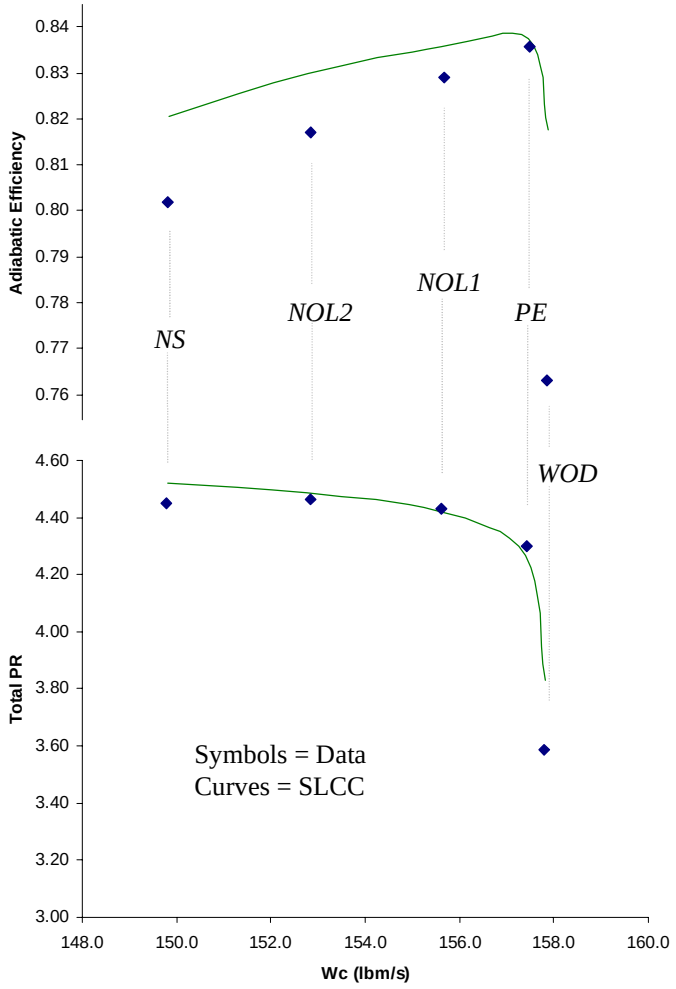

Figure 4.19: SLC Prediction Accuracy, Clean Inlet, 98.6% (13,104rpm) Corrected Speed (Boyer, 2001)

Corresponding prediction of interstage flow properties is achieved with good accuracy. Comparisons between predictions and measured data for the same 98.6% flow condition with a peak efficiency throttle setting are shown in figure 4.20. Spanwise comparisons of total temperature (TT) and total pressure (PT) values at the first (S1) and

second (S2) stage stator measurement locations are illustrated. The SLC prediction accuracy at this throttle setting is representative of all throttle settings investigated.

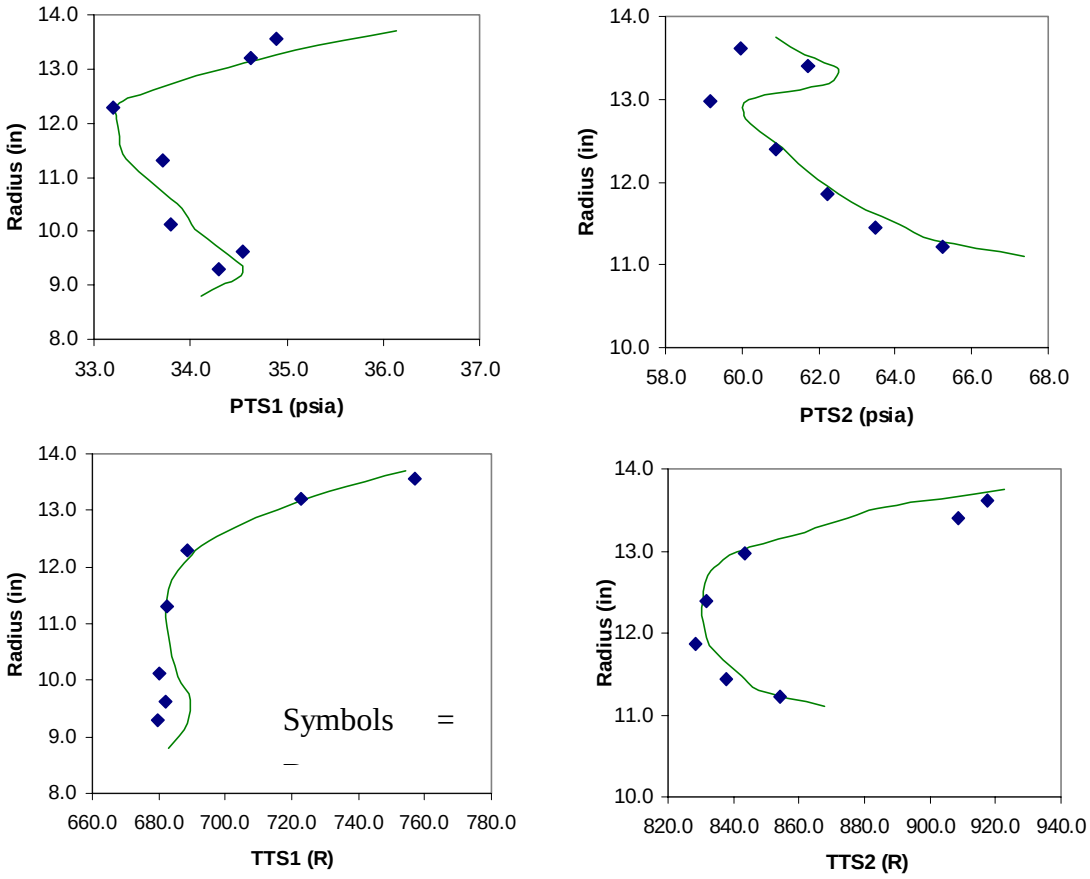

Figure 4.20: Interstage SLC Prediction Accuracy, Clean Inlet, 98.6% (13,104rpm) Corrected Speed (Boyer, 2001)

In order to apply the SLC method to this study, the axisymmetric flow restriction had to be overcome. To do this, flow values from a given distorted inlet flow circumferentially averaged at a constant span are assumed to be representative of an equivalent axisymmetric distribution. Using averaged values as boundary conditions, the SLC code adequately captures mass- averaged compressor performance; including total prssure and temperature ratios. As shown in figure 4.21, the accuracy of the SLC code prediction (lines) of pressure ratio is similar for cases of axisymmetric flow (closed symbols) and cases of distorted flow (open symbols).

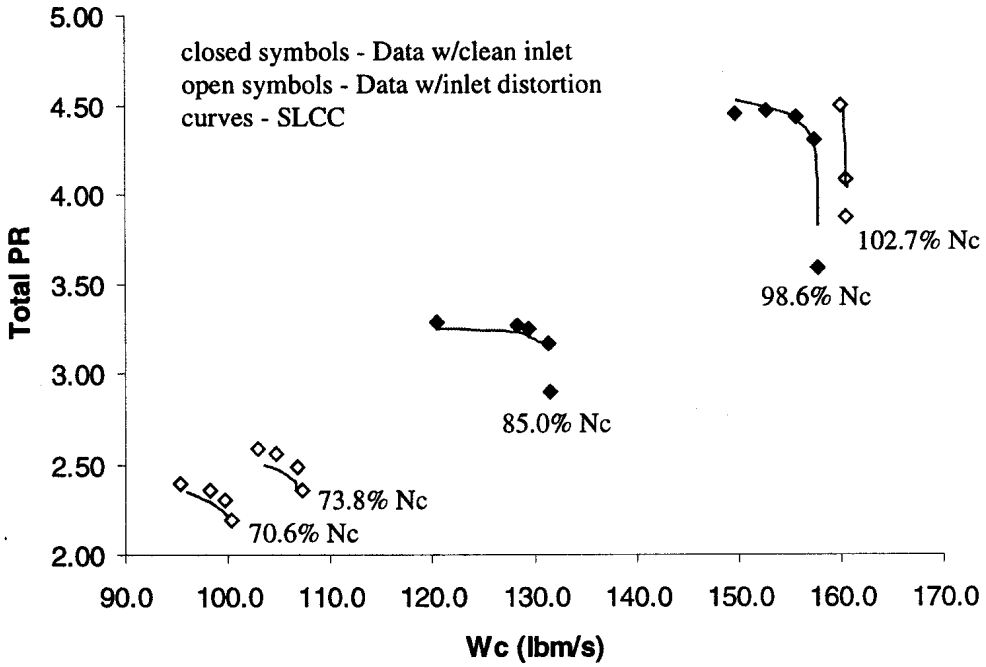

Figure 4.21: SLC Method Prediction Accuracy for Clean and Distorted Inlet Conditions (Boyer, private communication, 2000)

Critical to this study is determination of the positions of equal mass flow annuli through the machine. These positions are calculated by linearly interpolating flow values from probe locations at five radial immersions (RI's), presented in tables 4.3 and 4.4, to the centers of equal mass flow annuli whose radial positions are computed by the SLC code. Table 4.5 gives these computed positions. Note that each operating point creates different streamline positions and that computed positions along the same speed line are identical, to at least the first decimal place. With flow values interpolated to these locations, a single streamline can be followed through the compressor (illustrated in figure 5.2 for immersion 4) making it possible to examine the frequency content and FRF of the corresponding fluid mass.

It is likely that, since the SLC method does not capture circumferential flow variations, the actual streamline positions in the distorted flow machine are different than those calculated. In a compressor whose flow behavior has strong radial dependence, such as the current machine, accurate estimation of streamline position is necessary to implement the prediction scheme of this study. However, it is reasonable to assume that

circumferential distortion does not radically alter streamline radial positions over those of the "clean" inlet condition. This assumption is justified by the radial uniformity of the distortion which therefore lacks significant radial static pressure gradients to cause a shift in streamline positions.

Immersion , in. (from case) → Op. Point ↓	S1 LE RI1	S1 LE RI2	S1 LE RI3	S1 LE RI4	S1 LE RI5	S2 LE RI1	S2 LE RI2	S2 LE RI3	S2 LE RI4	S2 LE RI5
13200 WOD	0.520	1.487	2.443	3.451	4.636	0.326	0.877	1.473	2.036	2.579
13200 NOL	0.521	1.494	2.449	3.455	4.637	0.326	0.878	1.474	2.036	2.578
13200 PE & NS	0.520	1.492	2.442	3.446	4.633	0.321	0.872	1.478	2.043	2.578
9500 WOD	0.480	1.587	2.600	3.607	4.705	0.281	0.88	1.519	2.097	2.612
9500 NOL	0.479	1.589	2.601	3.607	4.705	0.280	0.881	1.52	2.099	2.613
9500 PE	0.473	1.604	2.611	3.621	4.71	0.277	0.883	1.526	2.107	2.615
9500 NS	0.467	1.625	2.632	3.635	4.714	0.272	0.888	1.537	2.117	2.618
9100 WOD	0.487	1.632	2.591	3.617	4.710	0.284	0.901	1.535	2.110	2.617
9100 NOL	0.485	1.635	2.591	3.617	4.710	0.283	0.902	1.537	2.113	2.618
9100 PE	0.483	1.648	2.597	3.621	4.712	0.281	0.907	1.543	2.119	2.620
9100 NS	0.478	1.648	2.608	3.629	4.715	0.277	0.912	1.55	2.130	2.624

Table 4.5: Radial Position of Centers of Equal Mass Flow Annuli, Computed

The SLC code, combined with measured test article data, provides the information necessary to develop the frequency domain model presented herein.

5 Experimental Results and Data Characteristics

Test article measurement and streamline curvature code runs, described in the previous section, provide the data necessary to develop a frequency response function modeling technique. This section discusses specific operating points of the test compressor, relevant data that was acquired, and presents representative data sets in both the time and frequency domains. The influence of rotor speed, blade row aerodynamic loading, span location and distortion type on total pressure distortion amplitude is examined.

5.1 Compressor Operating Points and Distortion Screen Characteristics

For this experiment, a two- stage transonic compressor whose configuration is described in chapter 4 is operated with distortion inducing screens upstream of its inlet. The compressor's mass flow, pressure ratio characteristic map for operation with both clean and distorted inlet flows is shown in figure 5.1. Compared to those with clean inlets, runs with distortion screens in place, indicated by dashed lines, exhibit markedly reduced mass flow for a given rotor speed. The corresponding pressure ratio for a given mass flow is likewise reduced, illustrating the detrimental effect of distortion on overall machine performance.

Data for this study are collected at a total of eleven individual operating points along three speed lines of the test compressor: 9100, 9500 and 13200 (mechanical rpm) which correspond to 68.5%, 71.5% and 99.3% (Nc) respectively, of design speed. Typically, data at four mass flow settings are recorded: WOD- wide open discharge (highest mass flow allowed by downstream valves, see section four), NOL- normal operating line, PE- peak efficiency and NS- near stall (lowest mass flow). Note that for the high-speed line PE and NS points are coincident. Additionally, at this condition the characteristic is nearly vertical, indicating the high sensitivity of blade loading to mass flow at design speed. This is due to the complex interaction of blade incidence angle variations with flow velocities and associated passage shock structures. This sensitivity is typical of modern, highly loaded transonic compressors.

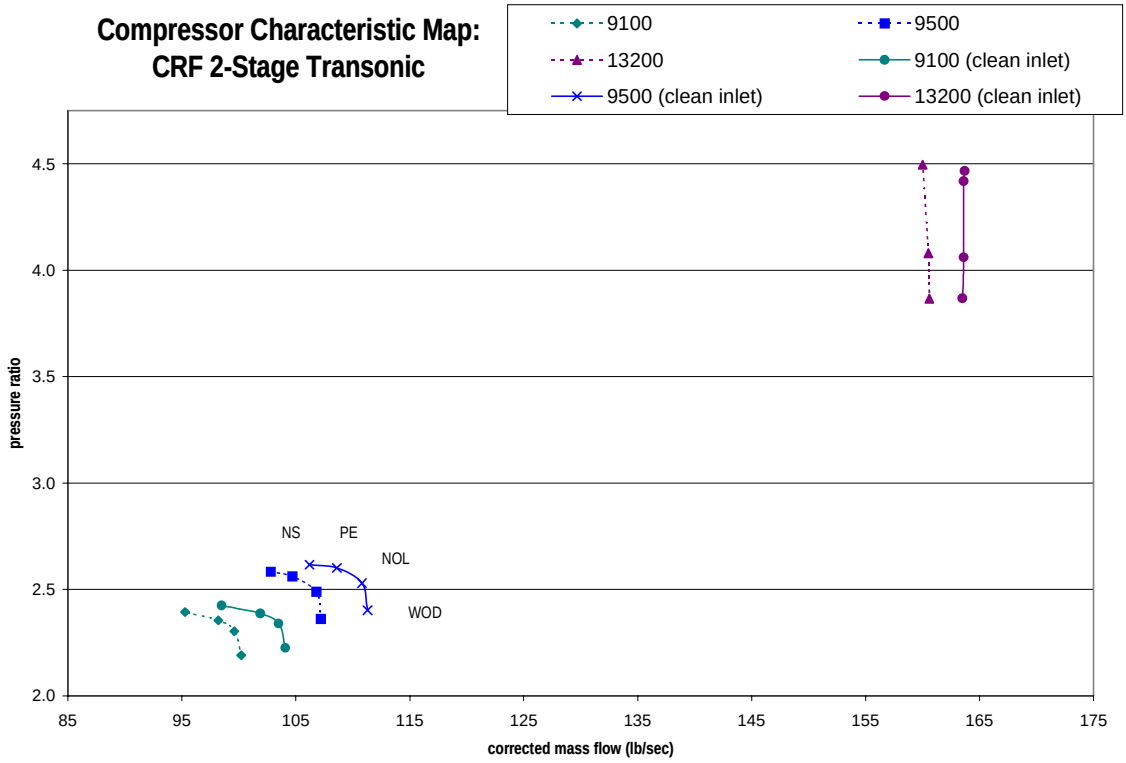

Figure 5.1: Compressor Characteristic Map

Two different distortion-inducing screens are used in the initial phase of this study. Each generates a circumferential, sinusoidal total pressure distortion. A three per-rev screen, pictured in figure 4.9, is used for data collected at 9100 rpm, while an eight per- rev screen is employed at higher rotor speeds. Total pressure deficits and associated operating points at the NOL condition are presented in table 6.1.

Distortion Type	3/rev	8/rev	8/rev
Typ. Max Pt Variation from Mean	3%	6%	18%
Mechanical Speed (rpm)	9100	9500	13200
Percent Rotor Speed	69%	72%	99%
Pressure Ratio	2.3	2.5	4.1
Percent Corrected Mass Flow	63%	67%	103%

Table 5.1: Compressor Characteristics at NOL

5.2 Typical Data Set from a 3/rev Distortion Case

Three per-rev distortion was induced only at a single speed, therefore only four separate data sets from this condition are available, one at each aerodynamic loading point. A typical inlet total pressure profile is shown in figure 5.2. Areas of low total pressure (green, blue) correspond to portions of high density screen, visible in figure 4.9. The distortion is fairly axisymmetric, and does not have sharp pressure transitions, indicating that the intent of the sine wave screen is being realized.

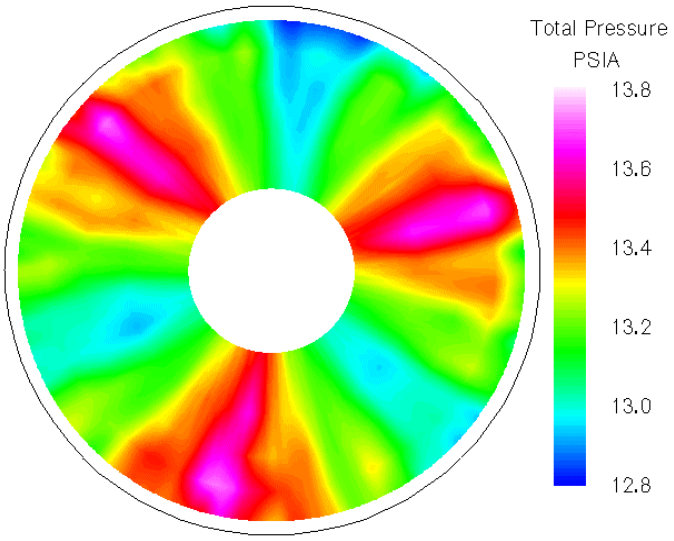

Figure 5.2: Typical 3/rev Inlet Annular Total Pressure Distribution (private communication, Williams, 2000)

Individual rotor blades moving through the stationary annular distribution create equivalency between the spatial domain (laboratory coordinate frame) and the time domain (rotor coordinate frame). Thus, results presented as a function of circumferential position will interchangeably be referred to as “spatial domain” and “time domain” throughout this report.

Measurements taken at the distortion measurement location, at all five span locations for the NOL operating point are presented in the time domain in figure 5.3, normalized by the average total pressure at this axial station.

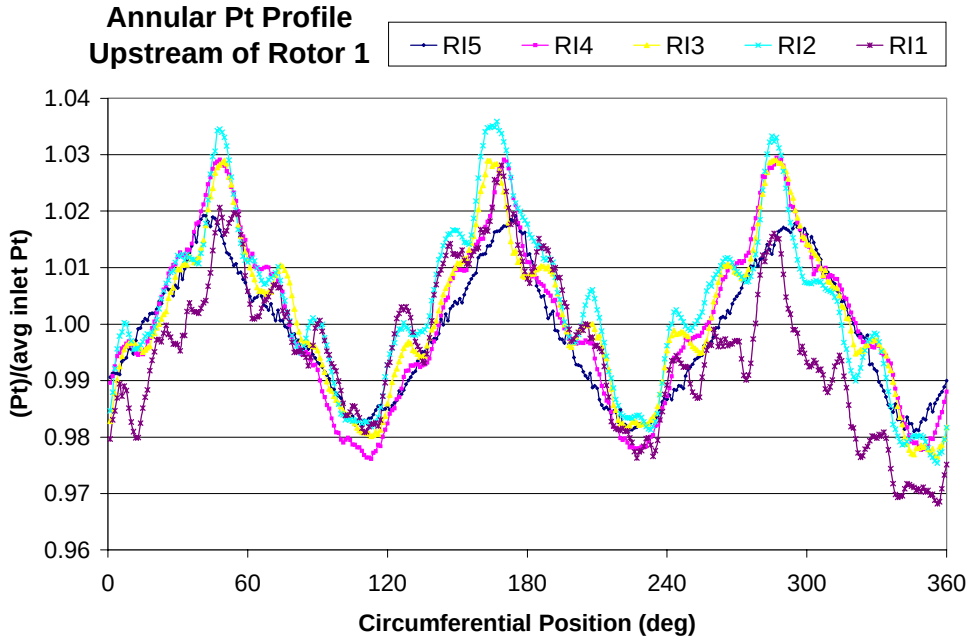

Figure 5.3: Annular Pt Profile Upstream of Rotor 1, 9100 NOL

These distributions are approximately in phase, with nearly the same mean value. They exhibit approximately 5% peak- to peak variations in total pressure.

Using the Fourier Transform techniques outlined in chapter 3, individual frequency components of the distortion profile can be examined. Throughout this report frequency domain magnitude and phase portions are presented separately, with individual frequency components (in 1/rev increments) along the horizontal axis. Magnitude values are the amplitude, in psia, of individual frequency components.

The frequency domain representation of the inlet distortion distribution at the 69% speed, NOL condition is shown in figures 5.4 and 5.5 to the Nyquist- limited 180th component frequency, the highest frequency calculated in this study.

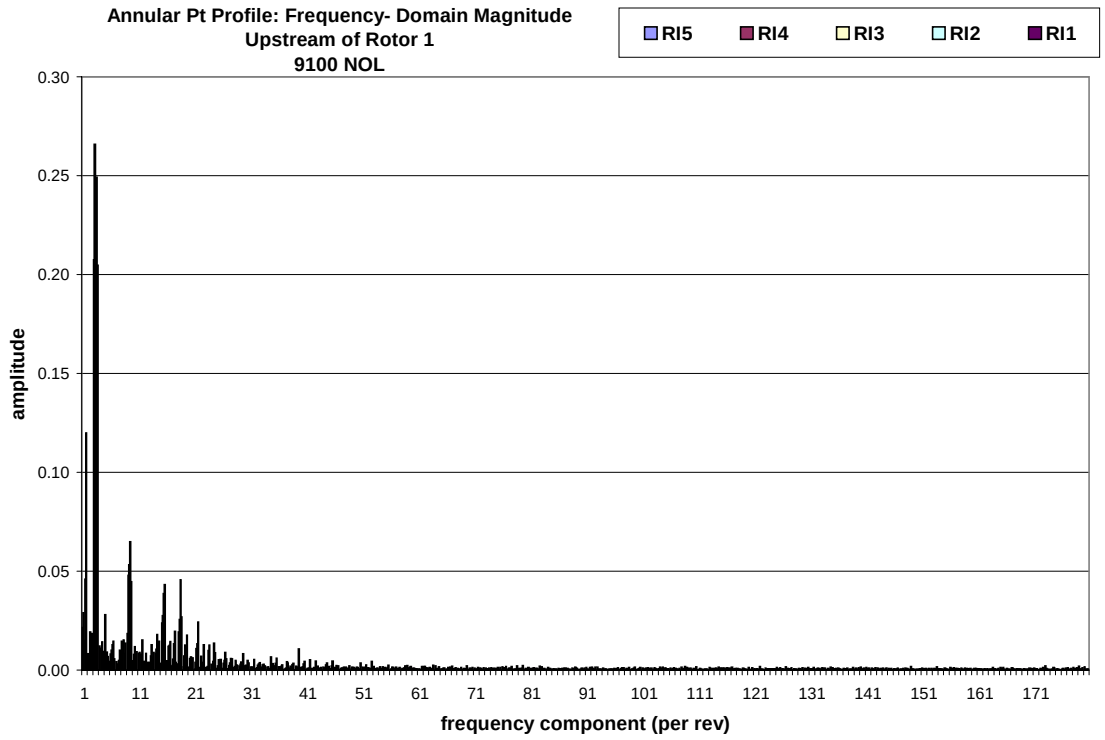

Figure 5.4: Annular Pt Profile Upstream of Rotor 1, Frequency Component Magnitudes, 9100 NOL

Examination of figure 5.4 reveals that frequency magnitudes decay quickly after approximately the 25th component. This indicates that the sampling rate is high enough to capture relevant frequencies (in fact for these low engine order distortions, a much lower sampling rate would suffice) and supports the argument that anti-aliasing filters are not necessary. As expected, phase values in figure 5.5 do not decay at higher frequencies.

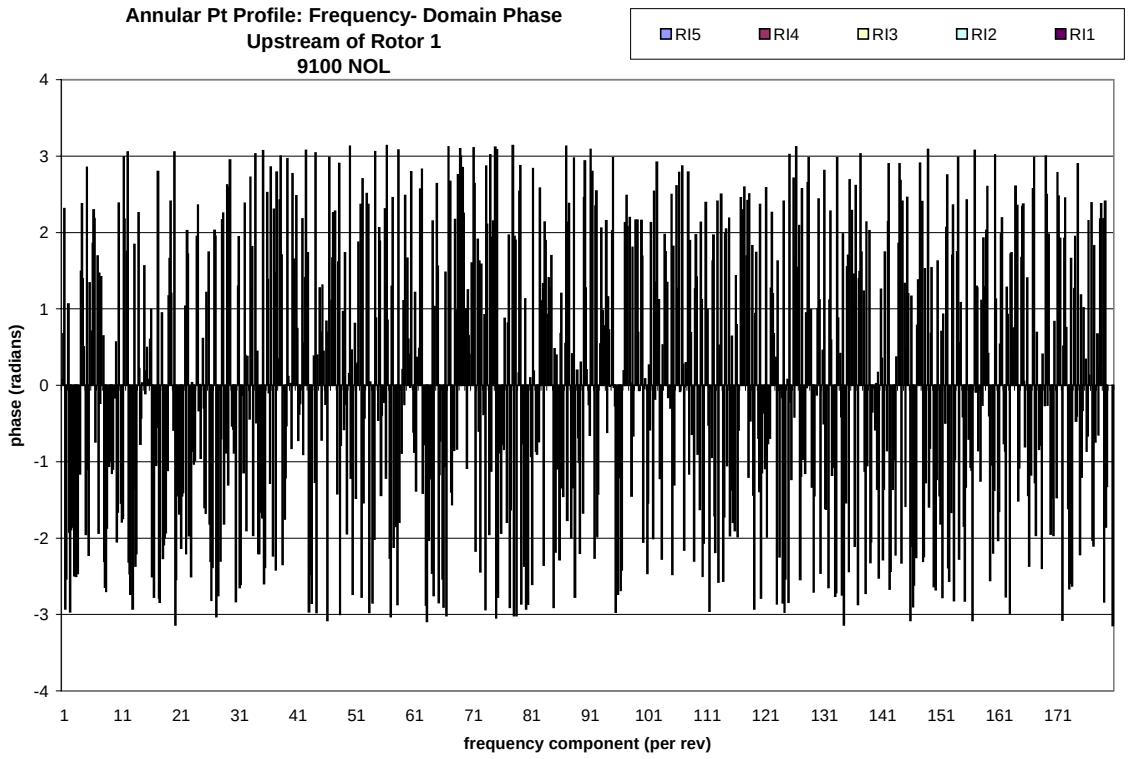

Figure 5.5: Annular Pt Profile Upstream of Rotor 1, Frequency Component Phases, 9100 NOL

Not shown on these plots is the zeroth frequency (DC component). Since the unsteady variation is a small percentage of the average pressure, the required graph scale if the DC portion was presented would compromise the resolution of the remaining frequencies.

Knowing that higher frequencies do not contain magnitudes above the noise floor, figures 5.4 and 5.5 are reproduced as figures 5.6 and 5.7, respectively, showing only component frequencies 1 through 24. Unlike the previous figures, individual data sets from the five radial immersions (RI's) are now visible.

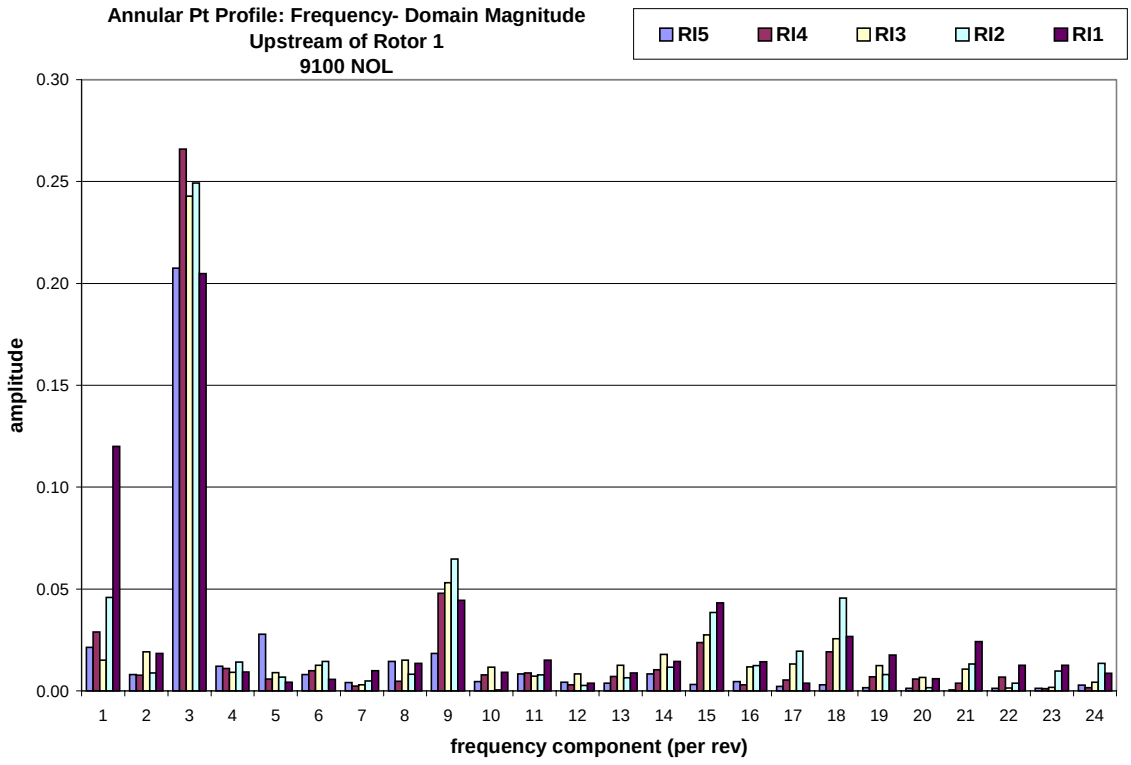

Figure 5.6: Annular Pt Profile Upstream of Rotor 1, Freq. Component Mag. (1-24), 9100 NOL

Figure 5.6 shows the dominant 3/rev component (expected, since this is a 3/rev distortion), as well as the 3rd (9/rev), 5th (15/rev) and 6th (18/rev) harmonic peaks. Note that the first frequency (1/rev) has relatively high magnitude, compared to that of other non- harmonics. This is due to an unavoidable operational error caused by the screen rotator not rotating precisely about the compressor's longitudinal axis. At all frequencies, magnitude values across the blade span from RI1 (near the case) to RI5 (near the hub) are relatively constant indicating a reasonably radially- uniform distortion.

Phase data continues to be scattered, except for frequency components with relatively large magnitudes, such as 3/rev and 9/rev, which remain fairly consistent across the span; this is consistent with the phasing shown in the time domain presentation.

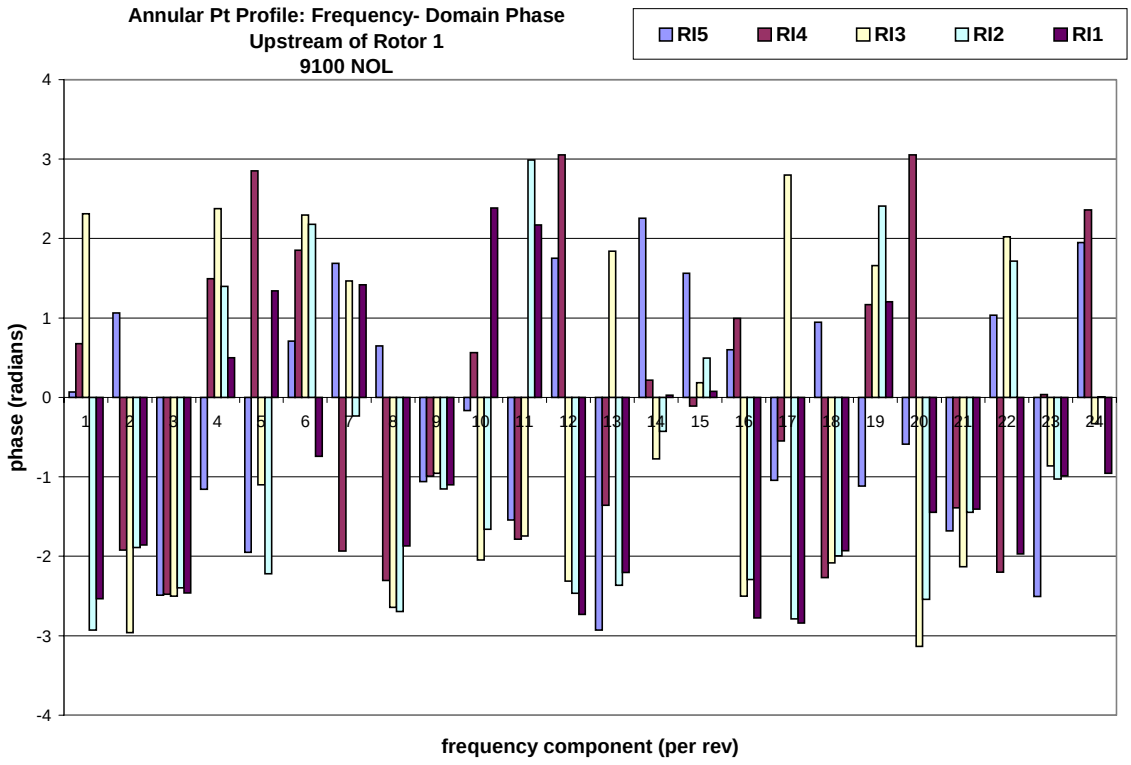

Figure 5.7: Annular Pt Profile Upstream of Rotor 1,Freq. Component Mag. (1-24), 9100 NOL

After passing through the first stage rotor, the flow is next measured at the leading edge of the first stage stator row. Time domain data, figure 5.8, show that the rotor weakly amplifies the distortion at most span locations; although the tip region exhibits some attenuation. Much of the high frequency "buzz", present upstream, is eliminated, especially near the hub. This is also seen in the component frequency magnitude presentation.

One hundred and eighty frequencies of the annular total pressure distribution, interpolated to positions determined from SLC analysis, are shown in figures 5.9 and 5.10. The action of the rotor is to further reduce the relative amplitudes of higher frequencies, further justifying the examination of only lower frequency components.

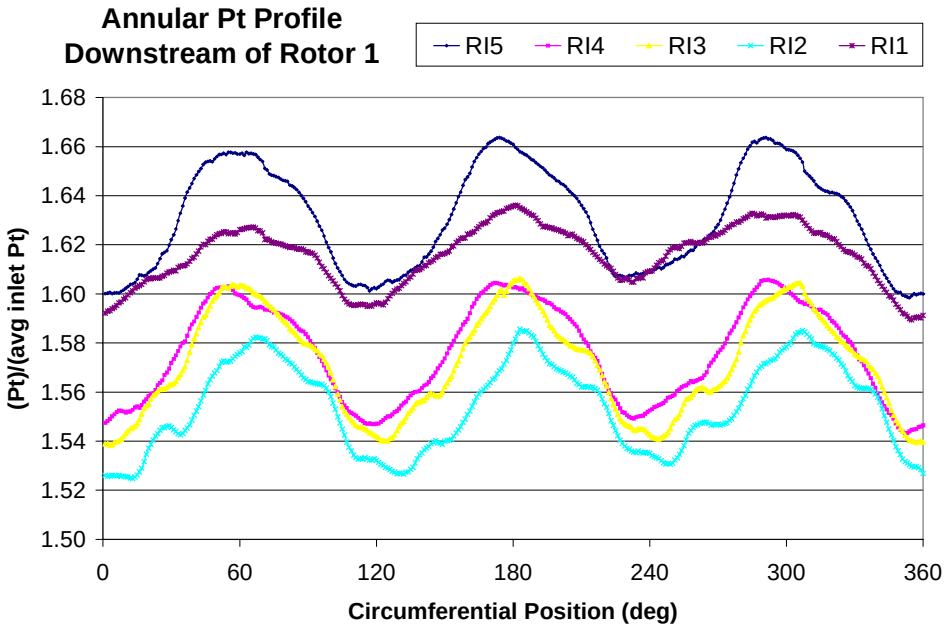

Figure 5.8: Annular Pt Profile Downstream of Rotor 1, 9100NOL

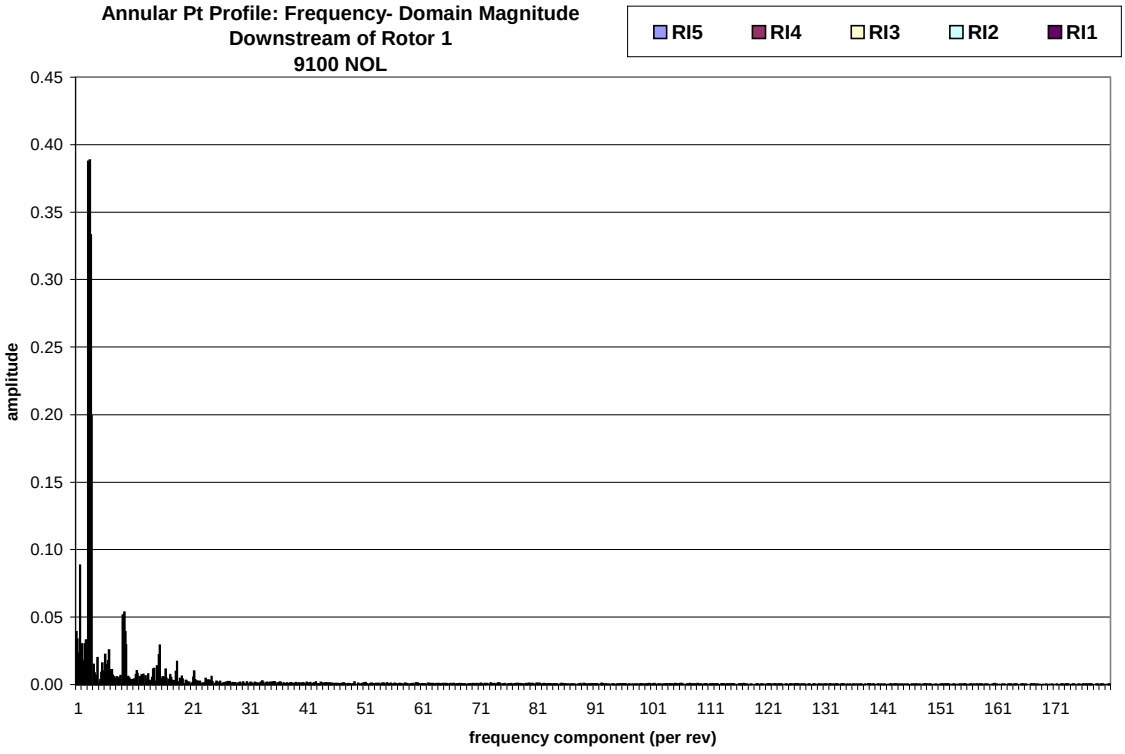

Figure 5.9:Annular Pt Profile Downstream of Rotor 1, Frequency Component Magnitudes,9100 NOL

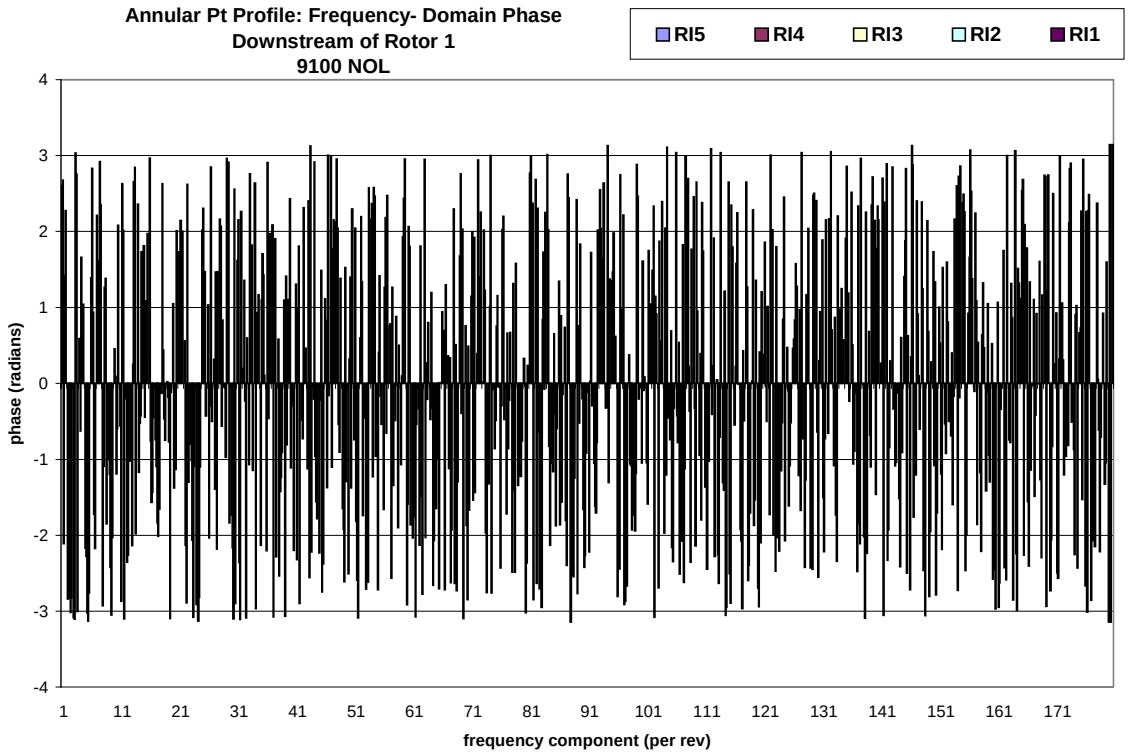

Figure 5.10:Annular Pt Profile Downstream of Rotor 1, Frequency Component Phases, 9100 NOL

The more relevant first twenty-four component frequencies of rotor exit data are presented in figures 5.11 and 5.12. Higher frequency attenuation is also evident in this plot, including attenuation of higher harmonics. The second harmonic is now visible, while the third is still strong, with lower values at the fifth and sixth. Phase data continues to be erratic, now showing the second and third radial immersions to be phase- shifted (at the third frequency component) from the other three distributions. This is also seen in the time domain plot.

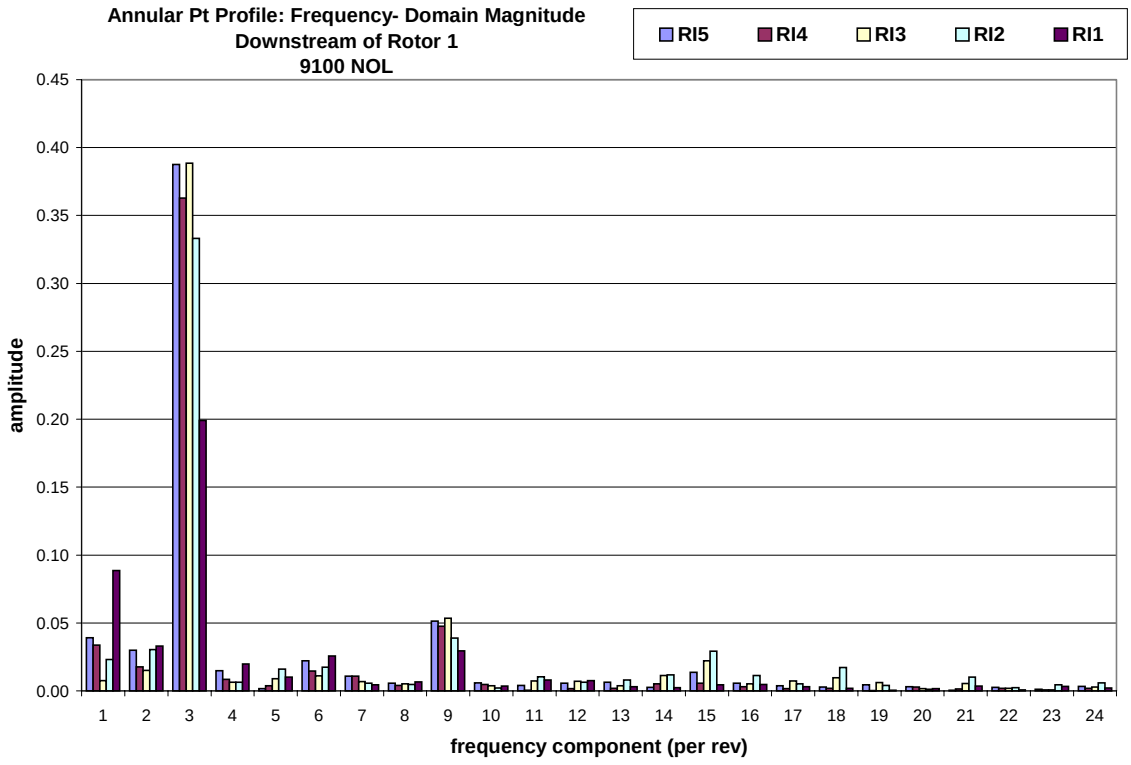

Figure 5.11: Annular Pt Profile Downstream of Rotor 1,Freq.Component Mag. (1-24), 9100 NOL

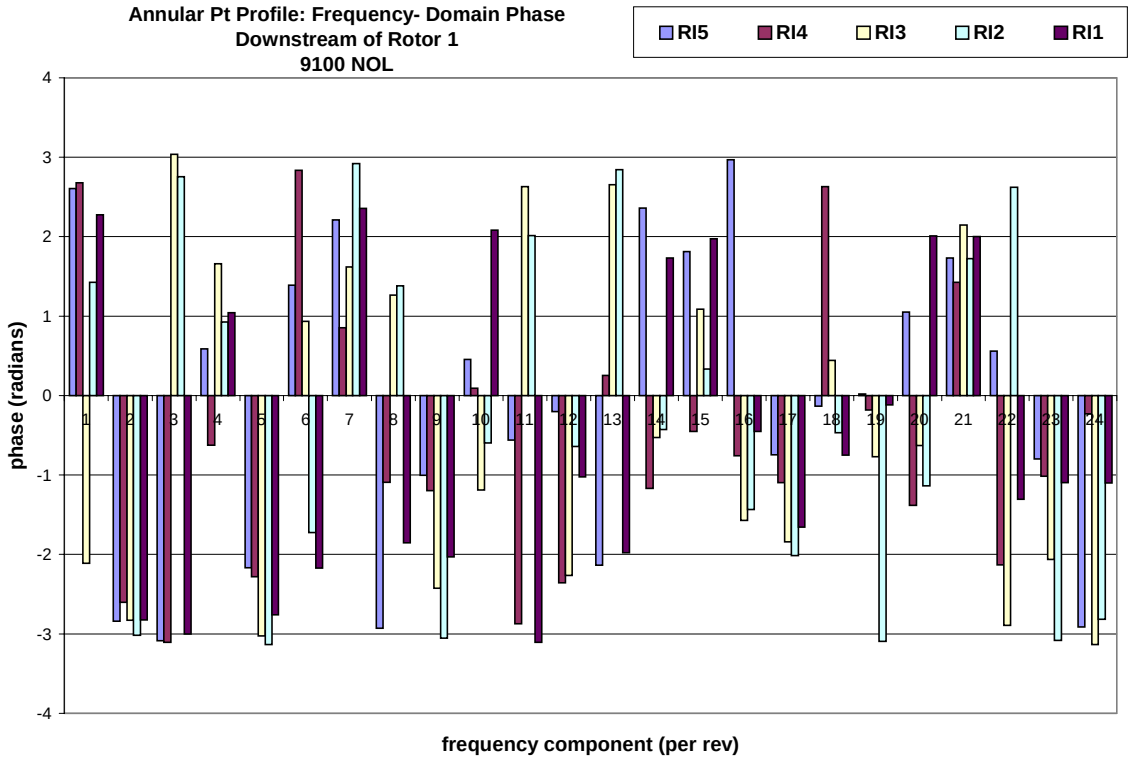

Figure 5.12: Annular Pt Profile Downstream of Rotor 1,Freq.Component Phase (1-24), 9100 NOL

A lack of instrumentation directly upstream of the second stage rotor forces the use of first- stage stator leading edge data as surrogate rotor 2 inlet data. This is, in fact, a reasonable assumption, given that total pressure is the only flow property being examined. The stator row would not be expected to markedly change the average value or peak-to-peak variation of total pressure.

Second stage rotor downstream annular distributions of interpolated total pressure values corresponding to centers of the same five equal mass flow annuli previously examined are presented in figure 5.13. Distortion amplification occurs through the second rotor, with peak- to- peak variations nearing 10% of inlet average pressure for streamline locations near the hub. Locations toward the tip experience less amplification. Some higher- frequency content has been added, especially near the hub. Overall, 3/rev distortion is still strongly dominant. This is seen in the frequency domain representation, figures 5.14 and 5.15.

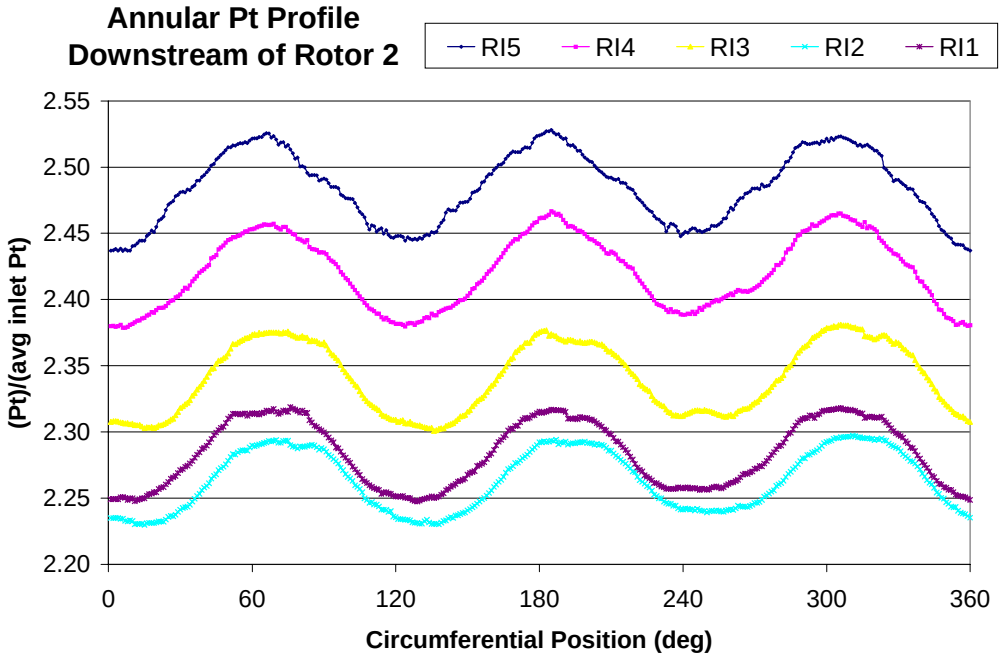

Figure 5.13: Annular Pt Profile Downstream of Rotor 2, 9100NOL

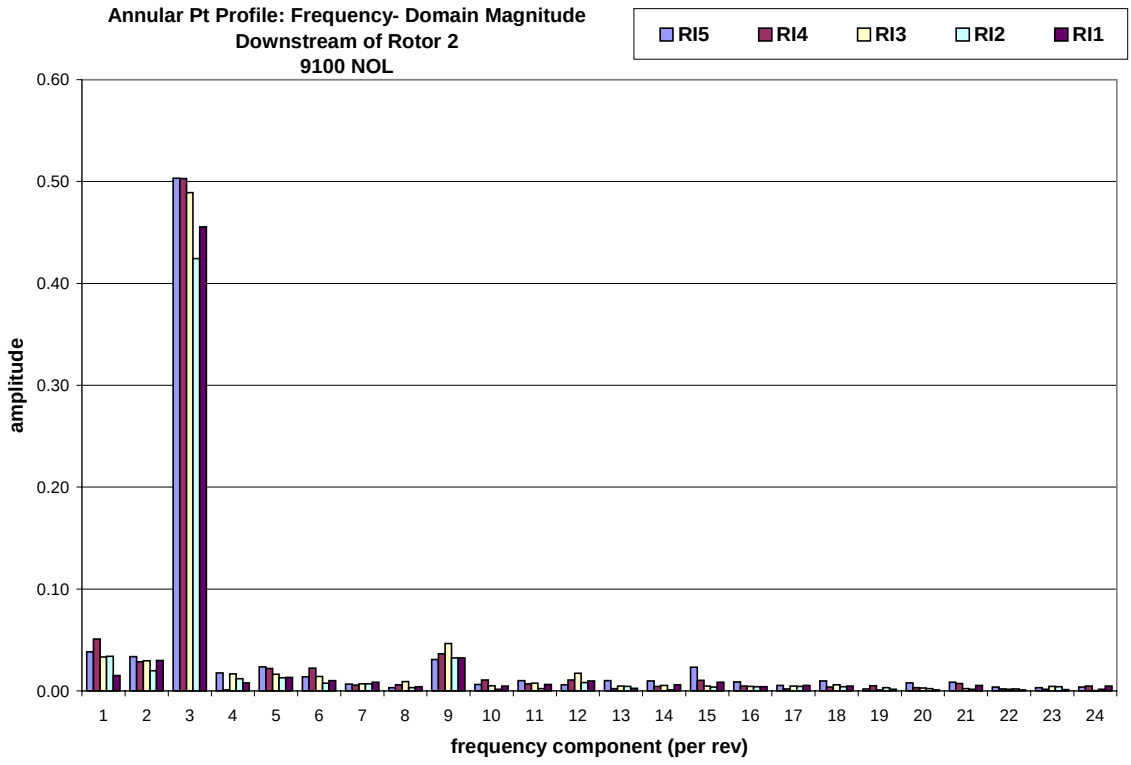

Figure 5.14: Annular Pt Profile Downstream of Rotor 2,Freq.Component Mag. (1-24), 9100NOL

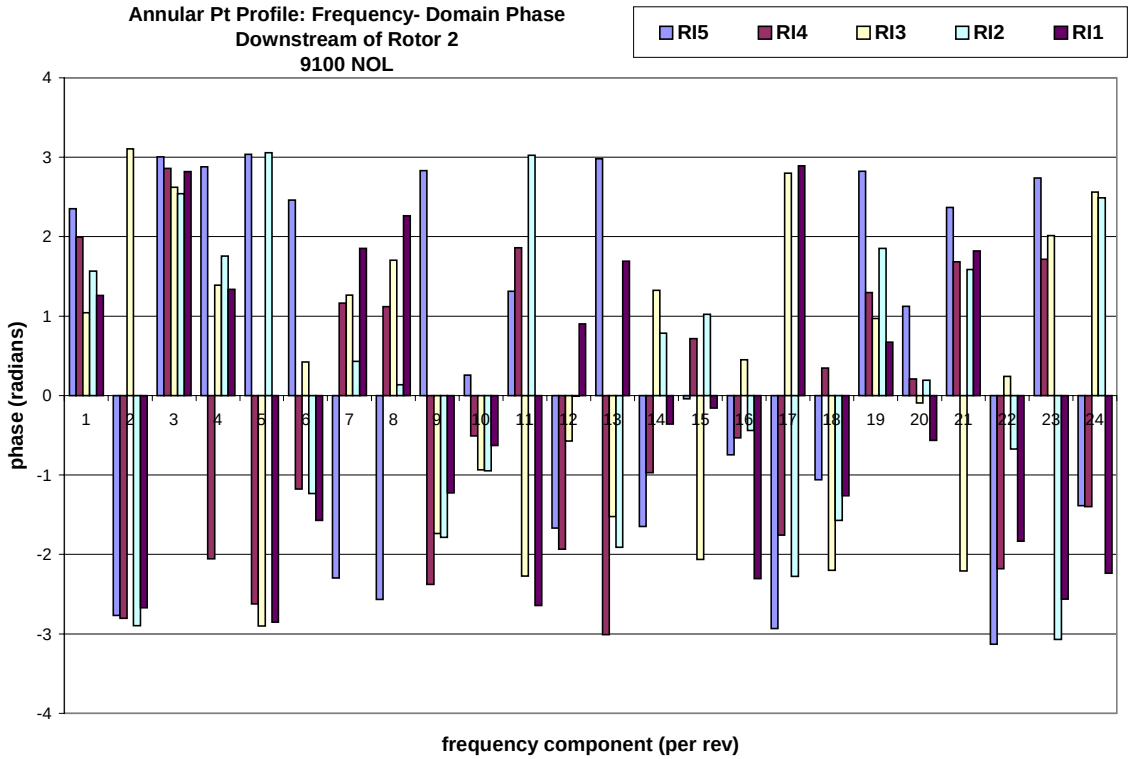

Figure 5.15: Annular Pt Profile Downstream of Rotor 2,Freq. Component Phase (1-24), 9100 NOL

5.3 Typical Data Set from an 8/rev Distortion Case

Qualitatively, data taken from an 8/rev distortion is similar to that taken from a 3/rev case. The dominant, or primary, frequency shifts from the third to the eighth component frequency, and for the presented data, the peak-to-peak variation in total pressure is much larger than it was in the previous case. A typical full annular inlet total pressure distribution for a part- speed case is presented in figure 5.16. Like that for the 3/rev case, the distortion is relatively axisymmetric.

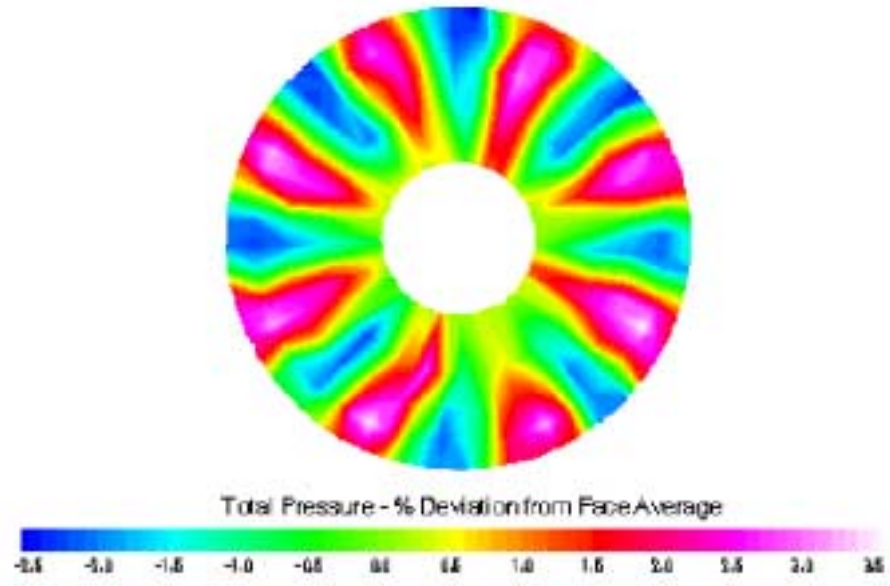

Figure 5.16: Typical 8/rev Inlet Annular Total Pressure Distribution (private communication, Williams, 2000)

Figure 5.17 shows the compressor inlet total pressure distribution in the time domain at five radial positions for data taken at the NOL operating point at the high speed (13200rpm, 99.3% Nc) condition. Again, all time domain values are normalized by span average inlet total pressure. Typical peak-to-peak total pressure variation is approximately 30%, except at the center of the flow, RI 5, where it is near 10%. This is attributed to the distortion screen's construction. All eight distorted segments and the remaining eight "clean" segments meet at the screen's hub where they are tied to a center

wire plug. This configuration creates high flow blockage, preventing the creation of truly undistorted flow in this area, thereby reducing the resulting pressure fluctuation.

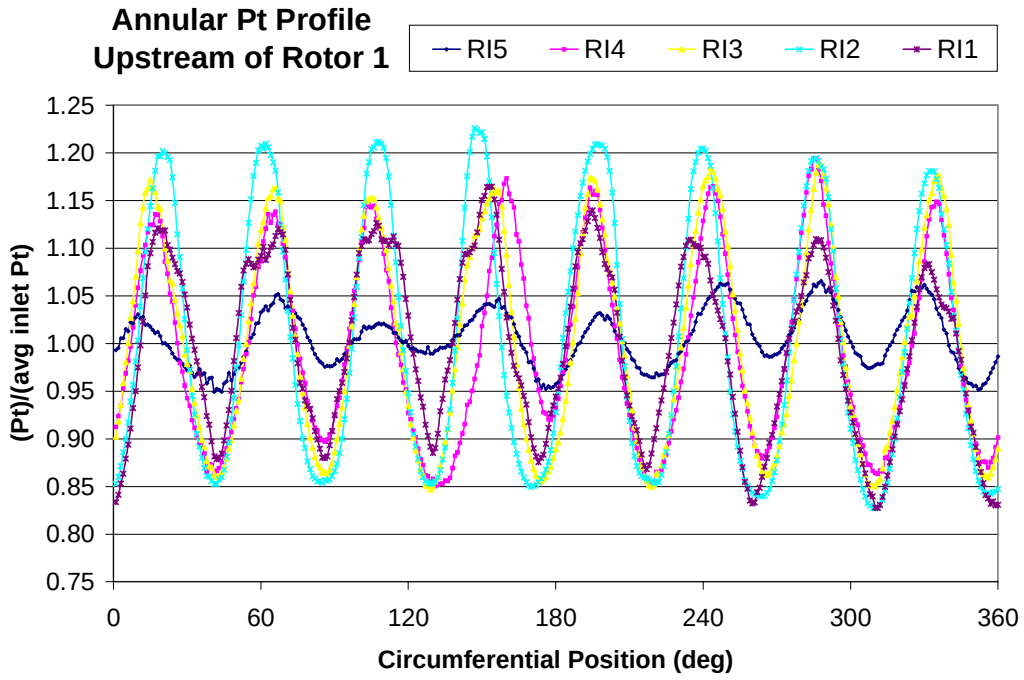

Figure 5.17: Annular Pt Profile Upstream of Rotor 1, 13200 NOL

All computed frequency components of the inlet total pressure distortion are presented in figures 5.18 and 5.19. Like those of the 3/rev distortion, component magnitudes decay quickly and are close to the noise floor by approximately the 30th per-rev, indicating that the sampling rate is sufficient. At the full frequency resolution, phase data continues to be indiscriminate, although as previously seen, high frequency component phases do not appear to decay. Since signal magnitude is very low at high frequencies, the majority of phase scatter is attributable to noise.

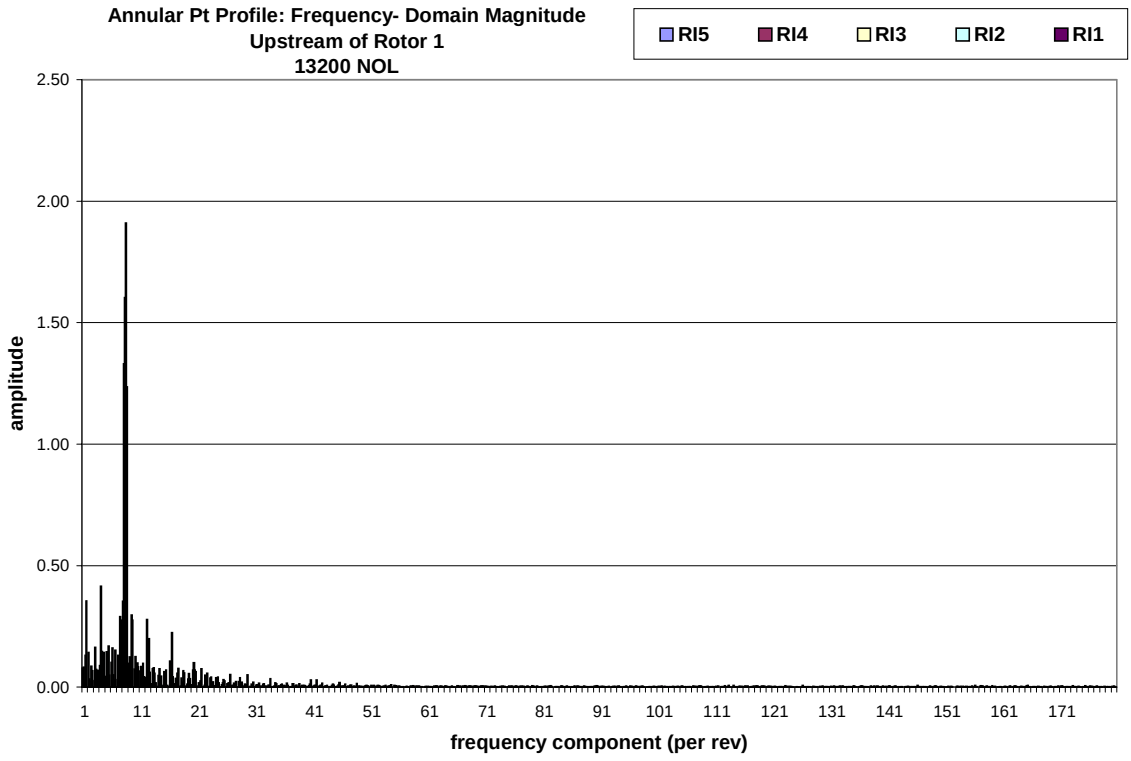

Figure 5.18: Annular Pt Profile Upstream of Rotor 1, Freq. Component Magnitudes, 13200 NOL

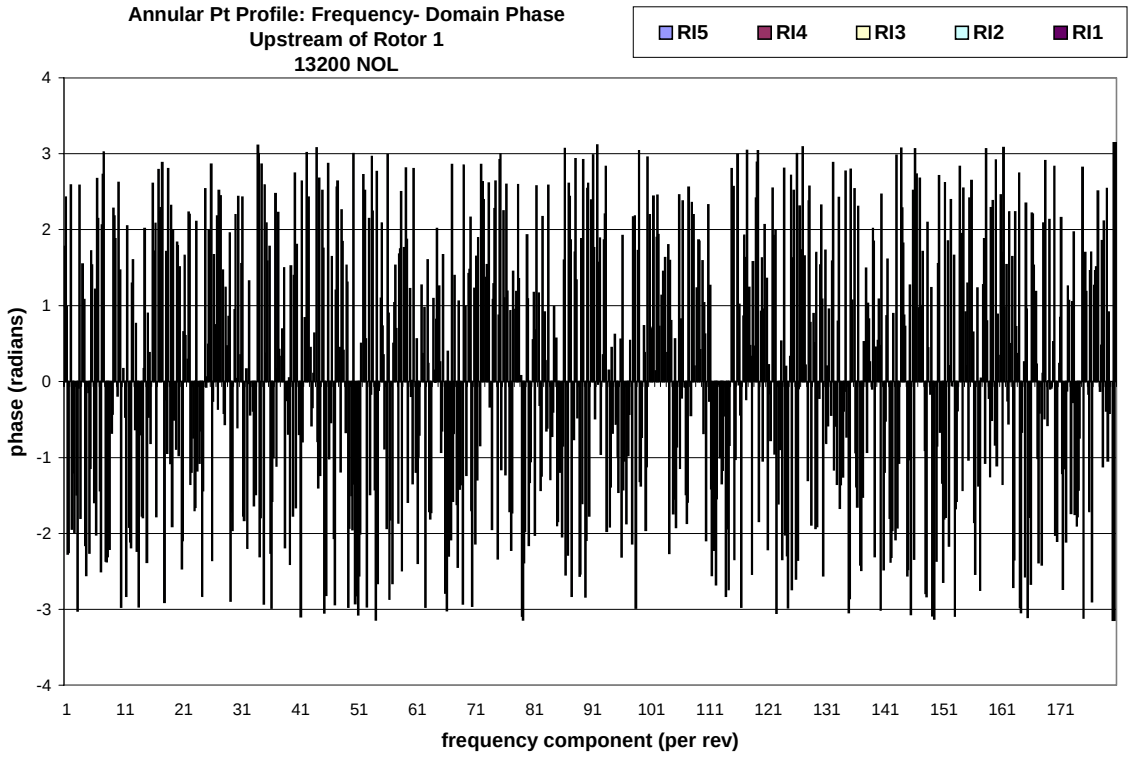

Figure 5.19: Annular Pt Profile Upstream of Rotor 1, Freq. Component Phase, 13200 NOL

Closer examination of the first twenty- four component frequencies in figures 5.20 and 5.21 reveal the expected dominance of the eighth magnitude component frequency and the common behavior of the eighth phase component. Harmonics are not as visible for this distortion as they were for the previous case, although magnitudes of the ½ harmonic (4/rev) and second harmonic (16/rev) are higher than those of neighboring frequencies. The third harmonic (24/rev) does not show appreciable magnitude. Additionally, substantial variation of the primary frequency magnitude exists along the span. The smaller peak- to- peak pressure fluctuation at RI5, also seen in the time domain, is evidenced here by the frequency component's reduced amplitude. Phase data continues to appear scattered, although uniformity across the span is found at the dominant frequency.

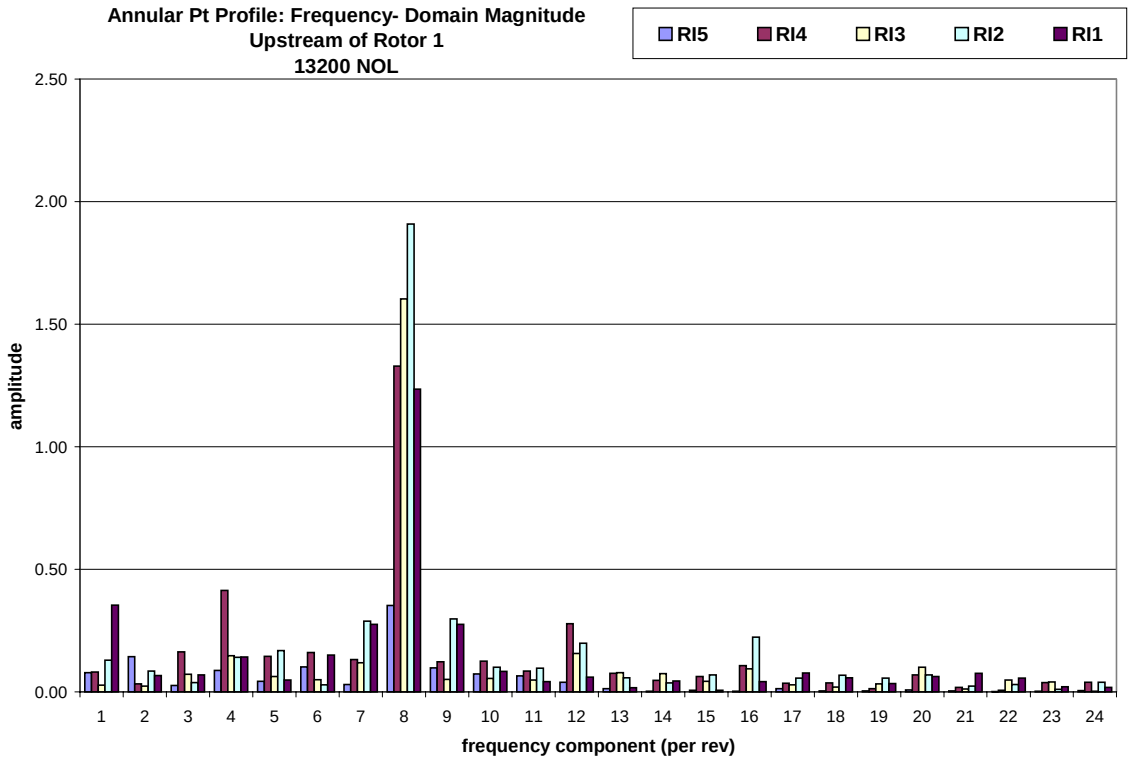

Figure 5.20: Annular Pt Profile Upstream of Rotor 1, Freq. Component Mag. (1-24), 13200 NOL

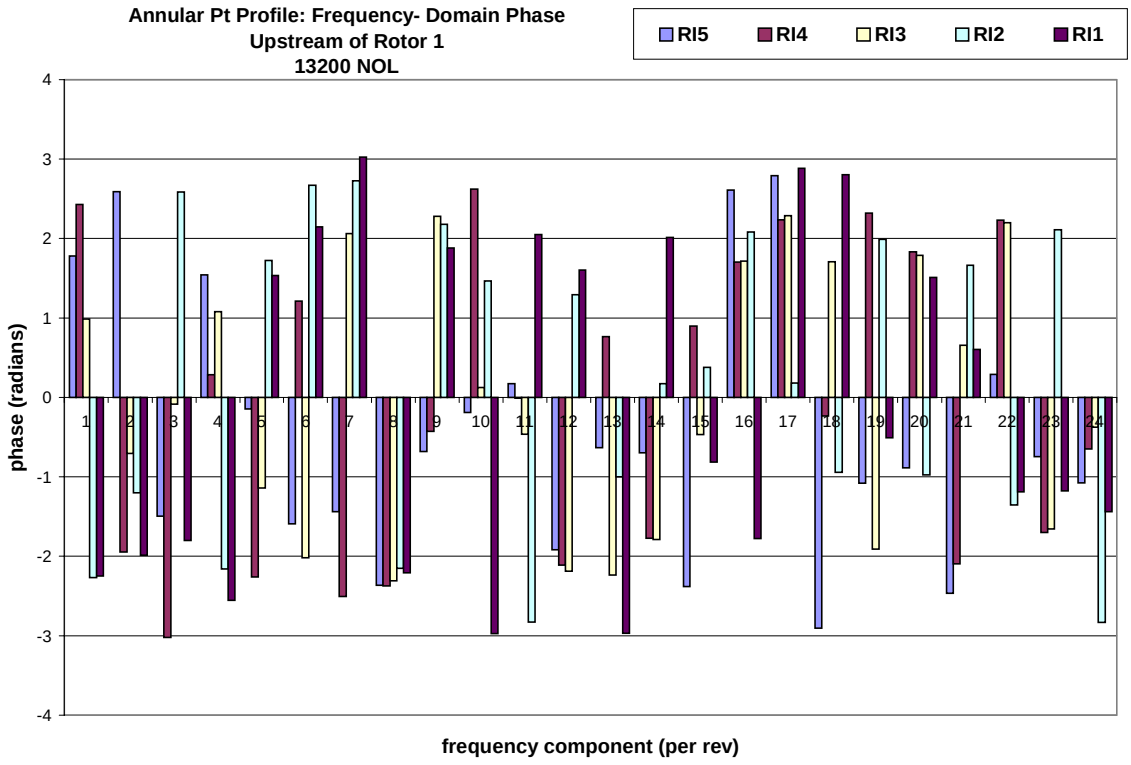

Figure 5.21: Annular Pt Profile Upstream of Rotor 1, Freq. Component Phase (1-24), 13200 NOL

As illustrated by the first stage rotor exit data, figure 5.22, the action of the rotor is not uniform across the span, imparting different frequency amplitudes and phase shifts at each RI. Frequency attenuation through the rotor is strong, reducing the peak-to- peak distortion amplitude from approximately 30% to less than 10%, as a percentage of mean total pressure. Radial positions near mid span experience the largest attenuation, with less occurring near the tip. Distortion phasing across the blade span is not constant, although the 5^{th}, 4^{th} and 1^{st} RI's appear to have similar phasing. A more accurate account is gained through examination of the data's frequency domain representation.

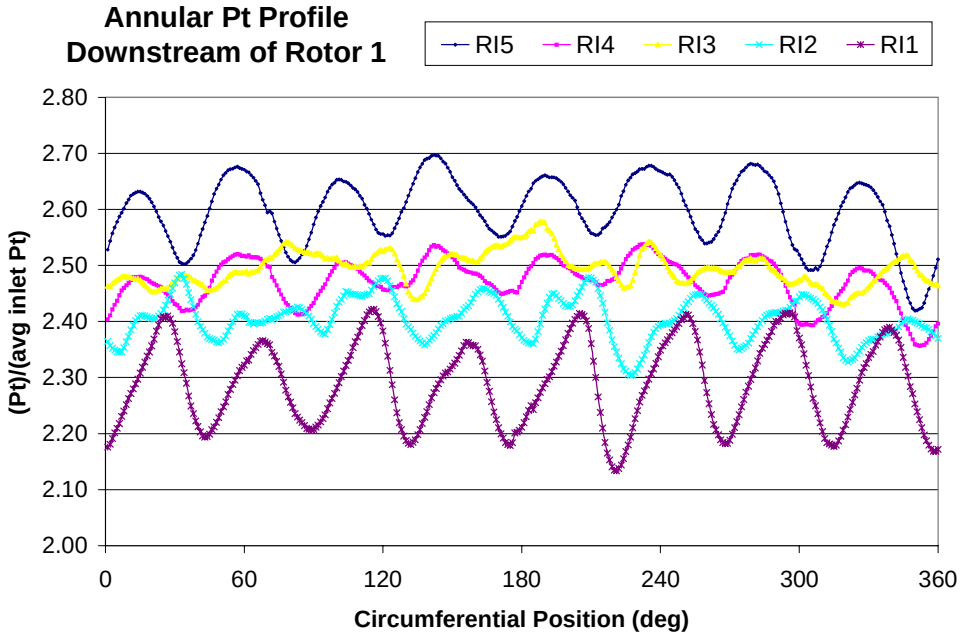

Figure 5.22: Annular Pt Profile Downstream of Rotor 1, 13200NOL

Figures 5.23 and 5.24 give the magnitude and phase of the first twenty-four component frequencies of the distortion annular distribution at the first stage stator leading edge. Behavior at higher frequencies is similar to that upstream of the rotor, therefore plots of 180 component frequencies are omitted for brevity.

The component frequency magnitude plot, figure 5.23, reveals that the rotor has strengthened the relative amplitudes of both the ½ and second harmonic. As also seen in the time domain plot, primary frequency magnitudes across the span are markedly different, especially at RI3, which shows strong attenuation.

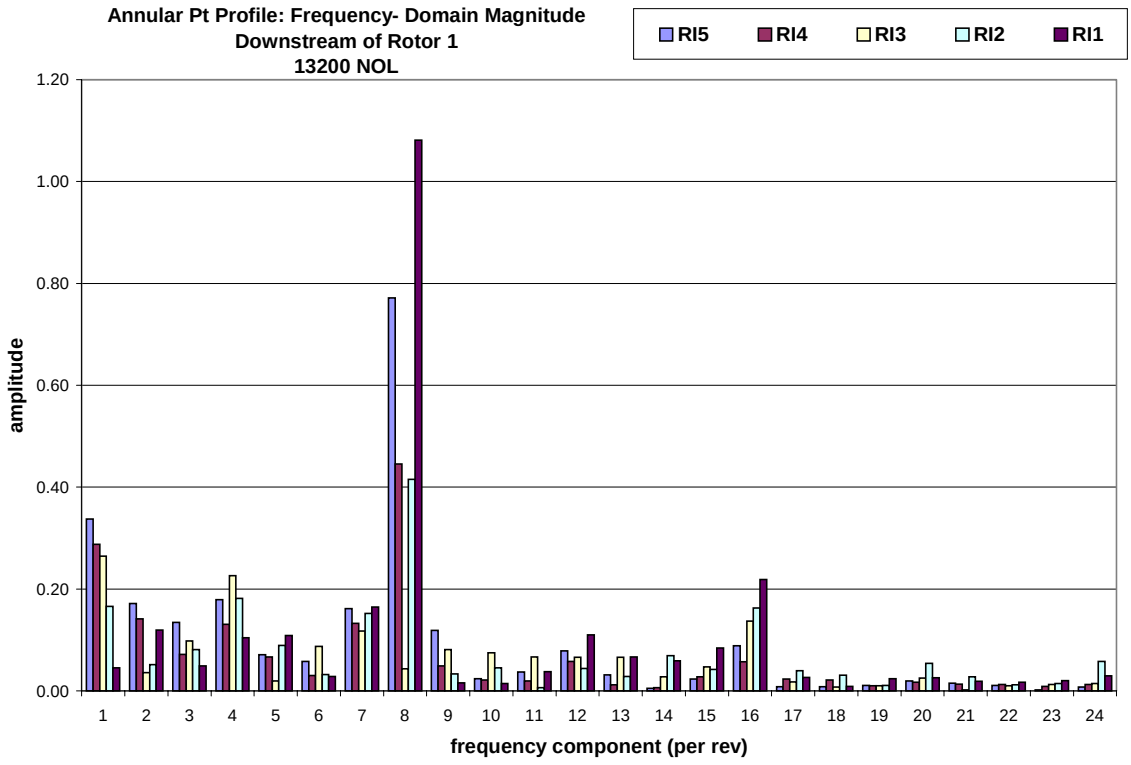

Figure 5.23: Annular Pt Profile Downstream of Rotor 1,Freq.Component Mag. (1-24), 13200NOL

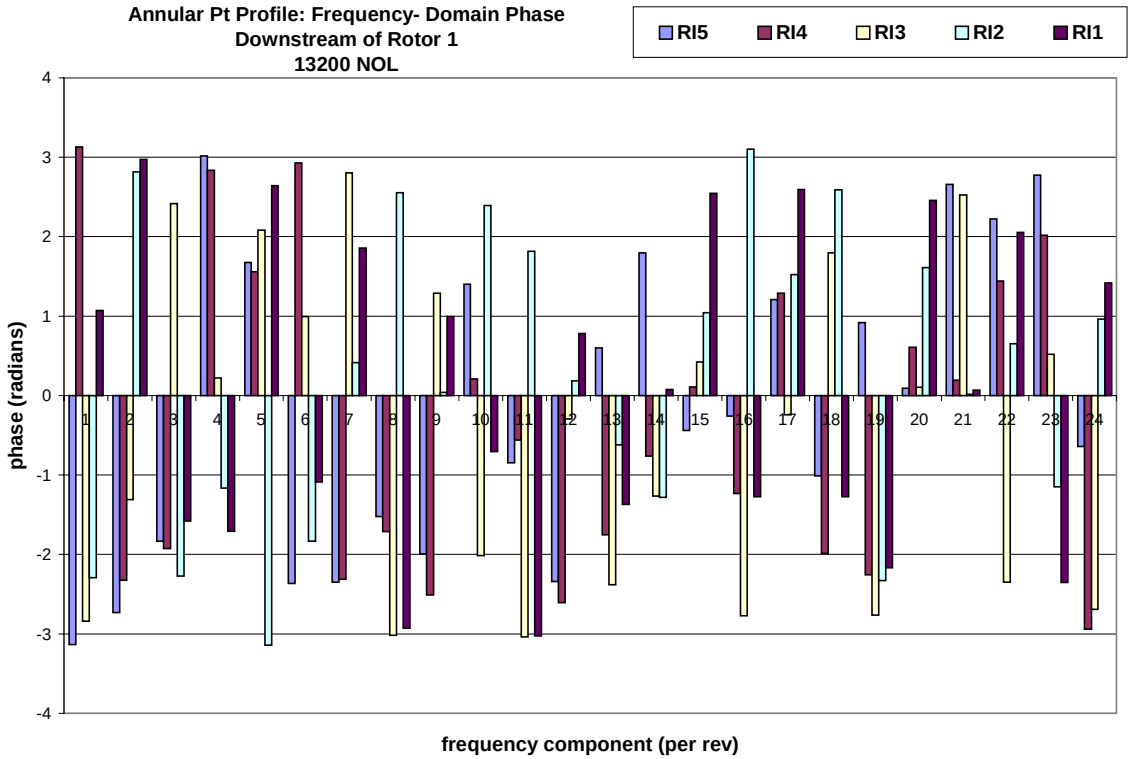

Figure 5.24: Annular Pt Profile Downstream of Rotor 1,Freq.Component Phase (1-24), 13200NOL

The phase plot, figure 5.24, shows very different phases at the primary frequency, which is manifested in the time domain plot as "misalignment" of the traces. This is in contrast to figure 5.12, which showed that the effect of the first stage rotor in the previous operating condition is to produce nearly uniform spanwise phase shift. (In figure 5.12, the absolute values of phase shift at all spans are near π. Note that +/- π are equivalent phase shifts since the transform's basis functions are sine waves.)

Second- stage rotor exit time domain data is presented in figure 5.25. Compared to that at the exit of the first rotor, total pressure distortion at this station is further attenuated. The overall action of the compressor is to reduce peak-to- peak variation at most span locations, as a percentage of average inlet total pressure, to approximately 20% from a value of near 30% at the inlet. Stronger attenuation is observed at streamline positions toward the tip. Higher frequency components have been removed from the flow at RI3 and strong primary frequency attenuation occurs near the tip at RI's 2 and 1.

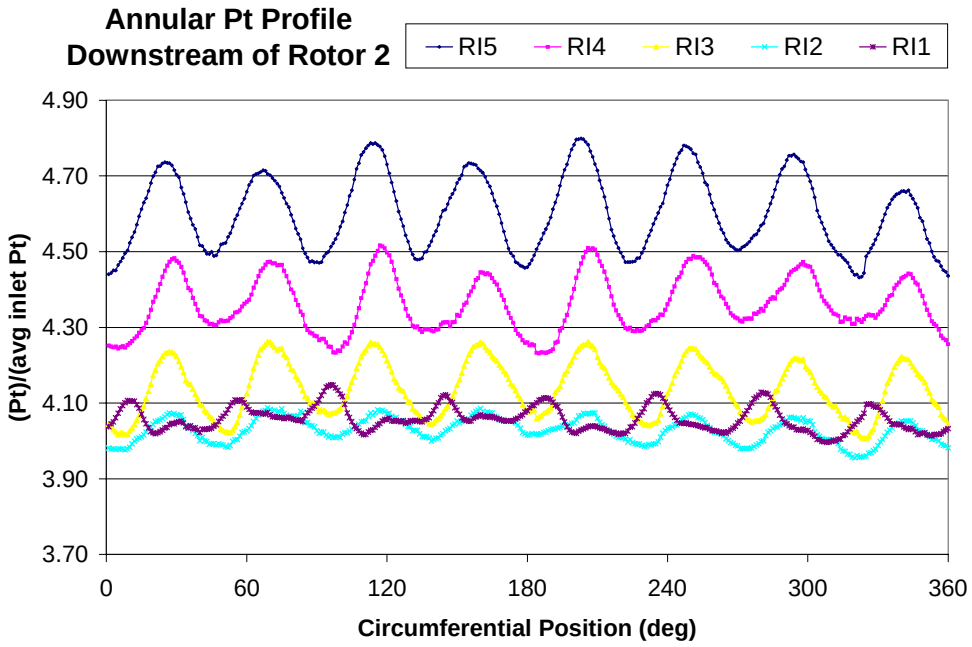

Figure 5.25: Annular Pt Profile Downstream of Rotor 2, 13200NOL

Examination of the frequency domain representation of rotor 2 exit total pressure distribution, figures 5.26 and 5.27, reveals that the second stage rotor increases the

relative magnitude of the second harmonic, as well as causing greater spanwise differences in the primary frequency magnitudes. As was seen in the previous distortion case, typically neither individual rotors nor the compressor amplify non-harmonic component frequencies.

Distortion at RI1 is shifted nearly $\pi/2$ radians relative to the other streamline positions, manifested in the time domain as a lack of peak alignment with the other four RI's and in the frequency domain as a discrepancy in phase value at the primary component frequency.

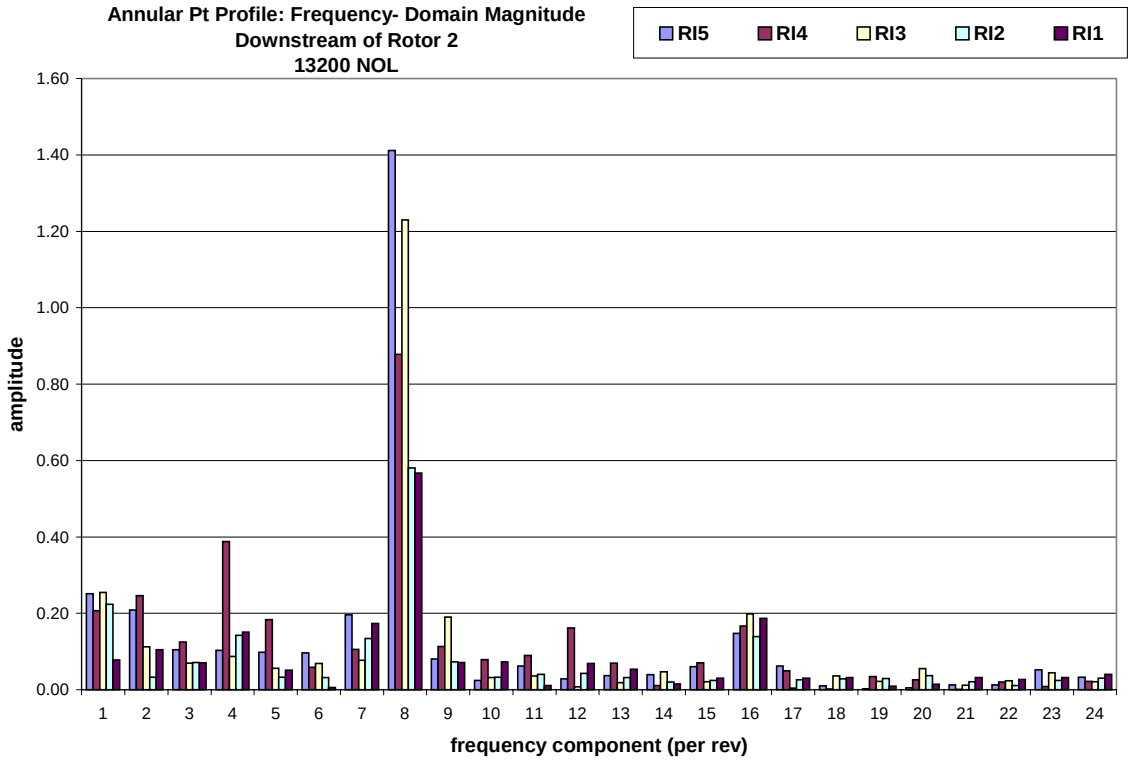

Figure 5.26: Annular Pt Profile Downstream of Rotor 2,Freq.Component Mag. (1-24), 13200NOL

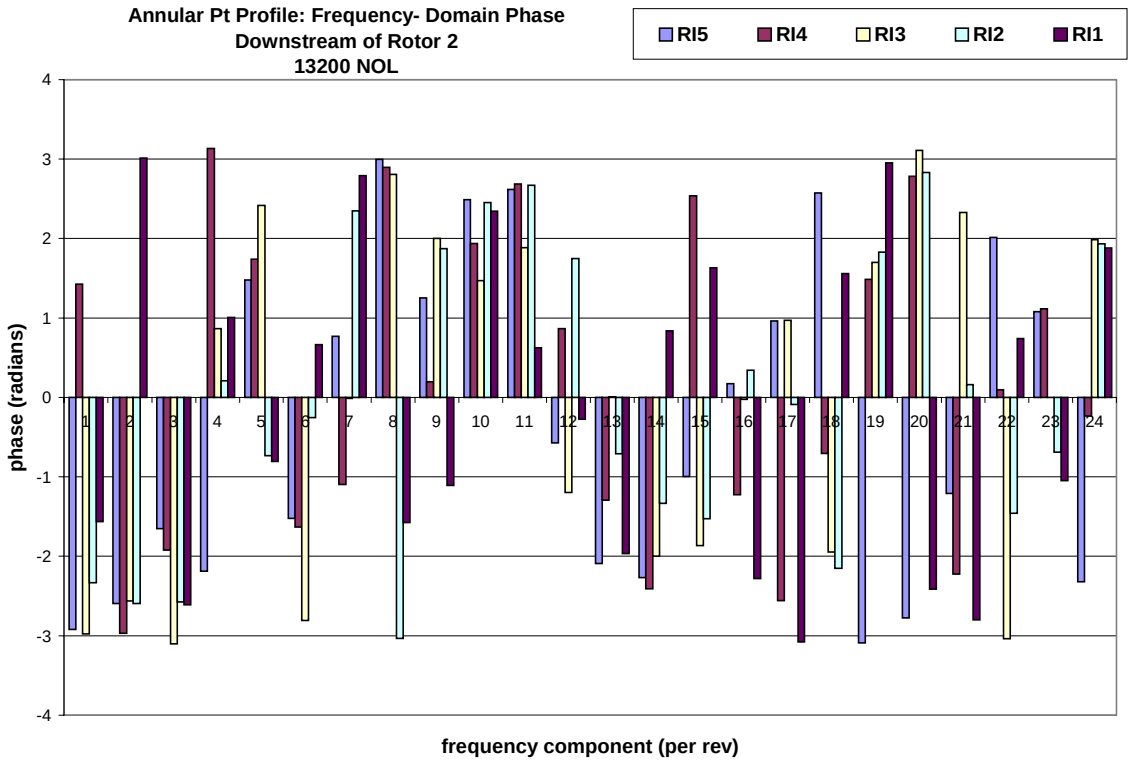

Figure 5.27: Annular Pt Profile Downstream of Rotor 2,Freq.Component Phase (1-24), 13200NOL

5.4 Primary Frequency Magnitude as a Function of Axial Position and Blade Row Aerodynamic Loading

Further analysis of frequency domain data provides information regarding distortion amplification (or attenuation) through each rotor. The change in primary frequency is discussed here, since it has the greatest bearing on the overall shape of the distortion. Other frequency components are examined later in this work.

Primary frequency magnitudes at each of the three axial measurement locations, with five traces (one for each radial position) at each aerodynamic loading level are presented for three rotor speeds. Frequency magnitudes are normalized by the span-average magnitude at 13200NOL. Data at individual loading levels are indicated by color.

Figure 5.28 shows primary frequency magnitudes for the 9100rpm (69%Nc) speed condition, for which the primary frequency component corresponds to 3/rev. All cases show a net increase in magnitude through the machine, although attenuation occurs for some traces through the first stage rotor, to be followed by amplification in the second stage rotor. No strong dependence on aerodynamic loading is seen.

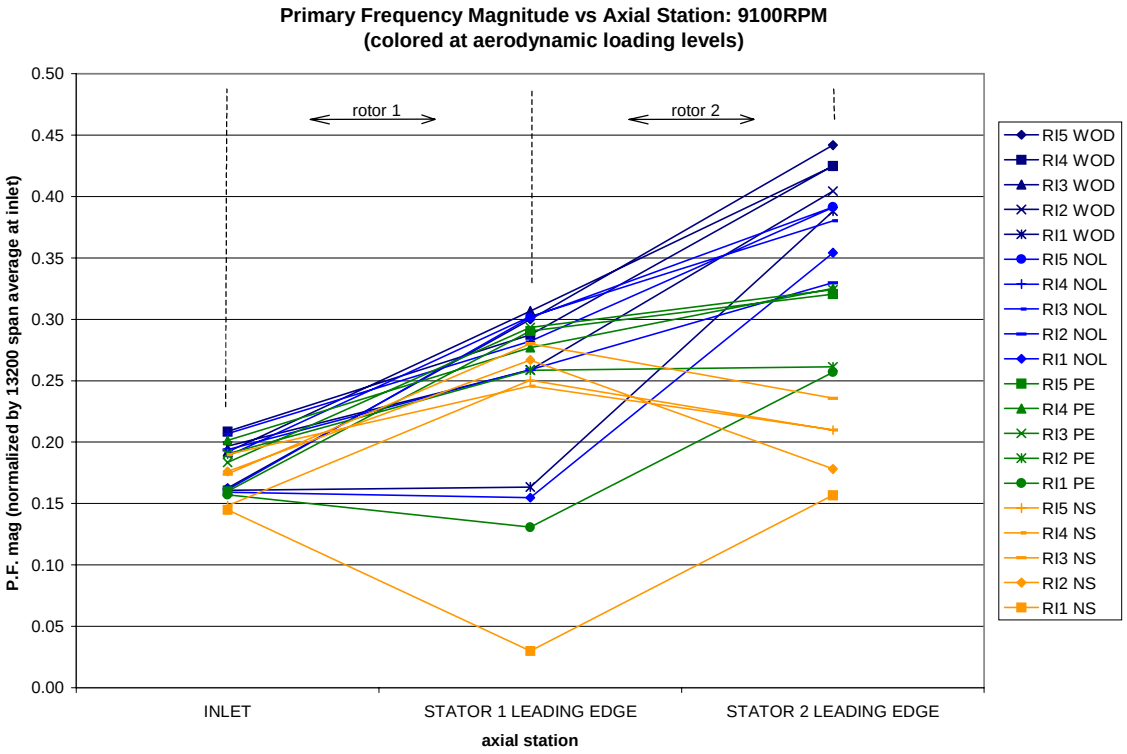

Figure 5.28: Primary Frequency Magnitude at Axial Measurement Stations, Color Indexed by Aerodynamic Loading Level, 9100rpm (69%Nc)

Data taken at 9500rpm (72%Nc) with primary distortion frequency of 8/rev are shown in figure 5.29. Note that inlet distortion amplitude is greater for this case than was observed previously. Additionally, rotor response at this speed and distortion engine order is strikingly different than that measured at 69%Nc. The majority of data show attenuation through both the first and second stage rotors, with the exception of four cases whose relative inlet distortion amplitude is low. No dependence on aerodynamic loading level is observed.

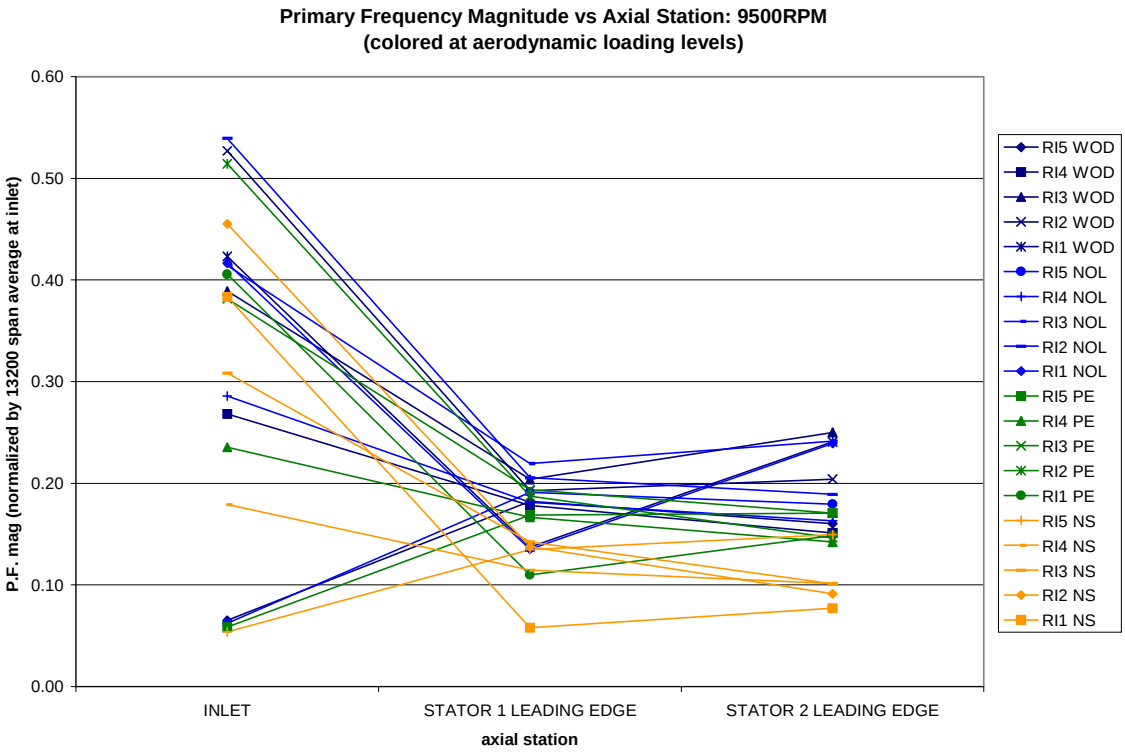

Figure 5.29: Primary Frequency Magnitude at Axial Measurement Stations, Color Indexed by Aerodynamic Loading Level, 9500rpm (72%Nc)

Figure 5.30 presents data taken at 13200rpm (99%Nc), also with an 8/rev distortion. Attenuation is again seen through rotor 1, although unlike the previous case, this is followed by amplification though the second stage. Inlet primary frequency magnitudes are higher than in the preceding two cases, with the exception of three cases whose inlet value and behavior are similar to the 69%Nc case. Like the other cases examined, there is no apparent dependence on aerodynamic loading.

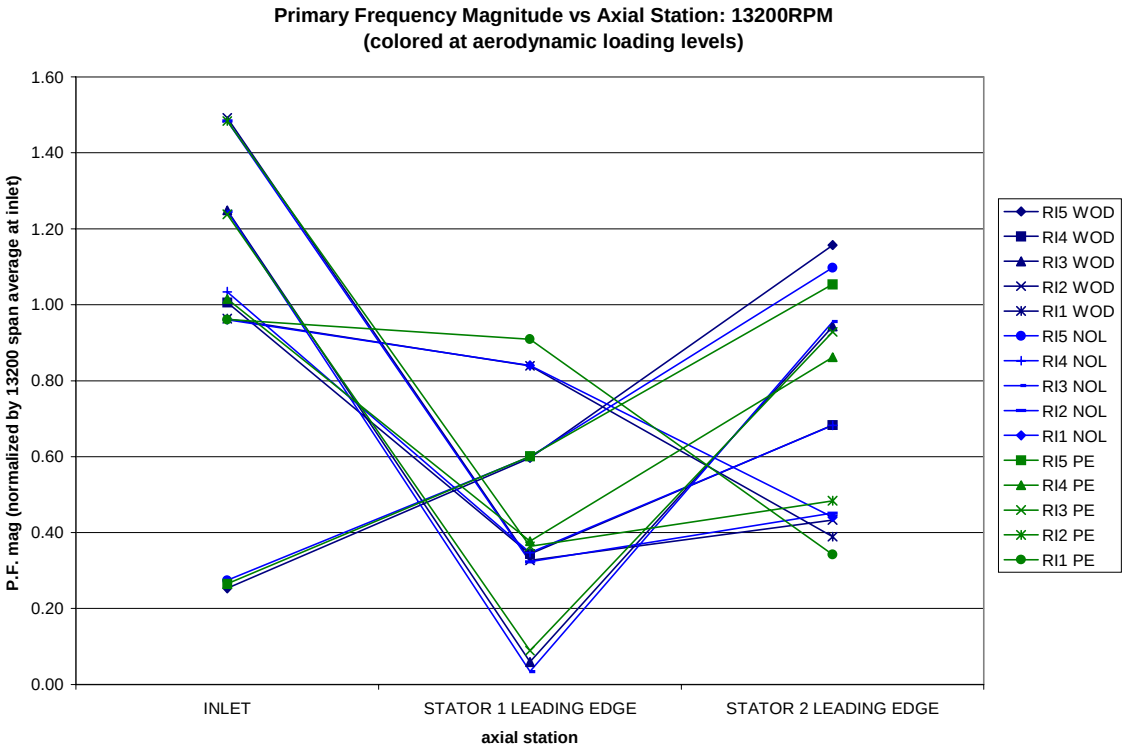

Figure 5.30: Primary Frequency Magnitude at Axial Measurement Stations, Color Indexed by Aerodynamic Loading Level, 13200rpm (99%Nc)

5.5 Primary Frequency Magnitude as a Function of Axial Position and Radial Position

While general trends of amplification and attenuation were found by examining data in the previous section, no strong dependence of distortion amplitude on aerodynamic loading was found. This section presents the same data. However it highlights data sets measured at the same radial positions through the machine, whereupon the importance of streamline radial position, regardless of aerodynamic loading, becomes evident. It is also shown that limited similarity exists between data taken at the same radial position while operating with different rotor speeds.

Figures 5.31, 5.32 and 5.33 are identical to figures 5.28, 5.29 and 5.30, respectively, except that the data's color is now indexed by radial position. Presented in

this fashion, it is readily apparent that primary frequency amplification is a strong function of radial position, especially at higher speeds.

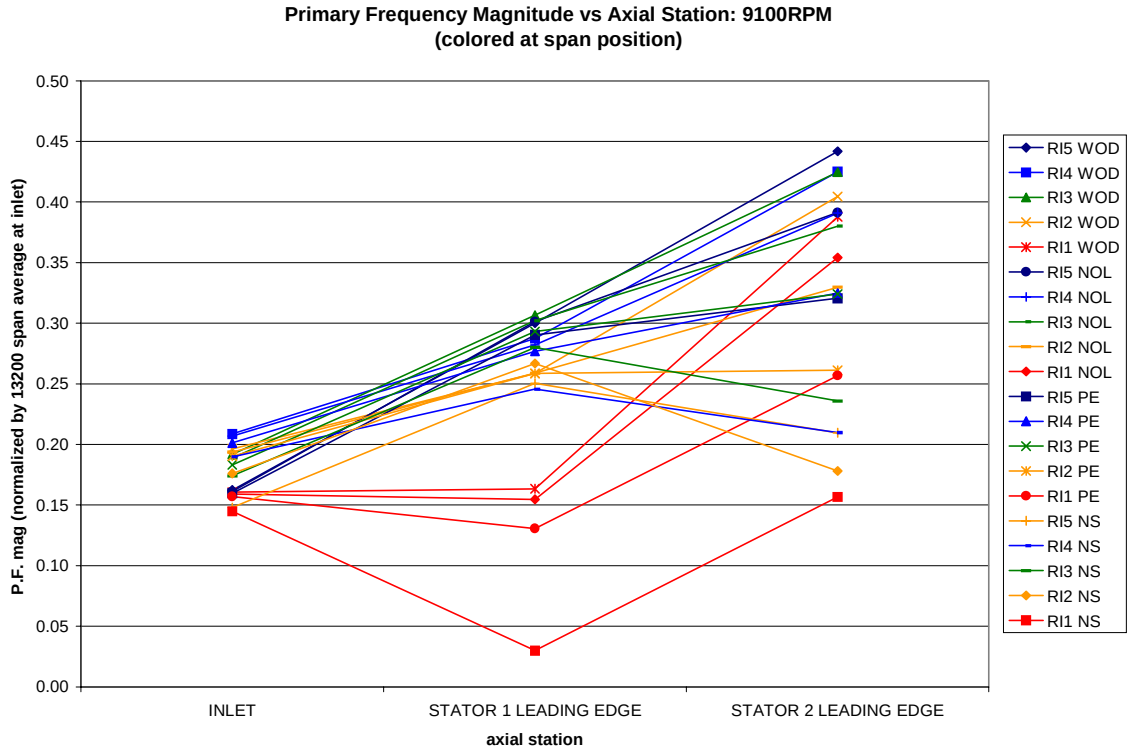

Figure 5.31: Primary Frequency Magnitude at Axial Measurement Stations, Color Indexed by Span Position, 9100rpm (69%Nc)

Distortion behavior at 9100rpm is fairly constant across the span, except for RI 1, where the distortion is not amplified through the first stage rotor. Large distortion amplitude "divergence" is seen through the machine as comparatively uniform distortion amplitudes at the inlet are amplified to various values between 15% and 45% of the normalization parameter.

In contrast to this is the behavior observed in figure 5.32 where a wide range of inlet distortion amplitudes converge to a much smaller range at the compressor exit.

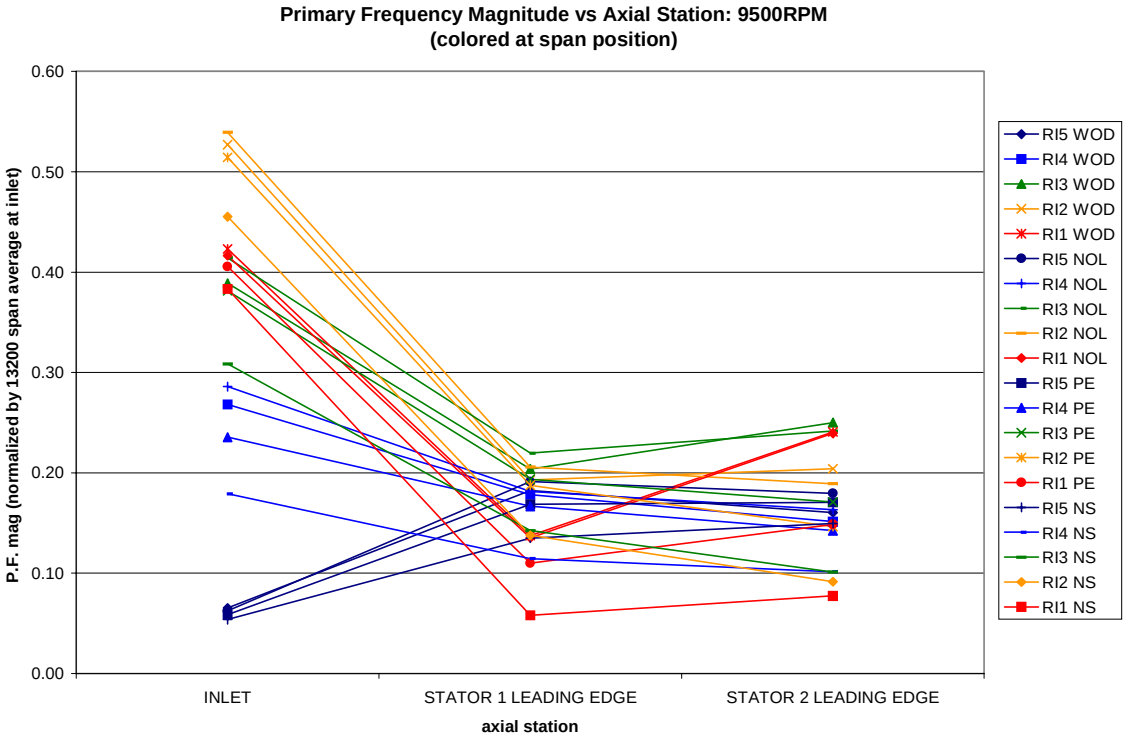

Figure 5.32: Primary Frequency Magnitude at Axial Measurement Stations, Color Indexed by Span Position, 9500rpm (72%Nc)

In all three cases, distortion amplitude behavior is rather strictly grouped by radial position. Recall that the data reduction technique is devised such that measurements taken axially at corresponding radial positions represent, using a Lagrangian flow description, the behavior of a given quantity of fluid mass through the machine. Thus, each individual trace in figures 5.31, 5.32 and 5.33 can be viewed as the result of following a group of fluid particles through the test compressor whose centers are positioned at RI's given in table 4.4. The resulting action of the compressor on a fluid mass is therefore highly dependent on the span location at which the fluid enters the compressor. This dependence increases with rotor speed, until the condition shown in figure 5.33 is achieved; measured total pressure amplitudes are vastly different across the flow annulus throughout showing no discernable amplification or attenuation trends. This behavior is a manifestation of spanwise non-linear behavior occurring at design speed due to such phenomena as blade passage boundary shock system development.

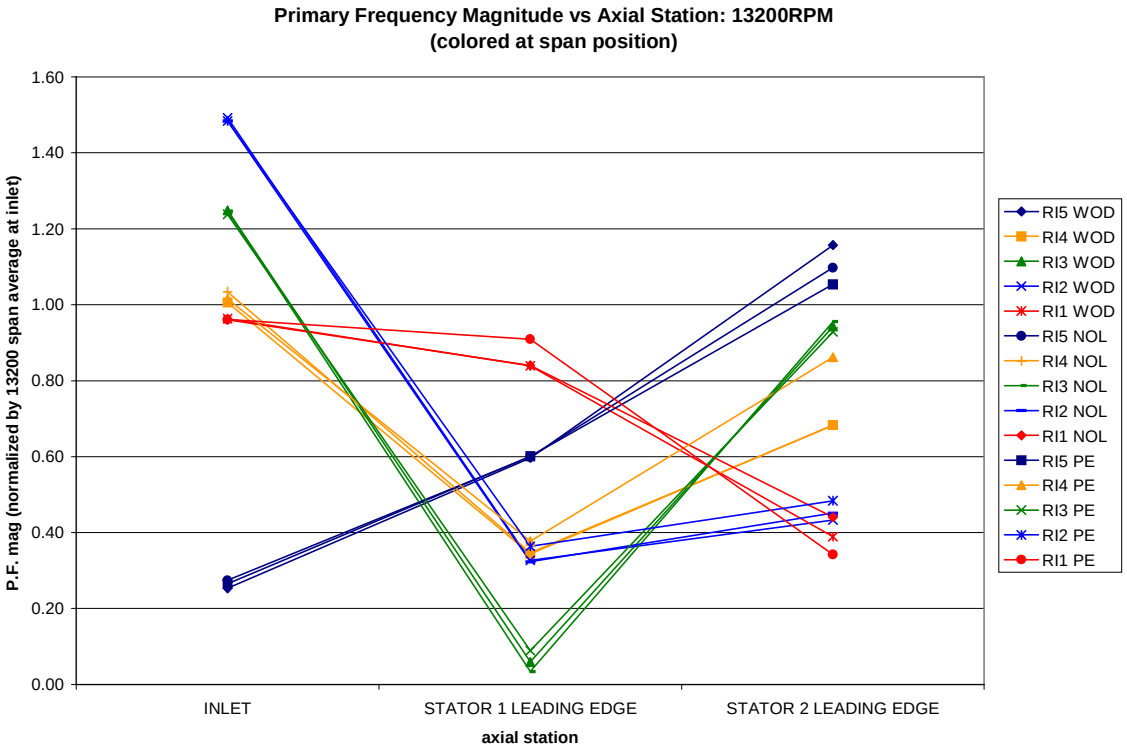

Figure 5.33: Primary Frequency Magnitude at Axial Measurement Stations, Color Indexed by Span Position, 13200rpm (99%Nc)

A possible method of dealing with this spanwise- dependent behavior is to treat the compressor as being composed of five pseudo- compressors, corresponding to the five concentric, equal mass flow annuli under investigation. If distortion attenuation were a linear function of rotor speed then it would be expected that flow amplitudes measured through the machine at similar radial positions would behave similarly. If distortion attenuation were a linear function of distortion frequency (per rev) then some similarity would be expected between at least the two 8/rev data sets. In fact, as illustrated in figure 5.34, limited similarity is seen at the five radial positions for the three data sets considered in this study. Near the hub, at RI5, amplitude behavior at the three conditions do parallel each other, although for the remaining four locations substantial differences are seen. Behavior at RI3 is especially sinuous where both rotors are observed amplifying the distortion in some instances while attenuating it in others. This is a compelling indication that total pressure distortion amplitude is not a strong function of radial position alone, and that there are prevalent non-linear interactions occurring.

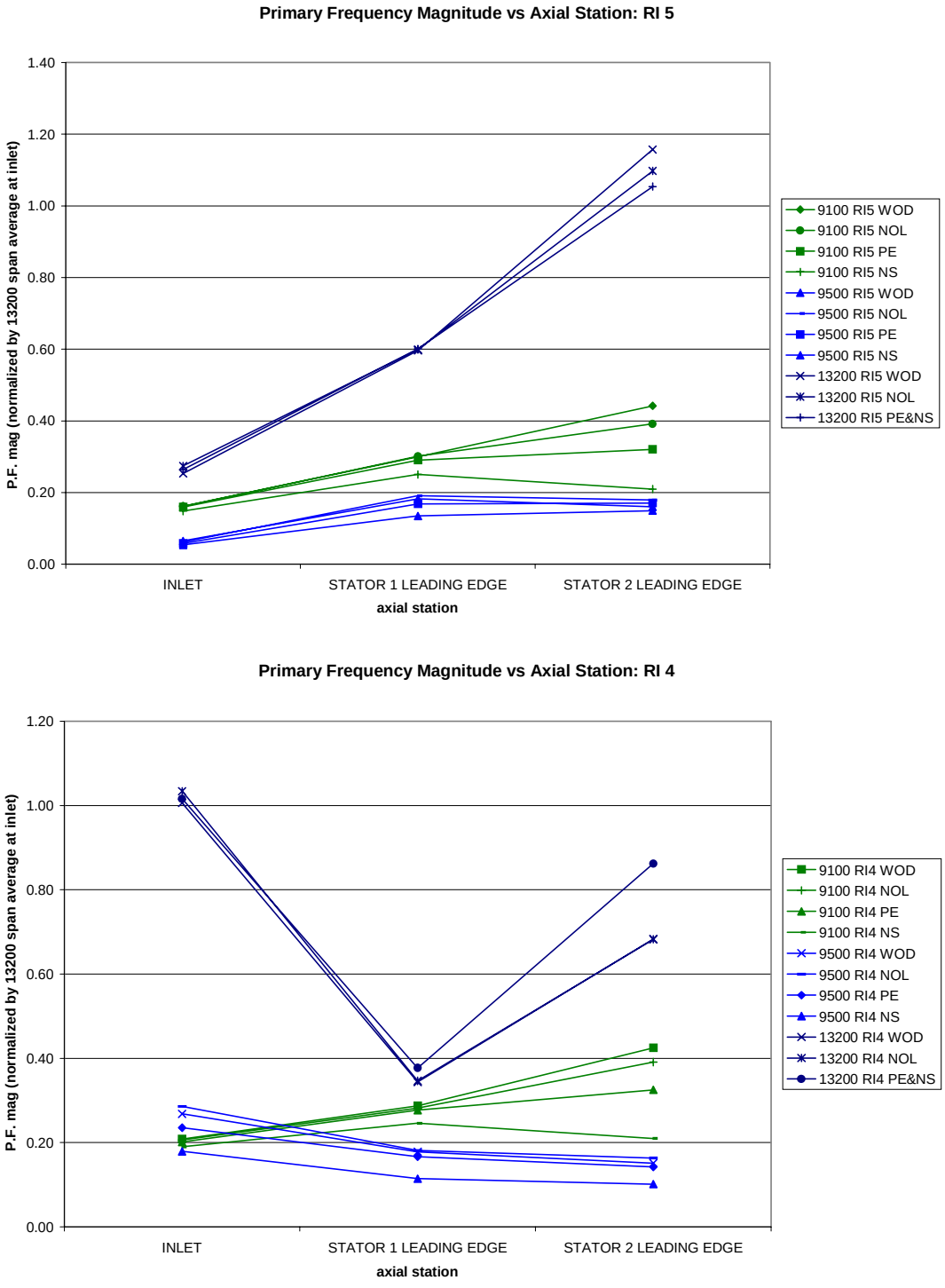

Figure 5.34: Dependence of Primary Frequency Amplitude on Radial Position

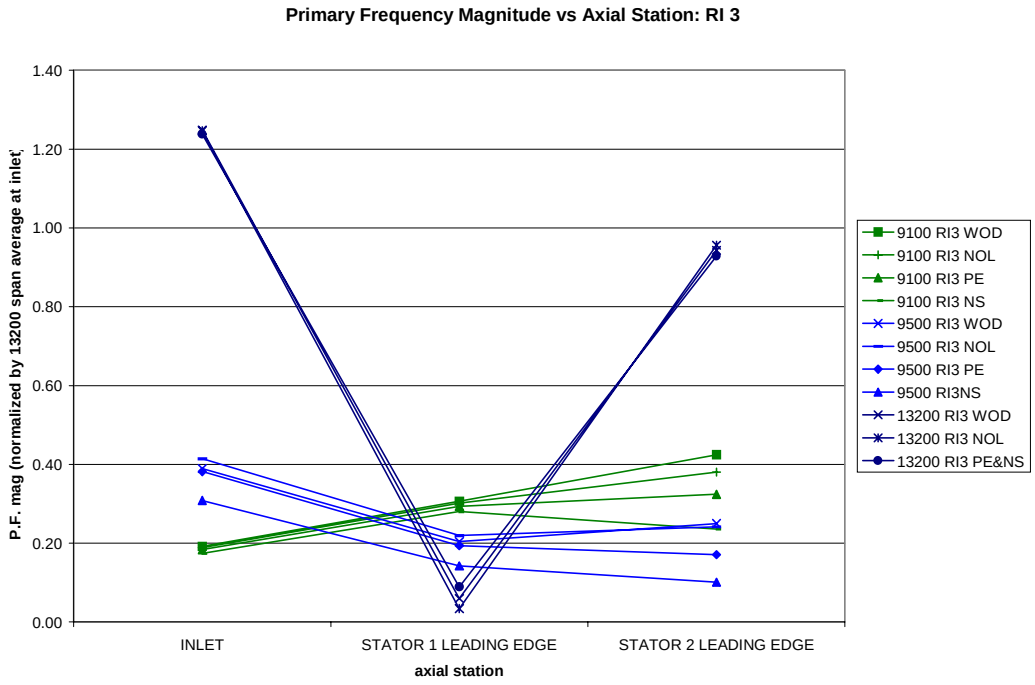

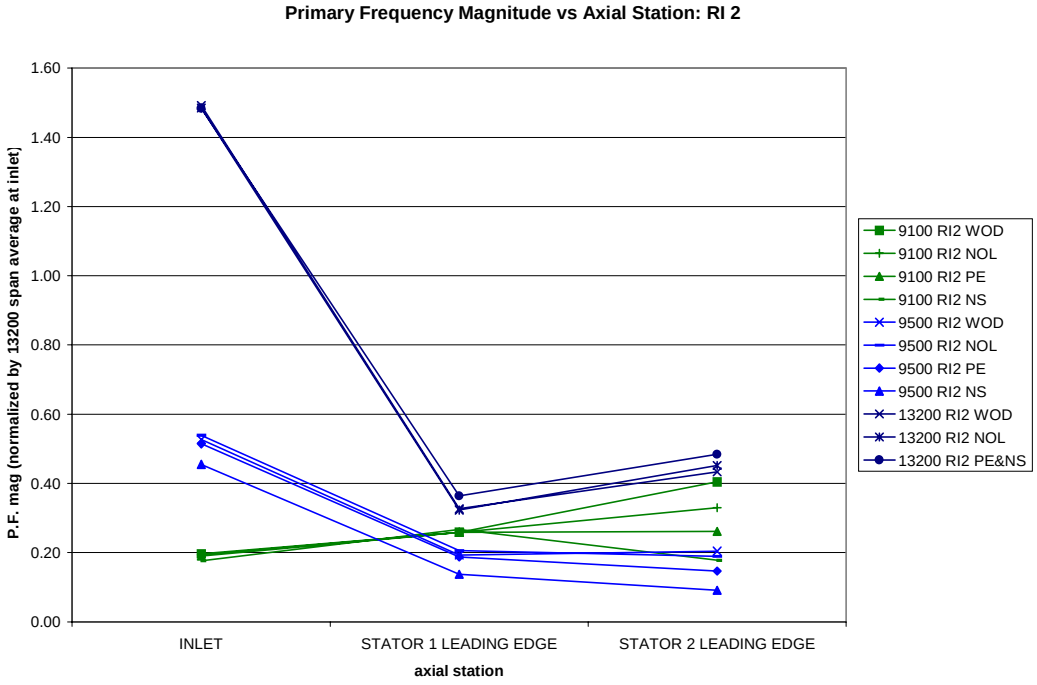

Figure 5.34, cont.: Dependence of Primary Frequency Amplitude on Radial Position

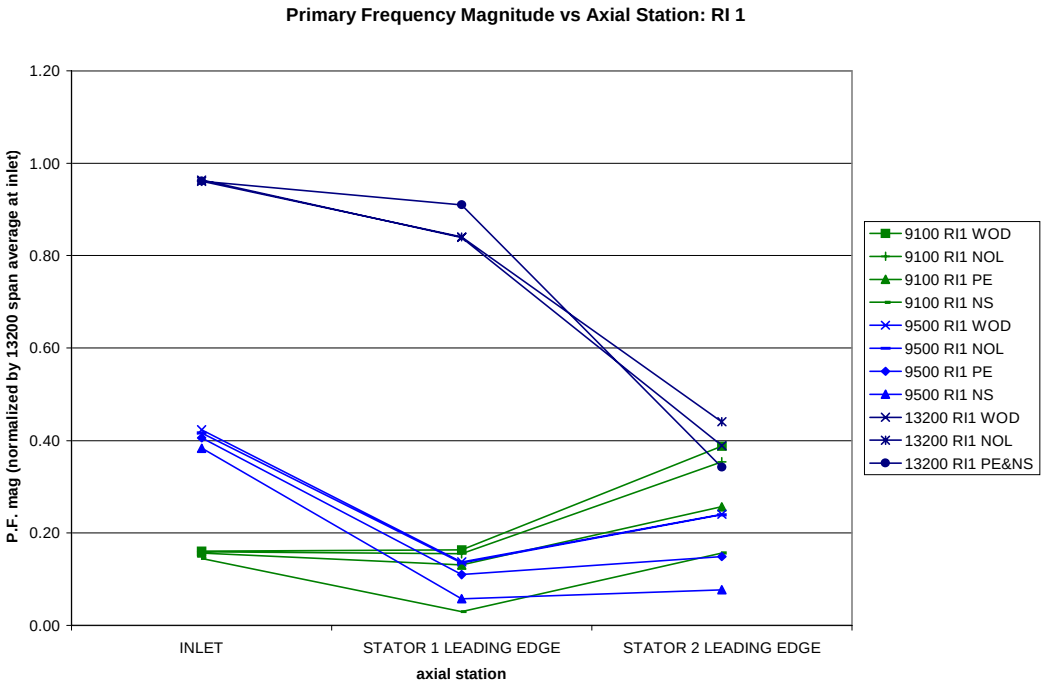

Figure 5.34, cont.: Dependence of Primary Frequency Amplitude on Radial Position

This section presented data measured along three different speed lines of the test compressor in both the frequency and time domains. Component frequency magnitudes were found to decay quickly between the twentieth and thirtieth component frequencies; thereby the sampling rate, which permits calculation of 180 frequencies, is sufficiently high.

Investigation of distortion amplitudes at axial positions through the compressor, by means of primary component frequency amplitudes, show that for each individual flow condition, there is strong dependence on radial position. However, dependence at a given location is a markedly different functional for every flow condition, indicating that other factors besides radial position strongly affect flow behavior. These factors are examined in the next chapter.

6 Fundamental Frequency Response Function Compressor Flow Modeling: Method and Results

Compressor flow properties acquired as described in chapter 4, and the corresponding frequency domain transformations and FRF's described in chapter 3, form the basis of the modeling technique presented here. This section begins with a description of the technique, with application to the test compressor used in this study, including FRF's developed at several operating points and distortion intensities. The section concludes with predictions of rotor exit total pressure profiles using the developed models.

6.1 Fundamental Frequency Response Function Model

Simply stated, the fundamental FRF model is an FRF. Calculated from measured system input and output data, the FRF can be excited by input with "unknown" response, creating a prediction of the system's resulting output. This is illustrated in figure 6.1, which shows a measured FRF being excited by an input function. If the system is linear, then the FRF correctly reproduces system behavior for any given excitation. If the system is weakly non- linear, then the FRF would be expected to predict system behavior with reasonable accuracy only for operating points similar to those at which it was developed.

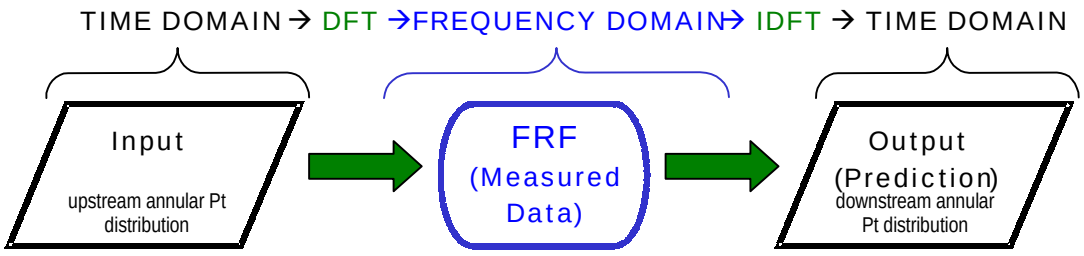

Figure 6.1: Fundamental FRF Compressor Modeling Procedure

More exactly, excitation of the FRF and calculation of the predicted response function occurs at each component frequency. Magnitude and phase values of the k^{th} component frequency are calculated separately, shown in equations 6.1 a and b. These are calculated for 180 component frequencies and the resulting response function is inverse transformed, as described in section four, to produce a prediction of the system's time domain output.

$$M_{RF,\,k} = M_{FRF,\,k} * M_{FF,\,k}$$

Equation 6.1a

$$\theta_{RF,\,k} = \theta_{FRF,\,k} - \theta_{FF,\,k}$$

Equation 6.1b

Calculation of frequency response functions occurs on five concentric, equal mass flow annuli through the compressor whose positions are determined from streamline curvature calculations previously outlined. See figure 4.17 for a plan form view of fifteen computed streamlines centered on annuli of equal mass flow. Figure 6.2 illustrates the streamline corresponding to the fourth radial immersion (RI) and the corresponding FRF computation locations. The radial position of each RI is a function of axial position and compressor operating point. Positions at the three axial stations for each operating condition examined in this study are given in table 4.4.

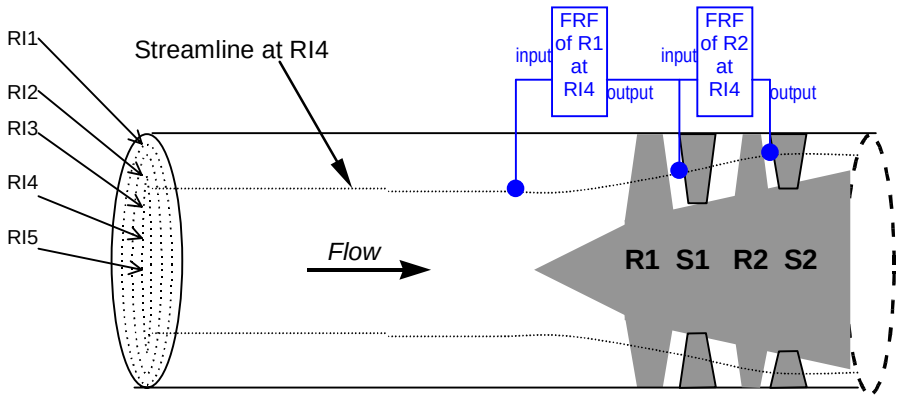

Figure 6.2: Centers of Five Equal Mass Flow Annuli Corresponding to Five Radial Immersions (RI) in CRF Test Compressor and Location of Data Collection for FRF Calculation (only RI 4 shown)

Input and output data for the FRF computed across rotor 1 are the annular total pressure profiles measured upstream of the rotor and at the first stage stator leading edge, respectively. Note that the streamline and the measurement and computation locations form bodies or revolution (not shown) about the machine centerline, thereby allowing the measurement and prediction of annular, spatially nonuniform distributions. In the rotor coordinate frame, these annular spatial distributions become functions of time, producing temporal data sets for use in FRF computation.

Lack of a measurement station directly upstream of the second rotor requires the use of first stage stator data as input to the second FRF and is the same data set used as the output of the first FRF. Data measured at the leading edge of the second stage stator act as output of the second FRF. Thus, the second FRF captures the effects of both the first stage stator and second stage rotor. However, since total pressure is the flow property used to generate the second FRF, it is principally the effect of the rotor that is captured. This is discussed further in section 5.2.

The requirement that the modeled system be linear reduces the ability of this fundamental FRF approach to model inherently non-linear fluid machinery. Nonetheless, FRF characteristics and prediction accuracy are investigated in the proceeding sections for several compressor operating points and distortion types. Results show that the compressor system is weakly non-linear at some span locations for deviations along the same rotor speed line; and strongly non-linear for the remaining cases.

6.2 Frequency Response Functions from 3/rev Distortion Case

Frequency response functions presented here are calculated using data measured upstream and downstream of the first stage rotor. Typical data sets used to calculate FRF's are presented in the time and frequency domains in section five.

Figure 6.3 presents an FRF calculated across rotor 1 at 9100rpm (69%Nc) for the outermost flow annulus. The first twenty- four component frequencies are included, as well as the DC (zeroth frequency) term. While this is not a representative FRF, due to typically strong spanwise dependence, it does illustrate several important points.

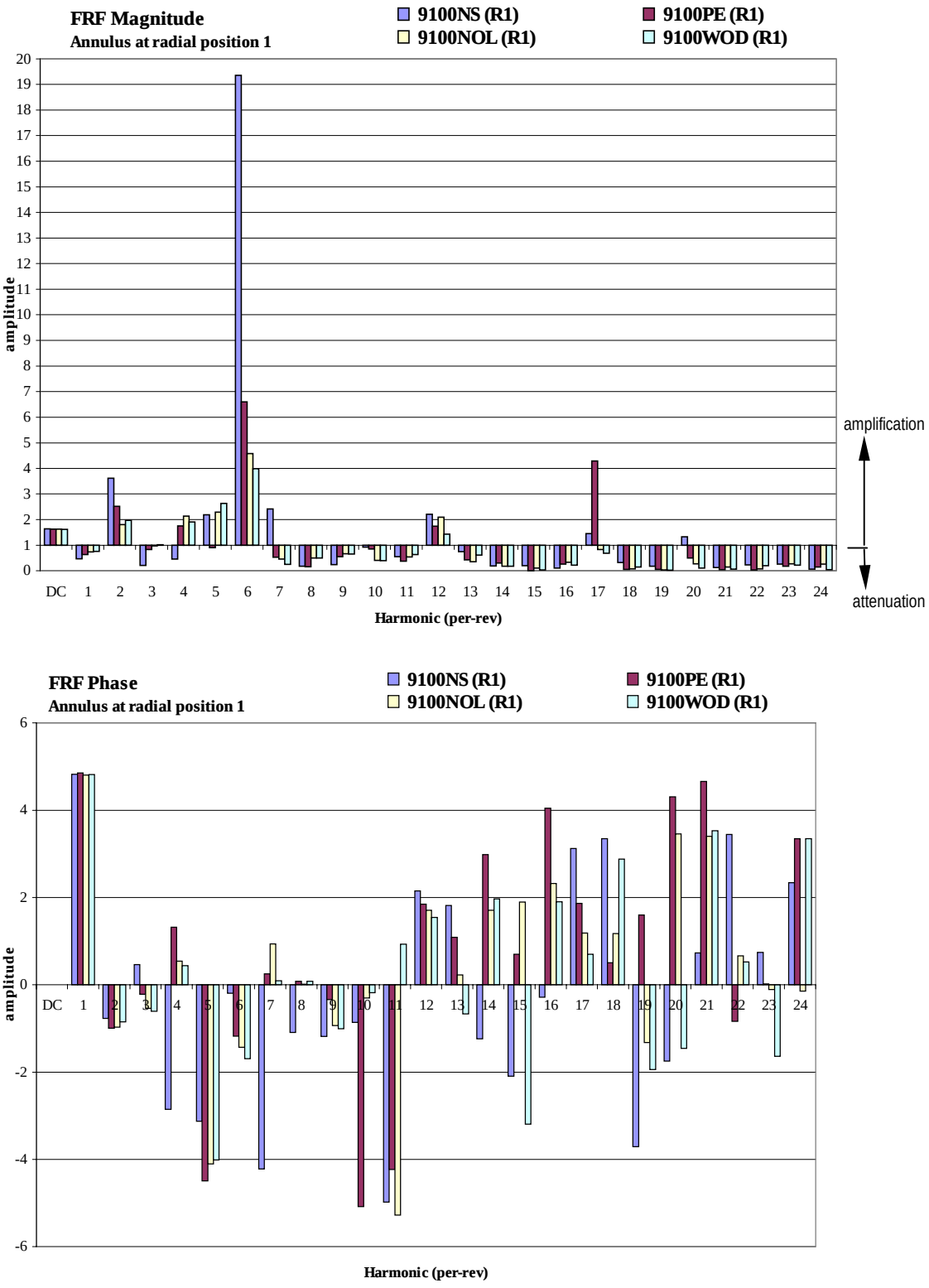

Figure 6.3: Magnitude and Phase of Rotor 1 FRF computed at 9100rpm, Radial Position 1

Since the FRF magnitude is the ratio of outlet to inlet magnitudes, values less than unity indicate attenuation. Likewise, FRF magnitude values greater than unity represent amplification. Examination of component frequency magnitude values, the top portion of figure 6.3, reveals that the majority are less than unity (downward pointing bars). Therefore, most frequencies are attenuated though the rotor, including the primary frequency at 3/rev. This is consistent with figures 5.28 and 5.31. However, the first (6/rev) and third (12/rev) harmonics are amplified, which could be of concern if a downstream rotor had vibrational modes at these frequencies. Frequency response function magnitude values do not appear to be highly dependent on aerodynamic loading.

Returning to the electronic filter/ compressor analogy presented in chapter 3, recall that the FRF's DC term is equivalent to the pressure ratio of the compressor components between which the FRF is calculated. Consequently, the total pressure ratio of the first stage rotor at all four throttle settings investigated is approximately 1.5.

Interpretation of phase data is less clear due to the small relative amplitude of most frequency components. Primary frequency phase shift at the NOL condition is small, consistent with that seen between figures 5.3 and 5.8.

The FRF computed using data taken across the second stage rotor, figure 6.4, shows less consistency. Frequency components are variously amplified or attenuated, with some dependence on aerodynamic loading. Consistent with figures 5.28 and 5.31, the primary frequency shows strong amplification across the rotor, with ratios as high as five at the NS condition. However, the first and third harmonics are attenuated. High spikes at the 15/rev and 24/rev are likely spurious and caused by low- amplitude signals. The DC component has a value of approximately 1.5 and when combined with the value observed at the previous stage (1.5) produces the overall machine pressure ratio of 2.3.

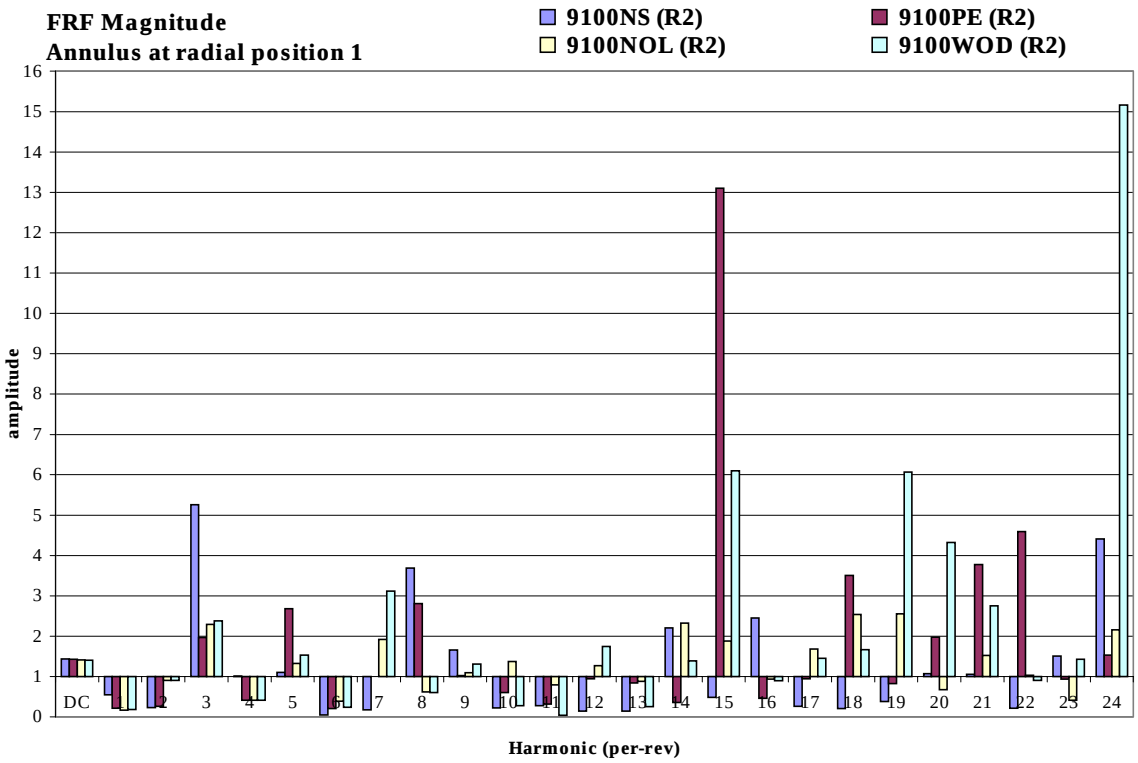

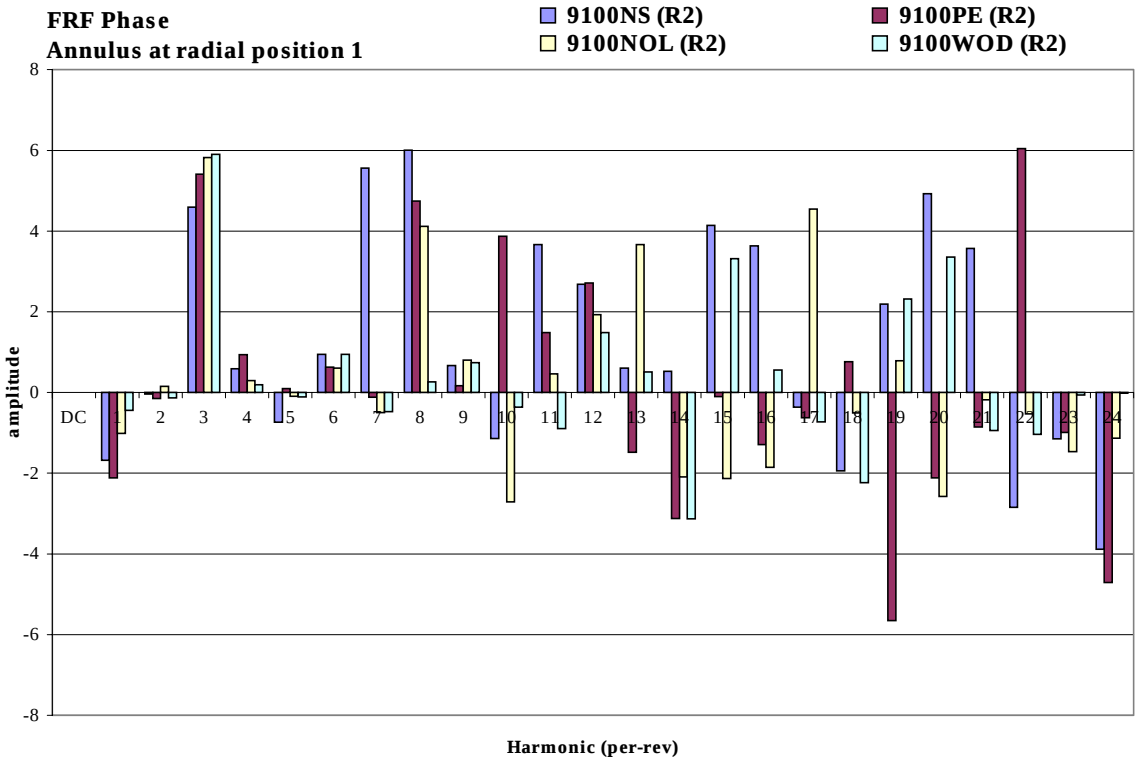

Figure 6.4: Magnitude and Phase of Rotor 2 FRF computed at 9100rpm, Radial Position 1

6.3 Frequency Response Functions from 8/rev Distortion Case

An FRF calculated from data measured at RI3, a mid- span location, at 13200rpm (99%Nc) for the first stage rotor is presented in figure 6.5. The DC term shows a pressure ratio of nearly 2.5, much higher than the previous case. Primary frequency values are low, indicating significant attenuation by rotor 1, also observed in figure 5.33. The second and third harmonics show amplification at most throttle settings. Other frequency components are either attenuated or weakly amplified, with the exception of the component at 1/rev, which is strongly amplified by a factor of nearly ten. However, the corresponding frequency magnitude at the inlet, shown in figure 5.20, is low; although amplified ten times it is of the same order as other first component frequencies at the outlet, figure 5.23.

The seemingly significant amplification of the 1/rev component, found only to amplify a modest input signal, illuminates an important topic regarding interpretation of FRF results. One must consider amplitude ratios in the context of the frequency component being amplified. Strong amplification or attenuation, although appearing influential in the FRF may be acting on an insignificant input magnitude. This is the basis of one element used to create a method to adjust FRF components and is examined in the next chapter.

The second stage rotor's FRF, figure 6.6, shows attenuation at most component frequencies, except the primary, which is amplified eight to twenty- three times, depending on aerodynamic loading. This strong amplification through the second rotor is also illustrated in figure 5.33.

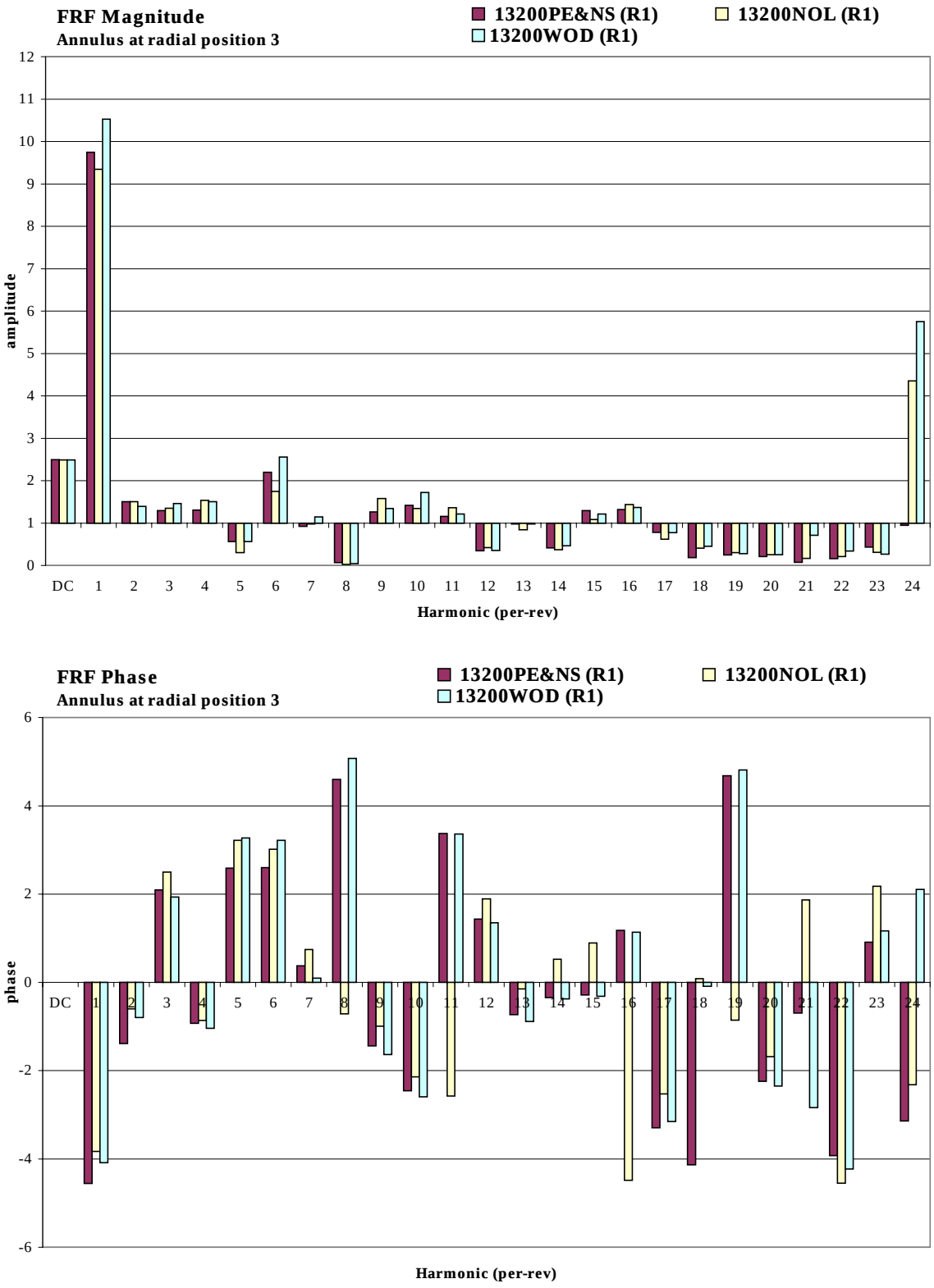

Figure 6.5: Magnitude and Phase of Rotor 1 FRF computed at 13200rpm, Radial Position 3

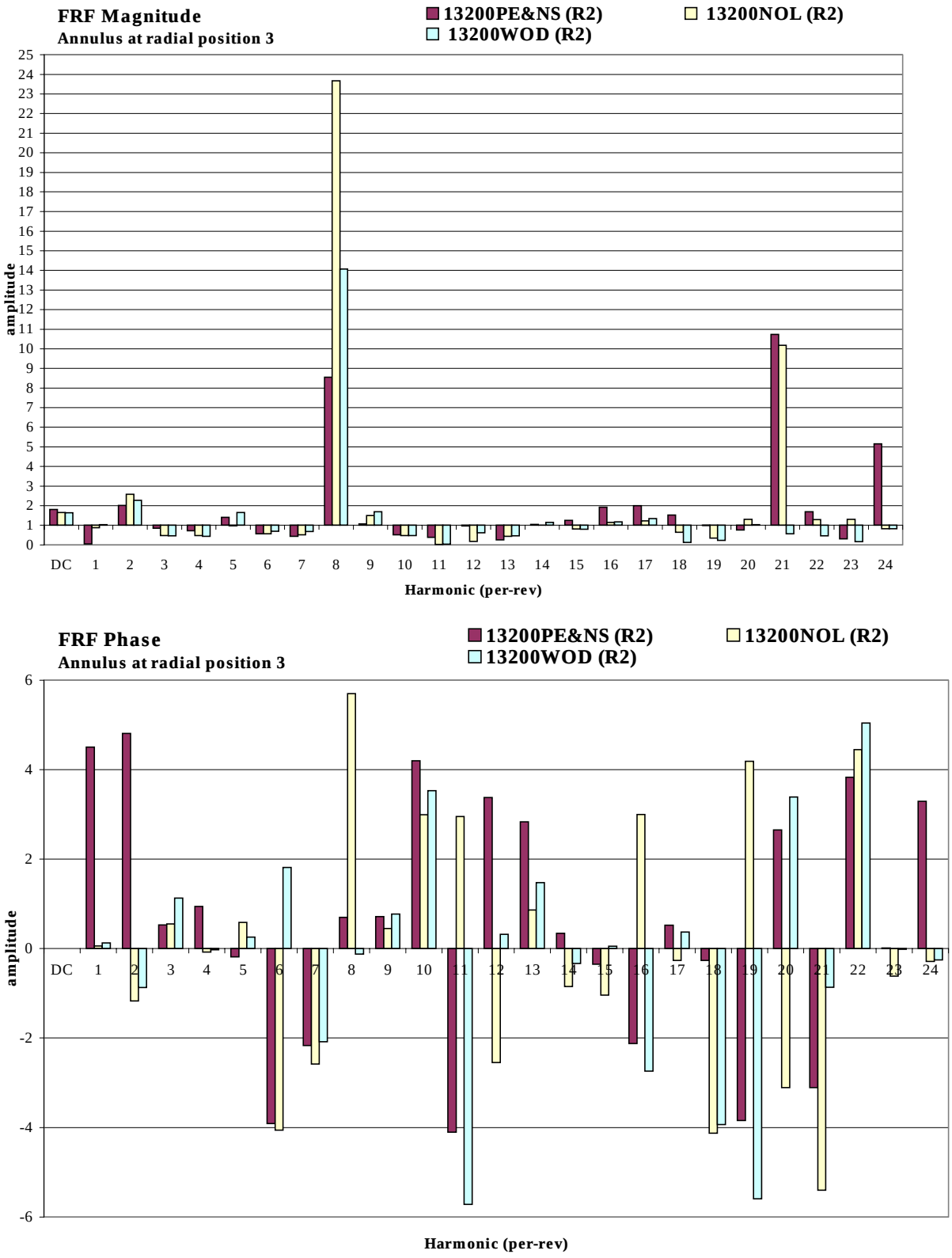

Figure 6.6: Magnitude and Phase of Rotor 2 FRF computed at 13200rpm, Radial Position 3

6.4 Accuracy of Frequency Response Function Predictions at the Operating Point at which they were Derived

The ability of any model to predict the data from which it was derived is a measure of the upper limit of the model's prediction accuracy. Predictions presented in this section are used to investigate the capability of FRF models and represent the highest accuracy achievable with this method using the available data resolution.

Data measured at 9100rpm (69%Nc) NOL is used to calculate an FRF at five span locations across the first stage rotor. The FRF at the outermost flow annulus for this case is presented in figure 6.3. Each FRF is then excited by the upstream annular total pressure distribution from which it was calculated. The resulting downstream predictions at five span locations, made using 180 frequency components, are presented in the time domain in figure 6.7. Prediction accuracy is very high; measured (blue) and predicted (green) traces are coincident. This behavior is representative of all data measured in this study.

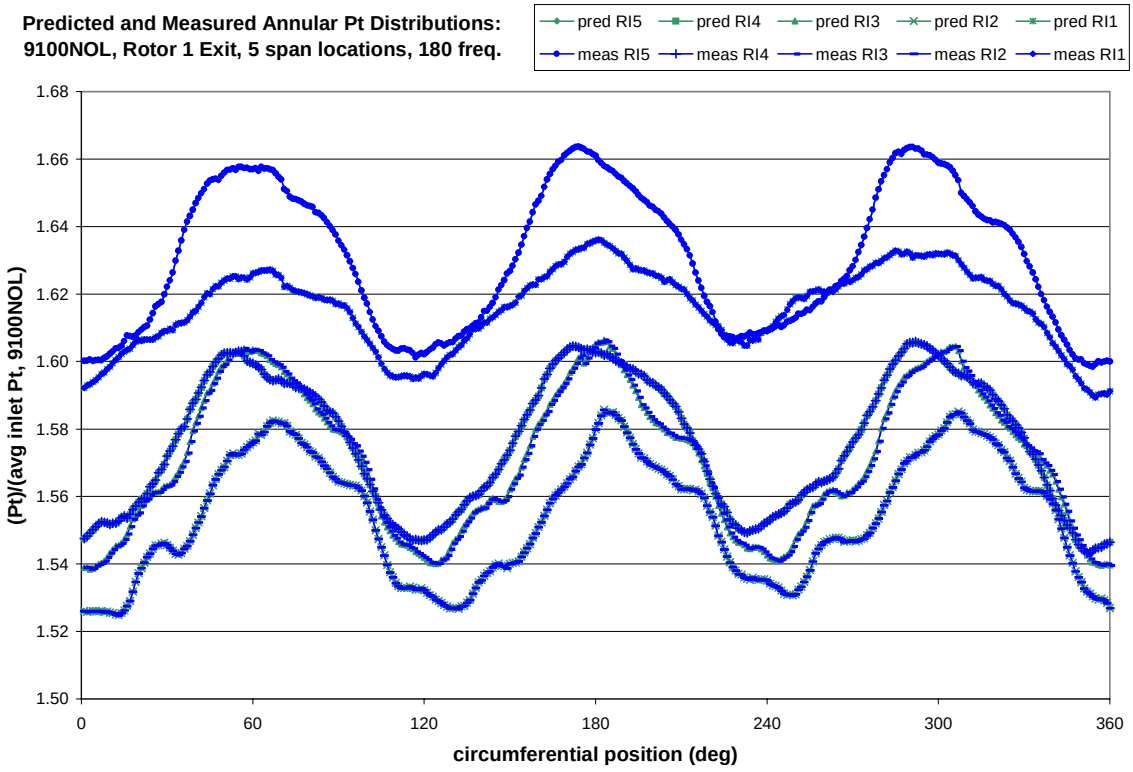

Figure 6.7: Predicted and Measured Annular Pt Distributions 180 Frequency Components, 5 Span Locations, R1 Exit, 9100NOL

As a means of lessening the complexity of the FRF model, removal of high frequency components was investigated. It was found that sufficient prediction accuracy is maintained by reducing the required number of terms from 180 to 25 (24 frequency components + DC term). This number is chosen because it falls in the range of components (20^{th} to 30^{th}) where the amplitudes at both the input and output have significantly decayed. Additionally, as discussed in chapter 5, distortion harmonics also decay by the 24^{th} frequency. The method used in this study to remove frequency components is to set their magnitude to zero.

This undertaking of reducing the frequency content of the FRF illuminates another important point. The required number of components of a given FRF can be adjusted to match the known disturbance content (from Fourier analysis) of the flow and known HCF excitation frequencies. Since the ability of the FRF method to capture high engine order disturbances is limited only by circumferential data resolution, had the data examined here contained distortion of high enough order, this study would have examined disturbances to 180/rev.

The prediction previously presented in figure 6.7 is repeated in figure 6.8, using the reduced frequency content FRF. Data point markers have been removed to allow close examination of results. The predicted total pressure distribution is of high accuracy, although since it includes only the first 24 component frequencies, it does not capture very high frequency “wiggle” seen in the measured data.

Table 6.1 gives a quantitative comparison of prediction accuracy between the 9100rpm prediction made with 180 component frequencies and that made with 24. Presented for five total pressure profiles is the difference between average variation from their mean, as a percentage of average inlet total pressure, for predicted and measured data. Larger percentages indicate poorer prediction accuracy.

Predictions made with 180 FRF component frequencies show no difference between measured and predicted average deviation, indicating they are accurate to within measurement resolution. Those made with 24 component frequencies show similar accuracy at two span locations, and very slight inaccuracy at the remaining three.

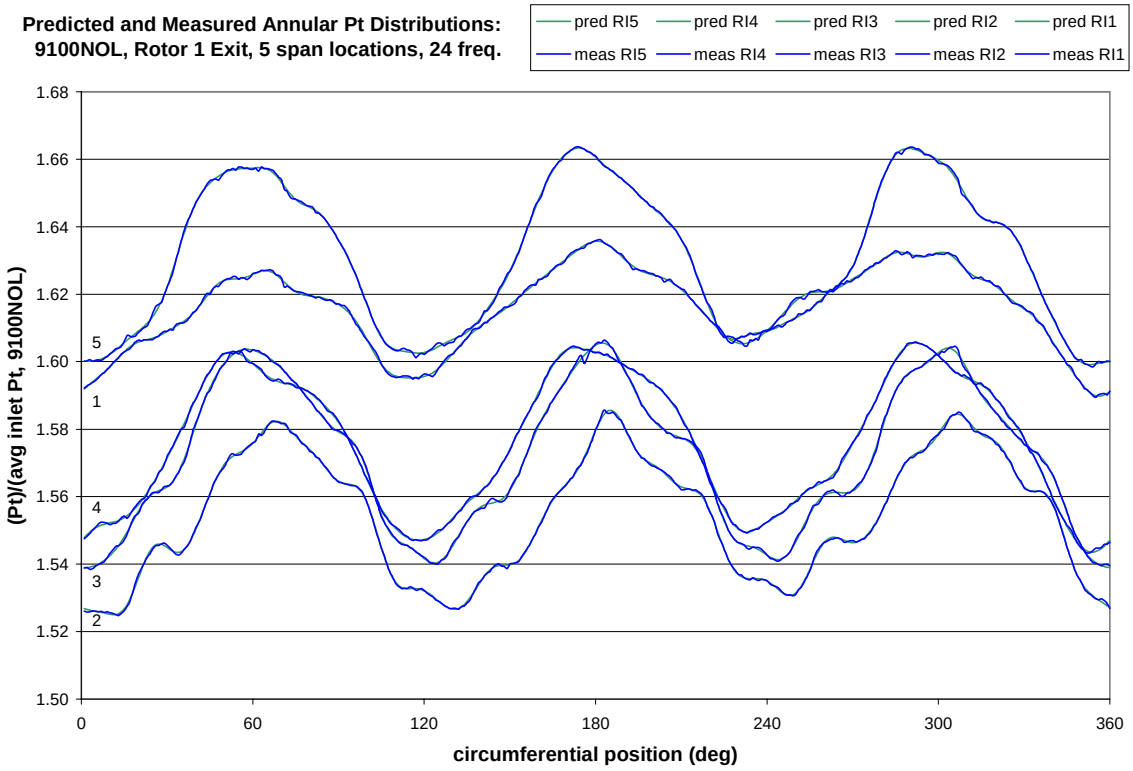

Figure 6.8: Predicted and Measured Annular Pt Distributions 24 Frequency Components, 5 Span Locations, R1 Exit, 9100NOL

Dependence of Prediction Accuracy on Number of Component Frequencies: Rotor 1					
	RI1	RI2	RI3	RI4	RI5
180 freq.	0.000%	0.000%	0.000%	0.000%	0.000%
24 freq.	0.000%	0.001%	0.001%	0.000%	0.001%

Table 6.1: Normalized Percentage Difference Between Measured and Predicted Average Variation from Mean, of Predictions Made with 180 and 24 Component Frequencies, Rotor 1

A presentation method used throughout the remainder of this report is introduced in figure 6.9. Shown for the first 24 component frequencies and the DC term at the five investigated span locations are the ratios of measured frequency component values (magnitude or phase) to predicted frequency component values. Magnitude (blue) values of unity indicate an exact prediction of a given frequency component. Phase (green) values have been offset (for display purposes) so that an exact prediction is shown by a

value of negative one. To avoid double- angle ambiguity, the presented phase accuracy is actually the ratio of the cosines of measured to predicted angles.

Accuracy values presented figure 6.9 are trivial, since predicted and actual FRF's are the same for this case, but this case is used as a datum for comparing future predictions. Note that the primary frequency and harmonics have been highlighted.

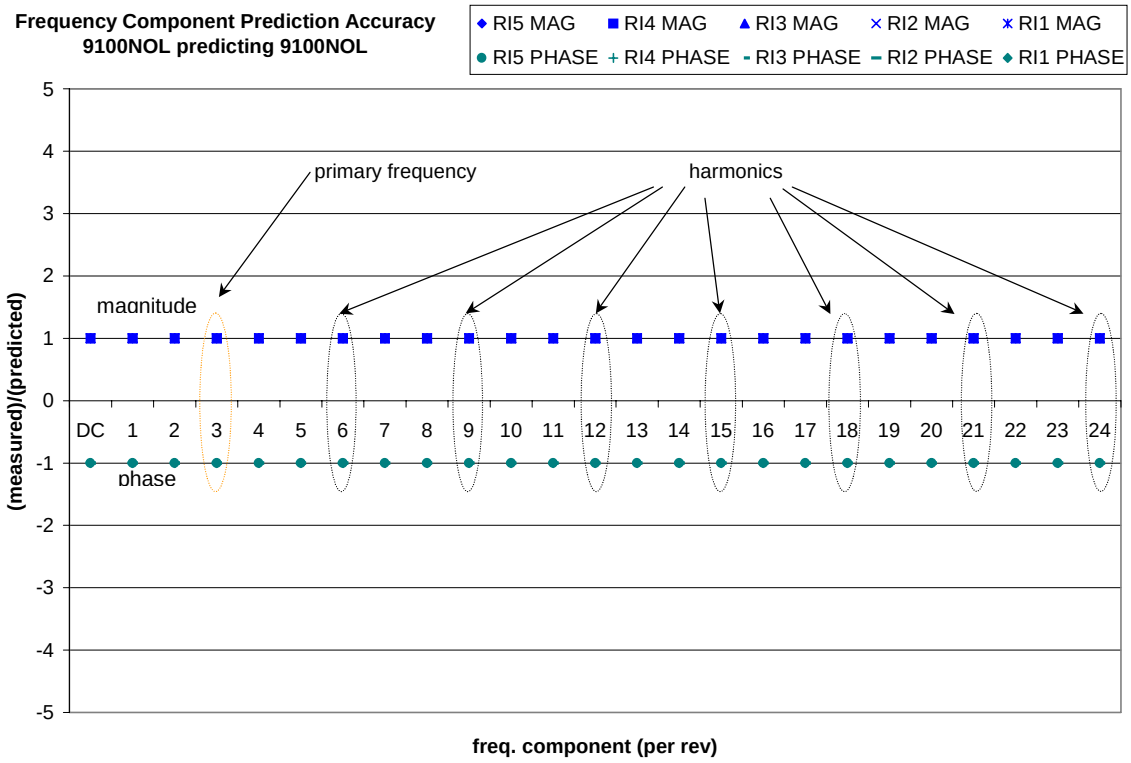

Figure 6.9: Frequency Component Prediction Accuracy, 9100NOL predicting 9100NOL

Frequency response functions calculated across rotor 2 and their associated predictions exhibit similar behavior. Prediction results of the corresponding 9100NOL case previously examined using 24 component frequencies is shown in figure 6.10. Again, the traces are nearly coincident, except for very high frequency "buzz". Accuracy is high, indicating that the FRF modeling technique has the potential to produce accurate and high fidelity results. These results are summarized in table 6.2, which shows that the same prediction accuracy as achieved for rotor 1 can be achieved for rotor 2.

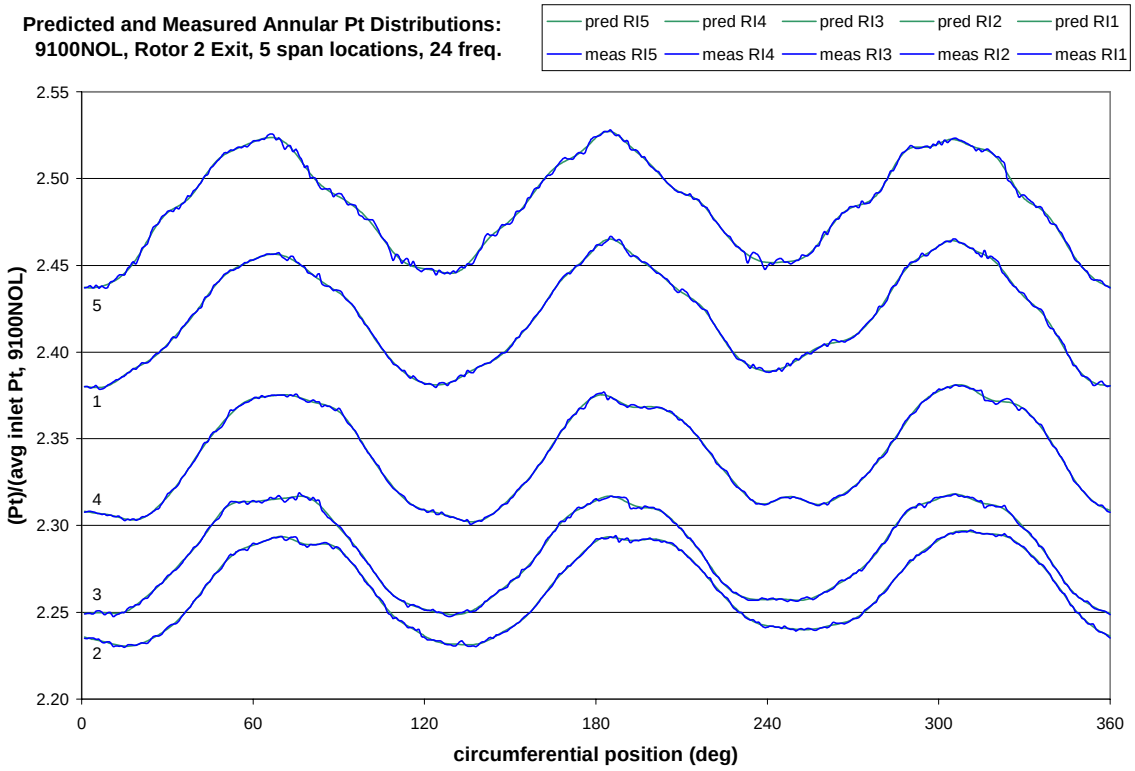

Figure 6.10: Predicted and Measured Annular Pt Distributions 24 Frequency Components, 5 Span Locations, R2 Exit, 9100NOL

Dependence of Prediction Accuracy on Number of Component Frequencies: Rotor 2					
	RI1	RI2	RI3	RI4	RI5
180 freq.	0.000%	0.000%	0.000%	0.000%	0.000%
24 frq.	0.003%	0.000%	0.001%	0.000%	0.004%

Table 6.2: Normalized Percentage Difference Between Measured and Predicted Average Variation from Mean, of Predictions Made with 180 and 24 Component Frequencies, Rotor 2

Prediction accuracy for both rotors at the remaining speeds, aerodynamic loading and distortion configurations examined is similar.

With baseline prediction accuracy established, the remainder of this chapter examines the ability of the FRF modeling technique to predict annular total pressure distributions at operating conditions other than those at which it was derived. All remaining FRF predictions are made using 24 component frequencies.

6.5 Fundamental Frequency Response Function Model Applied to "Near" Points

This section presents the use of the fundamental FRF modeling technique, described in section 6.1, to predictions of operating conditions similar to those at which the FRF was calculated. Data points measured along the same speed line are considered of adequate similarity and are "near" to each other with respect to blade row flow behavior.

The first set of predictions examined occur along the 9100rpm (69%Nc) speed line, with 3/rev upstream distortion. These use the same FRF model (calculated at 9100NOL) examined in the previous section. Presented in figure 6.11 are the time domain predictions of rotor 1 exit total pressure annular distributions at the five examined span locations for the WOD throttle setting. Prediction accuracy is high, although more greater differences are seen between measured and predicted data in this plot than in those examined previously. The peaks of some distributions are missed, as well as some subtle shaping.

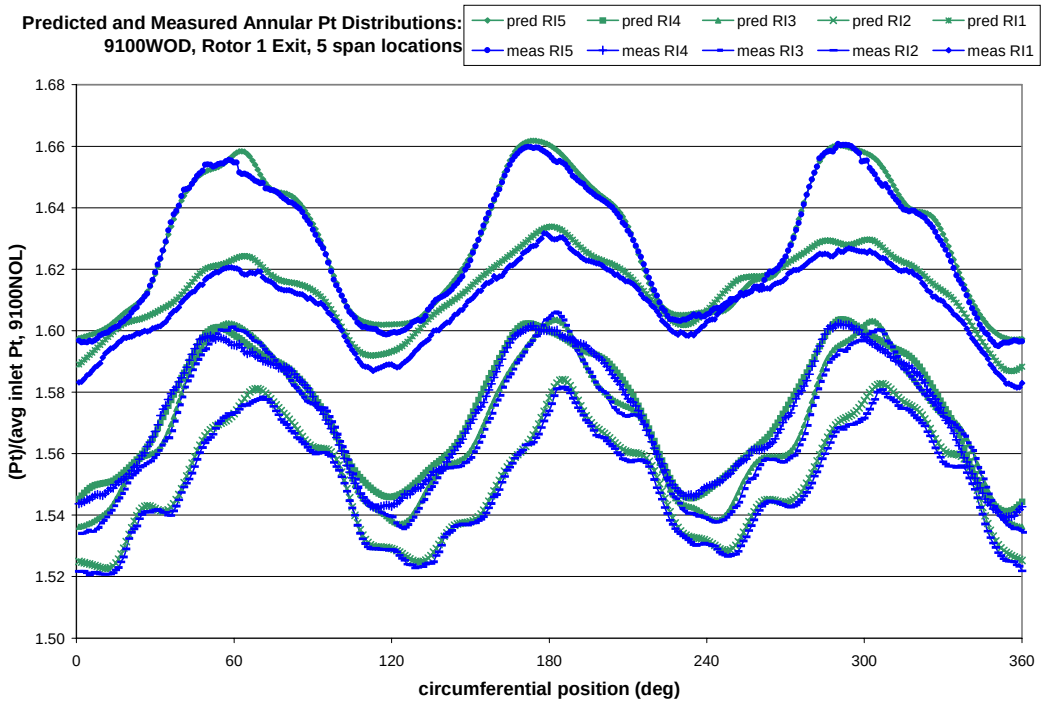

Figure 6.11 Predicted and Measured Annular Pt Distributions 24 Frequency Components, 5 Span Locations, R1 Exit, 9100WOD predicted with 9100NOL FRF

Frequency domain value predictions (where the prediction calculation actually occurs), figure 6.12, show considerable scatter, compared to figure 6.9, despite the relative accuracy of the corresponding time domain prediction. The primary frequency and some harmonics, especially the third, are predicted well. The DC term is also accurately predicted, indicating that the pressure ratio through the rotor is fairly constant over the range of this speed line. Note that the height of the harmonic ovals correlates with prediction accuracy: taller ovals represent comparatively worse component predictions.

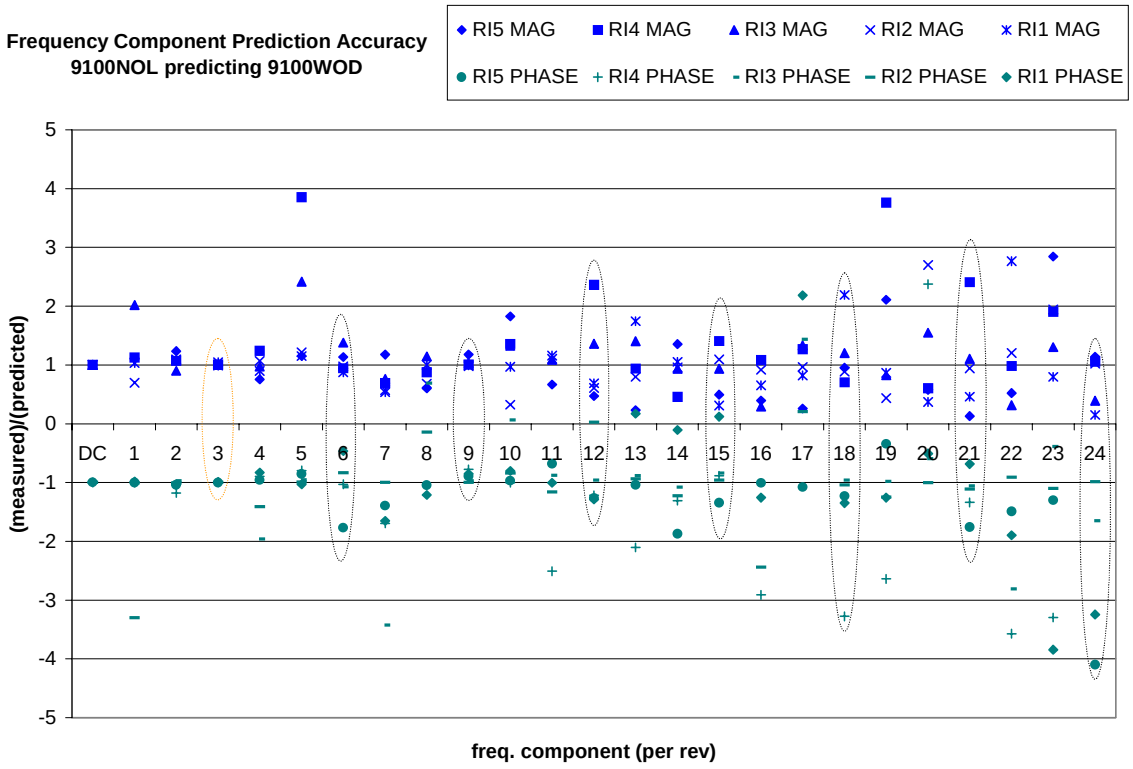

Figure 6.12: Frequency Component Prediction Accuracy, 9100NOL predicting 9100WOD

Prediction accuracy of the other two aerodynamic loading conditions is similar and results are summarized in table 6.3. Results of predicting the NOL condition, discussed in the previous section, are included for comparison. Accuracy is fairly consistent across throttle settings, with predictions at RI's 3 and 4 having the least variation from measured data. Equivalent data is presented for rotor 2 in table 6.4.

Prediction Accuarcy Along 9100rpm Speed Line Using 9100NOL Model: Rotor 1					
	RI1	RI2	RI3	RI4	RI5
NOL	0.000%	0.001%	0.001%	0.000%	0.001%
WOD	0.043%	0.030%	0.002%	0.016%	0.023%
NS	0.455%	0.199%	0.015%	0.075%	0.185%
PE	0.120%	0.029%	0.004%	0.009%	0.056%

Table 6.3: Normalized Percentage Difference Between Measured and Predicted Average Variation from Mean, of Predictions Along R1 9100 Speedline Made with R1 9100NOL model

Several important points are exposed. First, predictions along the 9100 speedline are less accurate for rotor 2 than they are for rotor 1. This indicates that aerodynamic loading has a stronger effect on flow properties in the second rotor. Although the values given in table 6.4 are larger than those in 6.3, they are still a small percentage of the normalization parameter (average inlet total pressure) and the resulting time domain predictions are still of reasonable accuracy. Figure 6.13 presents annular total pressure profile predictions at five span locations downstream of rotor 2 for the 9100WOD condition.

Prediction Accuarcy Along 9100rpm Speed Line Using 9100NOL Model: Rotor 2					
	RI1	RI2	RI3	RI4	RI5
NOL	0.003%	0.000%	0.001%	0.000%	0.004%
WOD	0.091%	0.471%	0.230%	0.161%	0.318%
NS	0.484%	1.020%	0.755%	0.827%	0.683%
PE	0.250%	0.436%	0.285%	0.356%	0.349%

Table 6.4: Normalized Percentage Difference Between Measured and Predicted Average Variation from Mean, of Predictions Along R2 9100 Speedline Made with R2 9100NOL model

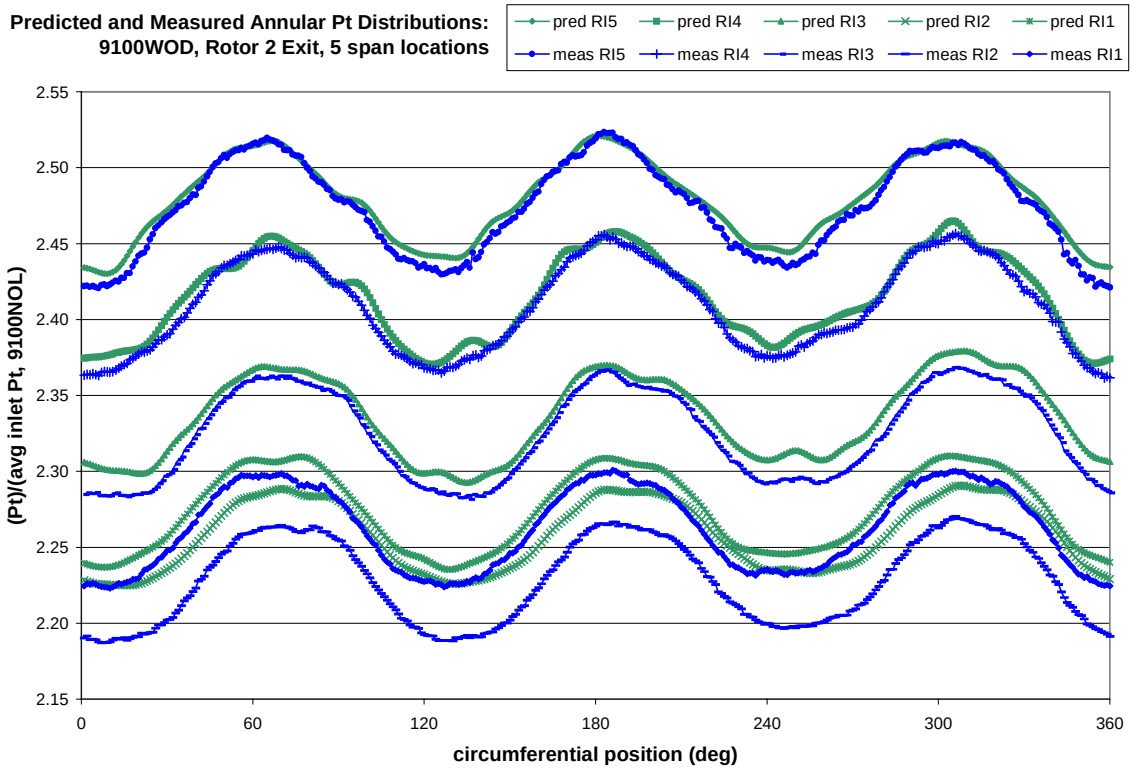

Figure 6.13: Predicted and Measured Annular Pt Distributions 24 Frequency Components, 5 Span Locations, R2 Exit, 9100WOD predicted with R2 9100NOL FRF

The second important point involves the poor prediction of RI2 (bottom blue line). The prediction (bottom green line) has the correct shape, but its average value is too high, creating a vertical offset. This is caused by an incorrect zero frequency (DC term) and does not affect the values presented in table 6.4, but does warrant some discussion.

In all predictions presented thus far, the DC term used in the FRF was the DC term measured at the point at which the FRF was created. For this case, it is the DC term from the second rotor at 9100NOL. Until now, predicted rotor 1 total pressure profiles have had good vertical alignment in the presented plots, since their average value was correctly predicted. This indicates that rotor 1's pressure ratio is fairly constant along the speedline, i.e. the rotor's characteristic is relatively flat at this speed.

These data show that rotor 2's characteristic is more steeply inclined, creating a pressure ratio that is more dependent on mass flow. Prediction of individual rotor or overall machine pressure ratio is not included in the scope of this work. In the interest of plotting efficiency, unless otherwise noted, the remaining time domain predictions

presented in this tome have their average value set equal to measured average values. In practice, this is a fairly simple procedure and is accomplished by replacing the FRF's zeroth frequency component with that measured at the prediction point.

The pressure ratio adjusted 9100WOD rotor 2 prediction is presented in figure 6.14. It contains the same predictions as those in figure 6.13, except that they appear to have higher accuracy because they match the vertical position of the measured profiles.

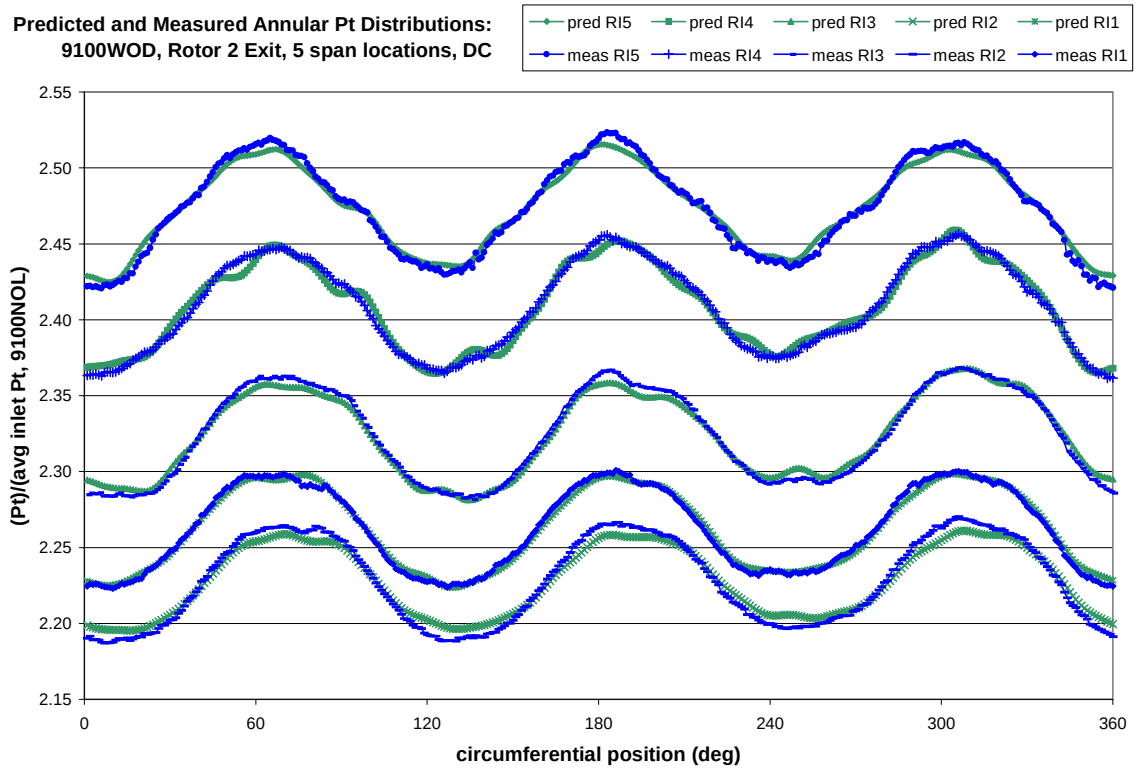

Figure 6.14: Predicted and Measured Annular Pt Distributions 24 Frequency Components, 5 Span Locations, R2 Exit, 9100WOD predicted with DC Adjusted R2 9100NOL FRF

Accurate FRF model predictions are not limited to low rotor speeds. Figure 6.15 presents the results of using an FRF to model (with no DC adjustment) created across rotor 1 at 13200rpm (99%Nc) with an 8/rev distortion to predict the PE&NS condition at the same speed. Accuracy is good, although the phasing of the prediction lags the measurement by several degrees. A comparison of frequency component prediction accuracy, figure 6.16, shows that the primary (8/rev), ½ (4/rev) and second (16/rev) harmonics are very well predicted. Prediction accuracy at this aerodynamic loading

condition is representative of accuracy obtained at the other throttle setting (WOD) along this speedline. Results are summarized in table 6.5. Prediction accuracy for this speed is of the same order as that for the 69%Nc case examined previously.

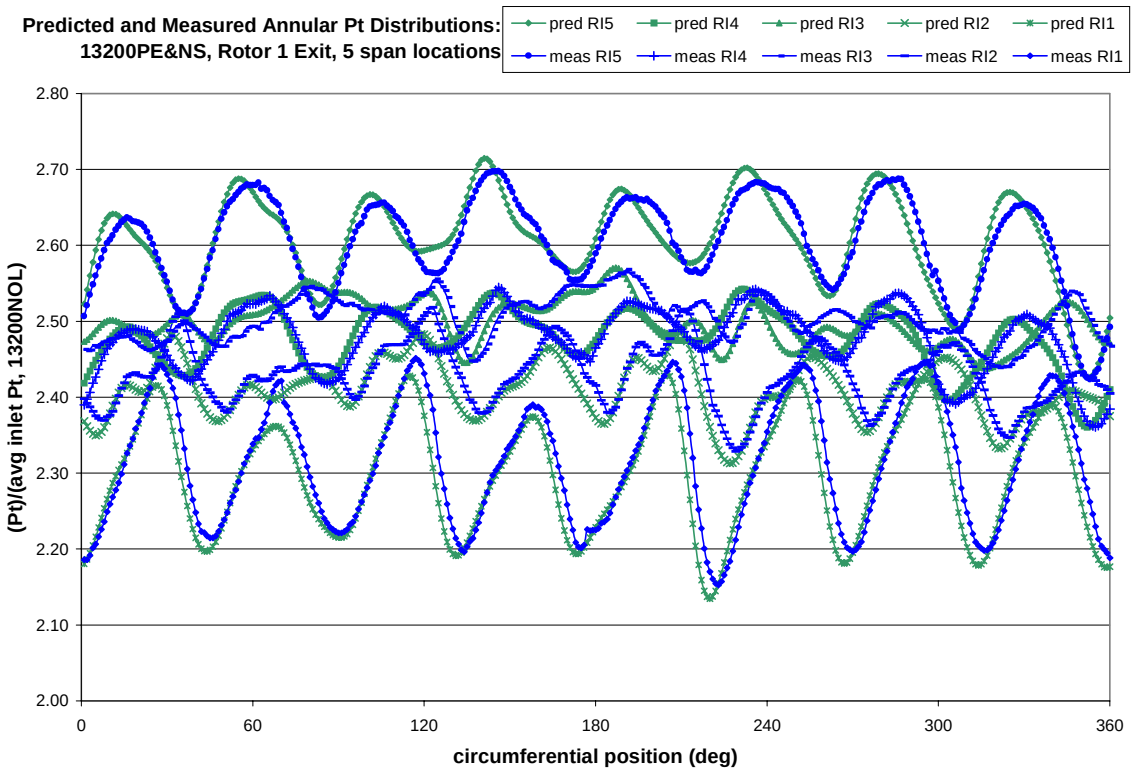

Figure 6.15: Predicted and Measured Annular Pt Distributions 24 Frequency Components, 5 Span Locations, R1 Exit, 13200PE&NS predicted with R1 13200NOL FRF

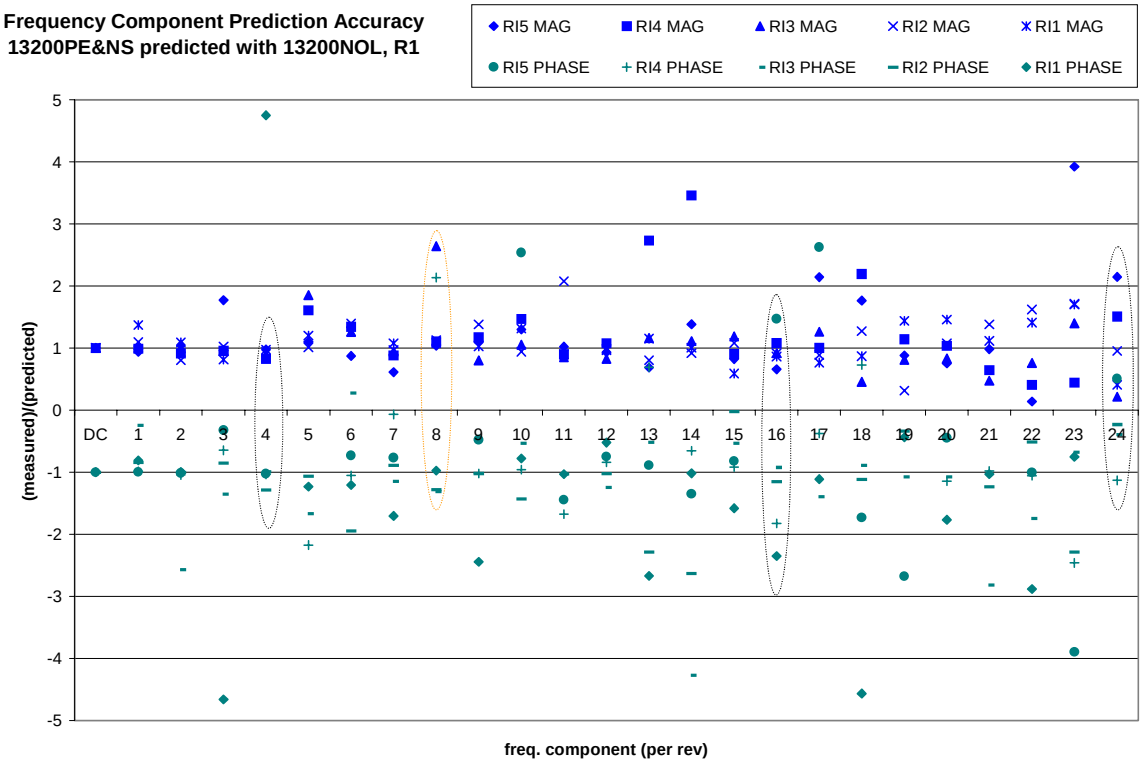

Figure 6.16: Frequency Component Prediction Accuracy, 13200PE&NS Predicted with 13200NOL

Prediction Accuarcy Along 13200rpm Speed Line Using 13200NOL Model: Rotor 1					
	RI1	RI2	RI3	RI4	RI5
NOL	0.000%	0.011%	0.002%	0.011%	0.002%
WOD	0.006%	0.052%	0.244%	0.027%	0.034%
PE&NS	0.531%	0.212%	0.017%	0.216%	0.163%

Table 6.5: Normalized Percentage Difference Between Measured and Predicted Average Variation from Mean, of Predictions Along R1 13200 Speedline Made with R1 13200NOL model

Results from rotor 2 and part speed (9500rpm) are of similar accuracy and are omitted for brevity.

6.6 Fundamental Frequency Response Function Model Applied to "Far" Points

As shown in the previous section, an FRF can be used to create highly accurate predictions of annular total pressure profiles downstream of turbomachinery rotors for operating points on the same speed line at which the FRF was derived. Depending on the degree of dependence of pressure rise on mass flow, a correction may have to be applied to match predicted with measured average pressure values.

The prediction of other aerodynamic loading conditions at the same rotor speed is of limited use, and the value of FRF predictors as distorted compressor flow models would be enhanced if they had general applicability. The degree of applicability is investigated in this section by using FRF's to predict flow behavior at dissimilar operating conditions than those at which they were derived.

The previously examined R1 FRF derived at 9100NOL is used in figure 6.17 to predict the rotor 1 outlet total pressure profile at 13200PE&NS. The operating conditions at which the FRF is calculated and driven are widely divergent: 69% vs. 99%Nc, 3/rev vs. 8/rev distortion, as well as having different aerodynamic loading.

Prediction accuracy is very poor, which is a manifestation of the highly nonlinear compressor behavior between these two operating conditions. A comparison of the frequency domain prediction accuracy, figure 6.18, with that calculated when the 13200NOL FRF was used as the predictor, figure 6.16 show decreased accuracy at all frequencies, especially harmonics. These results show that the investigated rotor responds to an 8/rev distortion at 99% speed dissimilarly than it does to a 3/rev distortion at 69% speed. This result is expected since these flow conditions are very dissimilar, and compressor response is strongly nonlinear. Results are slightly improved, when the flow conditions are used that are still dissimilar, but share a common characteristic, namely distortion frequency.

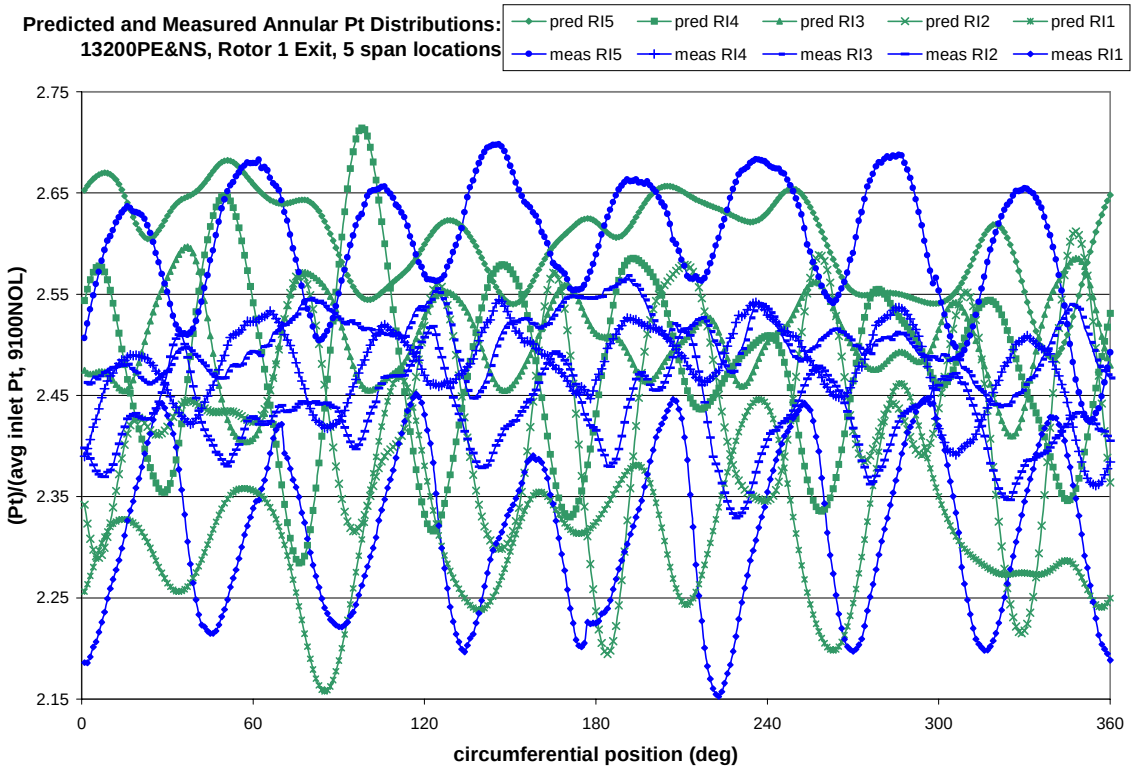

Figure 6.17: Predicted and Measured Annular Pt Distributions 24 Frequency Components, 5 Span Locations, R1 Exit, 13200PE&NS predicted with R1 9100NOL FRF

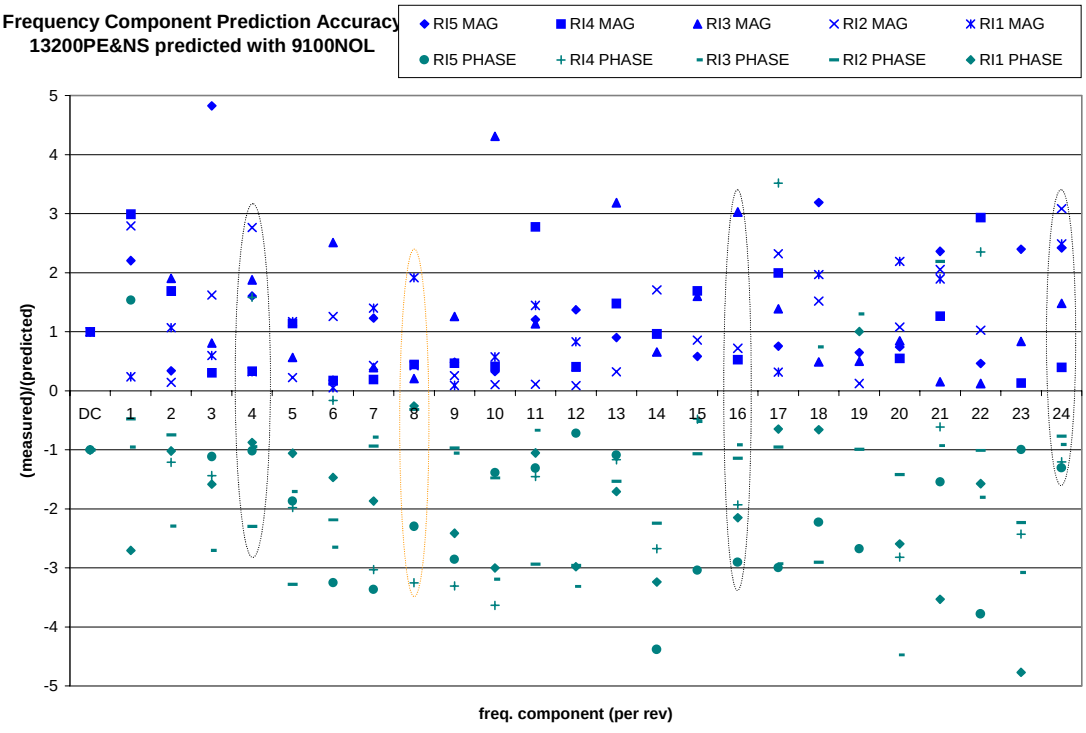

Figure 6.18: Frequency Component Prediction Accuracy, 13200PE&NS Predicted with 9100NOL

Figure 6.19 presents a prediction of the same 13200PE&NS condition examined in figure 6.17, using instead an FRF calculated at 9500NOL (72%Nc). While this is a part speed flow condition, like that of 9100NOL, data at the 72% speed was measured while operating with an 8/rev distortion. Resulting prediction accuracy is therefore improved, although the still relatively poor results indicate a strong dependence on rotor speed, aerodynamic loading (since the FRF was developed at NOL and the prediction made at PE/NS) or both.

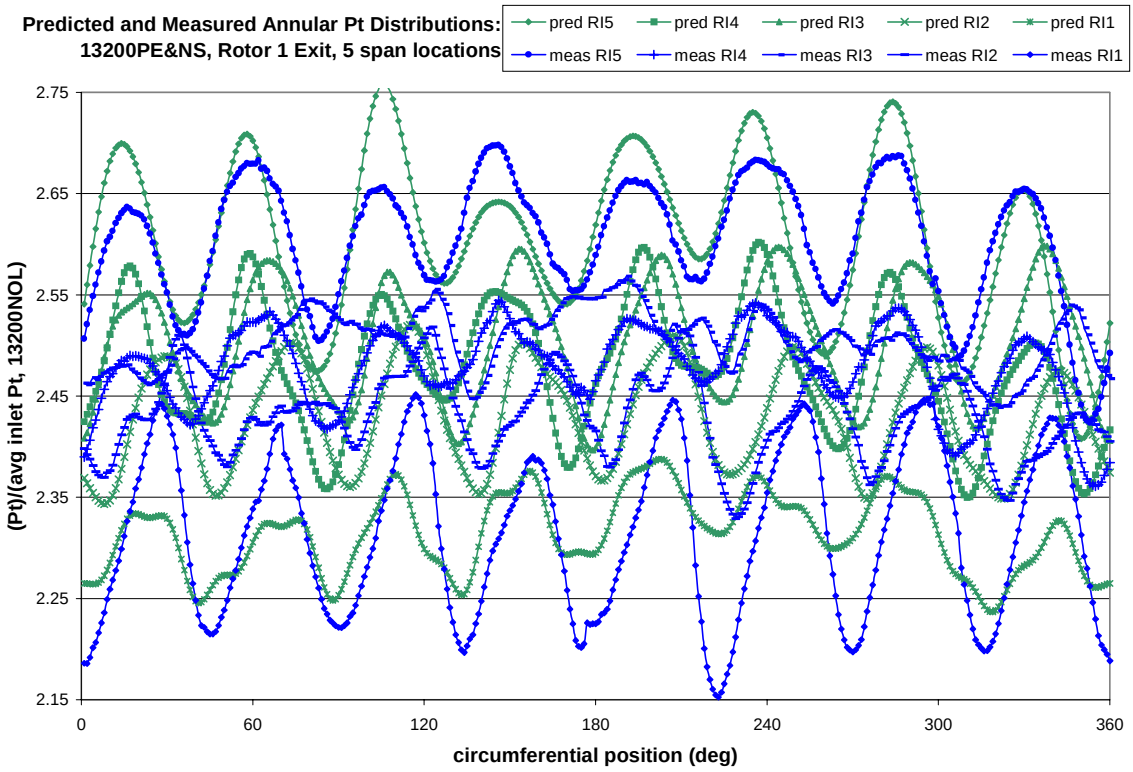

Figure 6.19: Predicted and Measured Annular Pt Distributions 24 Frequency Components, 5 Span Locations, R1 Exit, 13200PE&NS predicted with R1 9500NOL FRF

Predictions at some span locations, especially near the hub, are reasonable. Figure 6.20 shows individual RI5 results taken from figure 6.19. Improved prediction accuracy near the hub is attributed to the flow in that span region behaving more linearly than that near the tip. This is attributed to the absence of two nonlinear, speed- dependent flow phenomena at the hub: tip leakage flow and blade passage shock structure.

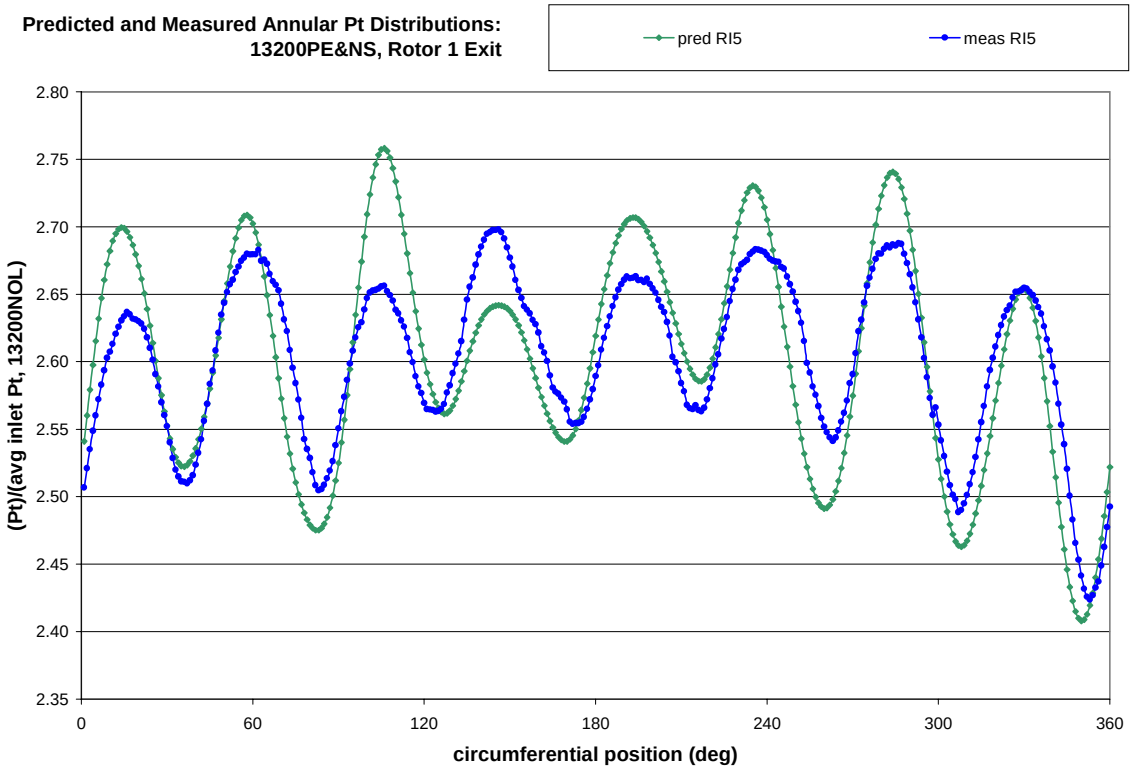

Figure 6.20: Predicted and Measured Annular Pt Distributions 24 Frequency Components, RI5 Span Location, R1 Exit, 13200PE&NS predicted with R1 9500NOL FRF

A lack of improvement in prediction accuracy of 13200PE&NS rotor 1 exit total pressure profile is seen when using an FRF derived at a similar throttle setting (9500PE). This indicates that prediction accuracy is much more strongly dependent on rotor speed then aerodynamic loading. Results of this prediction are shown in figure 6.21, and are similarly poor to those in figure 6.19. This is an expected result, given that it was previously shown that FRF predictions along a given speed line are very weakly dependent aerodynamic loading.

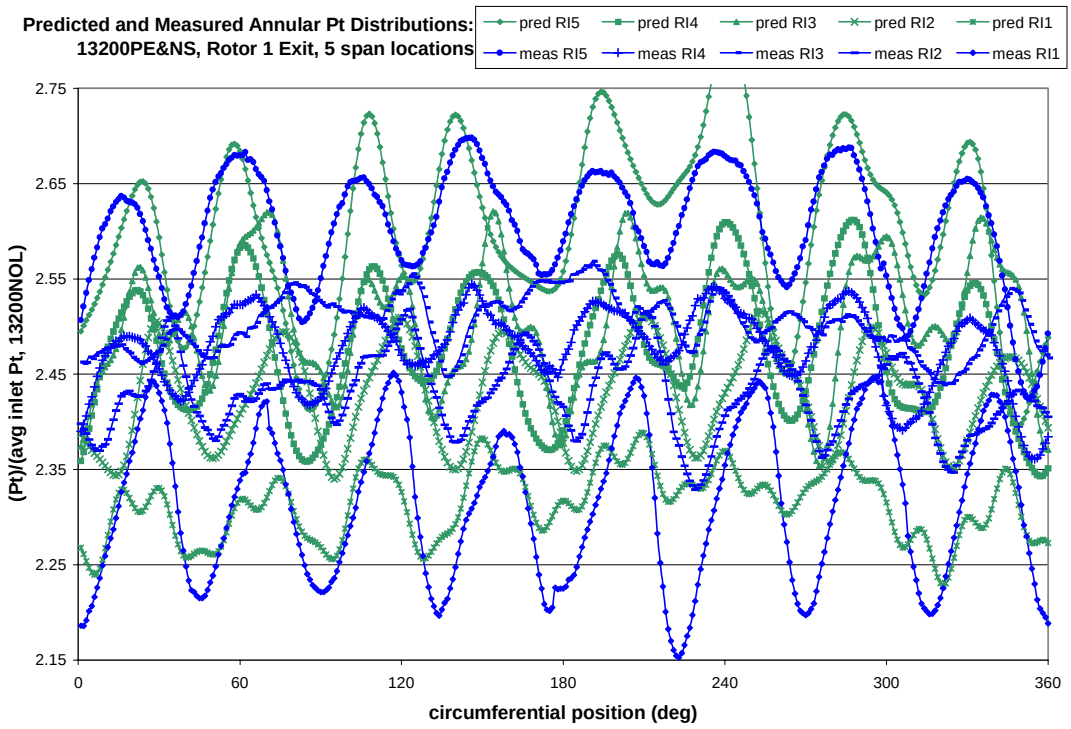

Figure 6.21: Predicted and Measured Annular Pt Distributions, 24 Frequency Components, 5 Span Locations, R1 Exit, 13200PE&NS predicted with R1 9500PE FRF

The ability of a given FRF to produce accurate predictions has thus far been shown to be strongly dependent on differences in rotor speed between the point at which the FRF was calculated and the point being predicted. A strong dependence on throttle setting has not been found either along the same speedline or between speedlines.

A lack of data prevents direct investigation of the effect of distortion type on fundamental FRF prediction accuracy. No data set is available at which the compressor was run at the same operating point with distortions of different frequency at the inlet. However, as a proxy case, data from the two part speed runs will be used to examine the effect of distortion type on FRF predictions.

As a representative case, an FRF calculated across R1 at 9500NOL (8/rev distortion) is used to predict the rotor's outlet annular total pressure profile while operating at 9100NOL (3/rev distortion). Results are shown in figure 6.22. Overall prediction accuracy is poor, although as previously seen, the span location near the hub is the best of the five radial locations examined. This location, RI5, and RI1 are shown together in figure 6.23.

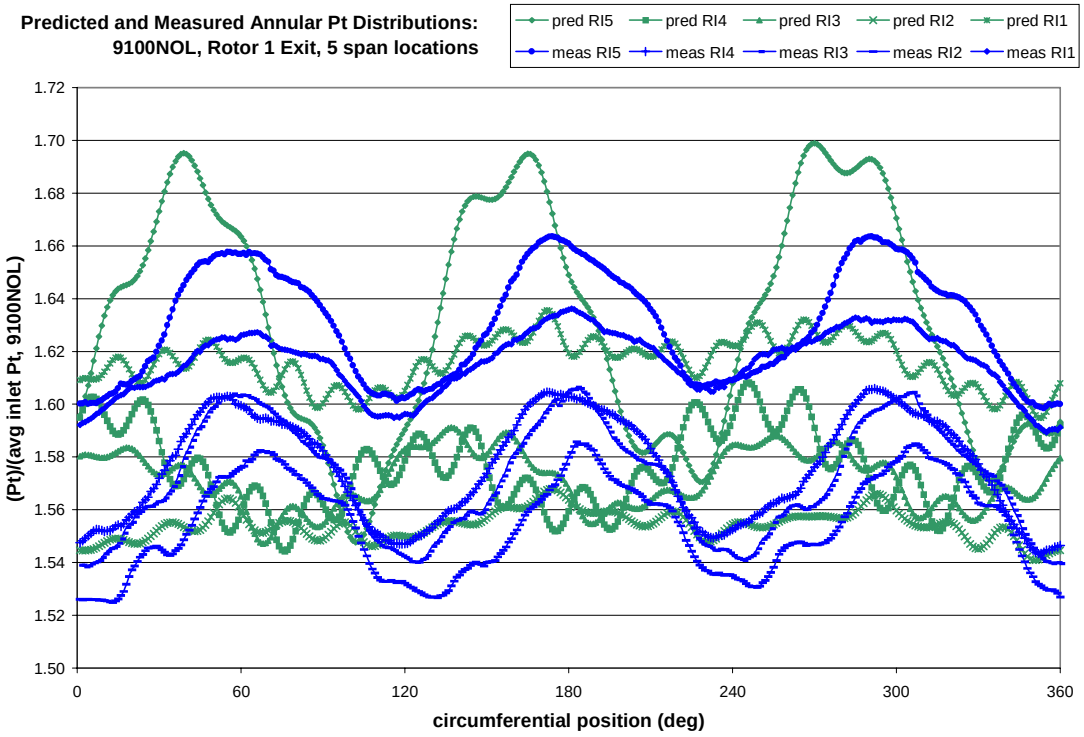

Figure 6.22: Predicted and Measured Annular Pt Distributions, 24 Frequency Components, 5 Span Locations, R1 Exit, 9100NOL predicted with R1 9500NOL

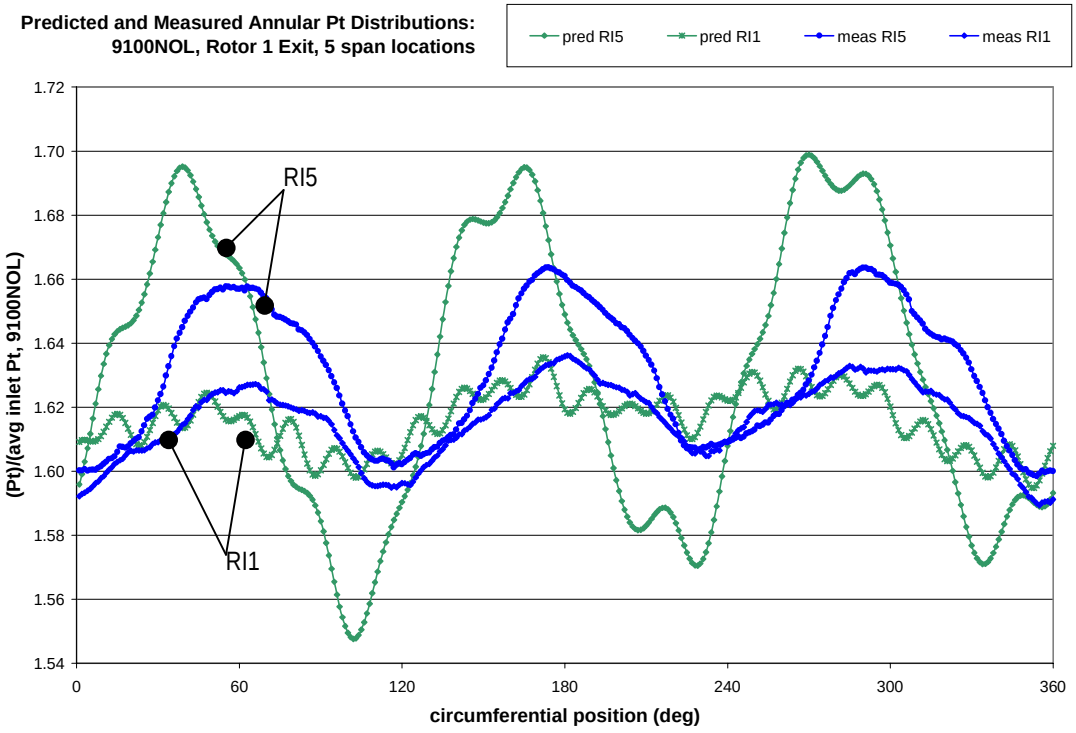

Figure 6.23: Predicted and Measured Annular Pt Distributions, 24 Frequency Components, 2 Span Locations, R1 Exit, 9100NOL predicted with R1 9500NOL

Surprisingly, the FRF developed with 8/rev distortion correctly predicts 3/rev dominance of the 9100rpm distortion profile at RI5. However, this is not seen at all span locations, including RI1, where the predicted primary frequency is neither 8/rev nor 3/rev, but something much higher. Primary frequency amplitude is not predicted correctly at any radial location.

Based on the cases examined in this study, frequency response function prediction capability is strongly dependent on rotor speed and, to a lesser extent, on distortion type.

As a final case, the dependence of FRF prediction accuracy on the specific geometry and blade row aerodynamic design of a given rotor is investigated. This is done by examining the prediction accuracy of an FRF calculated with rotor 2 data at 13200PE&NS and used to predict the total pressure distribution downstream of rotor 1 at the same operating condition. Figure 6.24 shows that overall prediction accuracy is very poor.

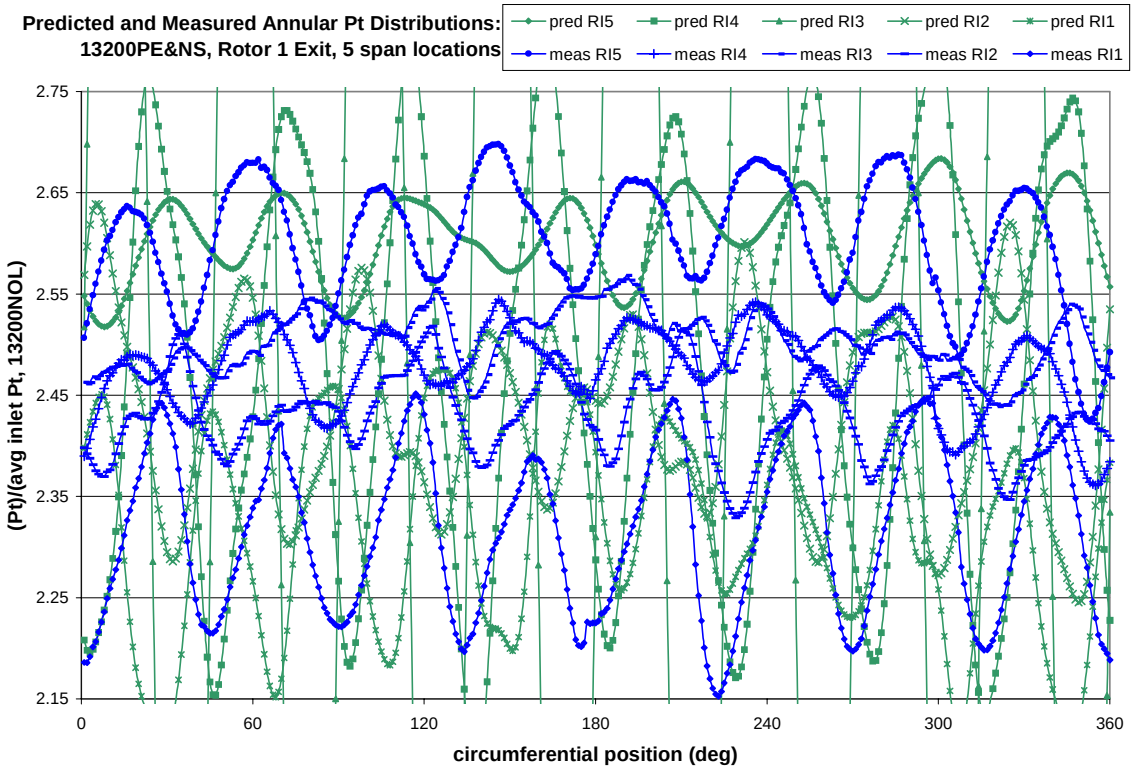

Figure 6.24: Predicted and Measured Annular Pt Distributions, 24 Frequency Components, 5 Span Locations, R1 Exit, 13200PE&NS predicted with R2 13200PE&NS

Accuracy at some span locations is somewhat better than that seen at others. Radial positions 5 and 1 are the best, although as a general rule, FRF's developed on one of the two rotors used in this program cannot be used to produce prediction of high accuracy of flow through the other.

The results of the representative cases presented here are summarized in table 6.6. It is seen that FRF prediction accuracy is most sensitive to the action of a specific rotor. Other parameters prevent the general applicability of a given FRF as well, including rotor speed and to a lesser extent aerodynamic loading.

Prediction Accuarcy of 13200PE&NS Using Various FRF's: Rotor 1						
	RI1	RI2	RI3	RI4	RI5	avg. acc.
9100NOL	1.695%	4.418%	1.123%	4.264%	1.215%	2.543%
9500NOL	3.929%	1.310%	2.658%	1.942%	1.770%	2.322%
9500PE	4.107%	1.130%	2.928%	2.634%	2.731%	2.706%
R2 FRF	1.650%	4.800%	78.559%	15.374%	1.503%	20.377%

Table 6.6: Normalized Percentage Difference Between Measured and Predicted Average Variation from Mean, of Predictions of R1 13200 PE&NS Conditions Made with Several FRF's

6.7 Staging of the Fundamental Frequency Response Function Model

An interesting application of the fundamental modeling technique is to the prediction of flow transport through several stages of compression. This is accomplished by staging individual FRF's such that the output of a given upstream FRF corresponds to the input of the corresponding downstream FRF. This process is shown for a representative case; 13200PE&NS.

Using FRF's developed at the 13200NOL condition as predictors, the staging process begins by computing a prediction of the total pressure profile downstream of the first stage rotor. This is shown in figure 6.15. Since the predicted data set is along the same speedline as the FRF, prediction results are very accurate. The predicted

distribution is then used to force the FRF measured across the second stage rotor. Downstream prediction results are shown in figure 6.25.

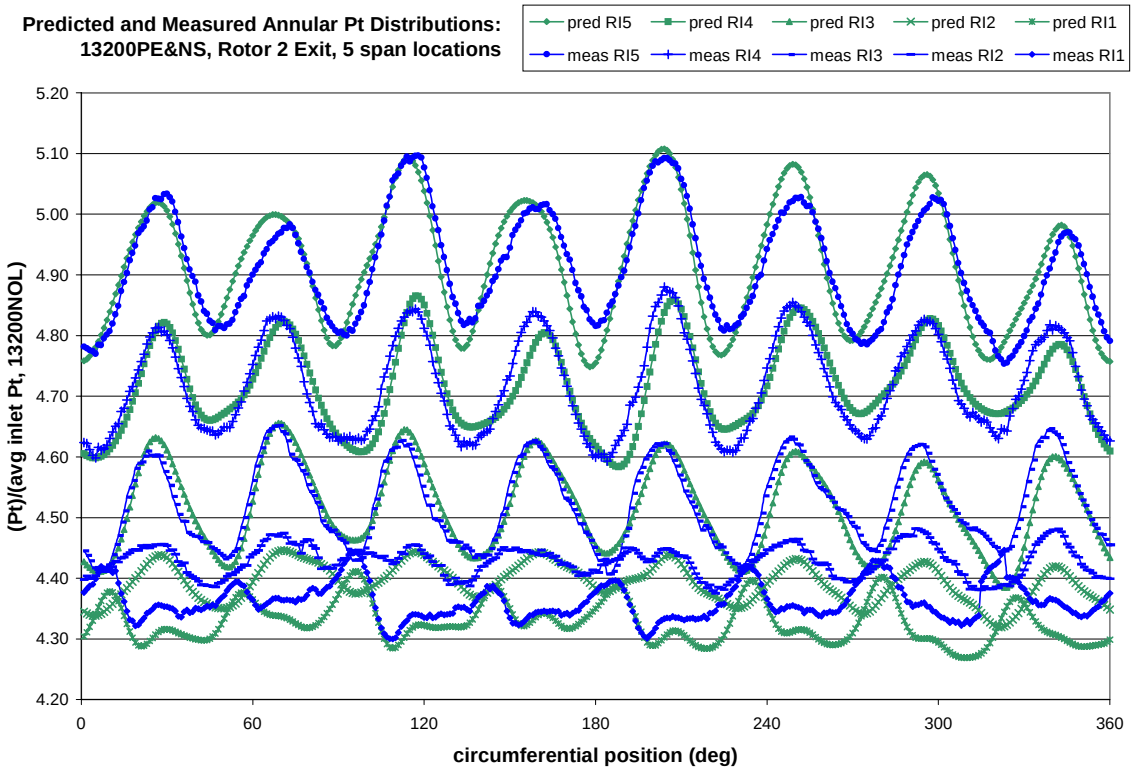

Figure 6.25: Result of Staging FRF's through 2 Stages, Predicted and Measured Annular Pt Distributions 24 Frequency Components, 5 Span Locations, R2 Exit, 13200PE&NS predicted with R2 13200NOL FRF

Strong dependence of pressure ratio on mass flow through the second rotor at this stage required DC adjustment of the prediction to match the average value of measured distributions. Otherwise, prediction accuracy is very good, due in part to good prediction accuracy of second stage inlet (small upstream error to propagate through the second stage).

If appropriate FRF's descriptors of each compression stage are available, this process can be used to determine flow conditions in the back stages of a machine where direct measurement is difficult, expensive or not available.

6.8 Summary of Fundamental Frequency Response Function Modeling Results

The relatively high prediction accuracy seen along an individual speedline is attributed to two phenomena, both related to the inherently linear nature of the FRF approach. For an FRF to be used as an effective system model, the system must either *be* or *act* linear. The test compressor used in this work is both, depending on rotor speed. Accurate predictions along low- speed speedlines are attributed to the pseudo- linear behavior at these operating conditions. Indeed, the compressor's characteristic map is fairly flat in this region. Near design speed, the characteristic approaches a vertical line, indicating that blade loading is highly dependent on mass flow and tends to create strongly nonlinear behavior. However, various aerodynamic loading conditions occur over a small mass flow range; the result is that the rotor's distortion response acts linear.

In general, FRF's used to predict flow conditions on a different speedline from which they were calculated yield poor prediction accuracy. It is found that FRF's have varying sensitivity to several important flow parameters, and the results are recapitulated as follows.

Based on the data used in this study, the ability of a given FRF to predict flow conditions different from those at which it was calculated has the following levels of dependence:

- very weakly dependent on blade row aerodynamic loading
- strongly dependent on rotor speed
- strongly dependent on distortion frequency and intensity
- very strongly dependent on rotor (FRF's can't be used for a different rotor than the one they were calculated across)

These dependencies restrict the use of this fundamental FRF modeling method to points only along the same speedline, operating with the same upstream distortion, than those that at which the FRF is calculated. A "tuning" method developed in the next chapter removes these restrictions, allowing the calculation of FRF's that are applicable to a wide range of flow and distortion conditions.

7 Frequency Response Function Model Tuning: Method and Results

The capability of the fundamental FRF modeling technique was investigated in the previous chapter and it was found that the method has limited applicability. A given FRF was seen to produce accurate predictions only for flow conditions similar to those at which it was calculated. Predictions made of data measured at other rotor speeds and distortion frequencies were poor. The method presented in this section adjusts, or "tunes" (literally adjusting the frequency components) the FRF so that its prediction accuracy is improved for dissimilar flow conditions. The method is empirically- based, although a small baseline data set is required for calibration.

The method proceeds as follows. Frequency response functions are obtained using experimentally measured total pressure response for several operating conditions. These data are transformed into sets of dependent and independent variables whose resulting correlations permit the characterization of other, disparate flow fields. Once a flow field of unknown response is characterized, the FRF is tuned to match the rotor's operating conditions and the properties of the inlet flow-field.

Although the tuning method generalizes the applicability of the FRF model, it is not intended to predict all properties of the compressor flow. Like the fundamental model, steady circumferential total pressure distributions are predicted, but with two limitations. First, average total pressure is not predicted; only deviations from the mean are computed. This equates to including all components in the FRF but the zeroth frequency. Accordingly, the distortion profile is predicted, allowing examination of frequency content transport through the rotor and possible downstream forcing functions.

Second, frequency domain phase is not part of the FRF tuning method. This prevents the prediction of the relative clocking (time and spatial domain phase) of the distortion profile. Although the phase portion of the FRF affects both the clocking and the shape of the predicted distortion, it was found that reasonable shape prediction could be achieved by assuming that each component frequency had the same phase value. Unless otherwise stated, all predictions presented in this chapter have been

circumferentially aligned with experimental data. A crude clocking prediction can be included in the FRF, and this is examined further in section 7.3.

As a consequence of developing this tuning method, a turbomachinery rotor's FRF was found to be a function of primarily the following five parameters:

- distortion intensity
- rate of change in total pressure as seen by the blade row
- blade passage shock strength
- fluid axial velocity
- blade chord length

These parameters are quantitatively incorporated into the tuning procedure developed in this chapter.

7.1 Development of Empirical Functionals

The FRF tuning procedure is based on two empirically- derived functional correlations. One determines the magnitude of the prediction's primary frequency; the other gives the magnitude of all other frequency components relative to the primary.

The independent variable used in the primary frequency correlation is a development of this study and is termed the *reduced distortion rate* or RDR. Based on time domain characteristics of the inlet distortion, rotor speed and fluid velocity, the RDR is defined as

$$\mathrm{RDR} = \frac{\frac{dP_t}{dt}\left(\frac{\mathrm{chord}}{\overline{C_z}}\right)}{\left(\overline{P_t}\right)_{\mathrm{ring}}}$$

where $\frac{dP_t}{dt} = \mathrm{P_t}$ average rate of change as seen by blade row at a given radial position

Equation 7.1

The normalization term is the average total pressure around a ring of constant span. Note that the total pressure rate of change is a function of both the upstream distortion and rotor speed. The time derivative of discrete inlet data is calculated numerically. The RDR is similar to most forms of the reduced frequency parameter (see chapter 2), with one important exception. Instead of including only the number of distorted sectors per revolution, the RDR contains the rate of change of distortion, thereby more fully characterizing the nonuniform flow. Usage of the RDR and the reduced frequency for this study is compared later in this section.

The dependent variable used in this correlation is related to the FRF's primary frequency. A scaled value of the primary frequency is used, and the scaling parameters are used to partially account for nonlinear behavior. (The remaining adjustment occurs in the correlation relationship itself.) These parameters are a blade passage shock strength correction factor and distortion intensity correction factor.

The shock strength factor removes pressure changes induced by the shock so that correlations occur as if all operating conditions have a subsonic blade passage trough flow velocity. As described in chapter 4, a streamline curvature approach is used to determine blade passage shock upstream Mach number. The blade passage shock structure is assumed to consist of a single normal shock allowing determination (using standard normal shock relations) of the shock- induced total pressure loss and static pressure rise through the blade row. Recall that FRF component magnitudes are the total pressure ratios at each frequency. Therefore, to remove the effect of the shock from the primary frequency, the measured primary frequency magnitude is multiplied by the ratio of static pressure loss to total pressure gain across a normal shock with the SLC computed upstream Mach number. The use of a normal shock model is a gross simplification of the time dependent oblique normal shock system in the blade passage. However, good results are obtained with this assumption, and more complex numerical methods to capture the actual time dependent structure are not in keeping with the philosophy of this study. If it were necessary to use a CFD model, for example, to obtain blade passage structure, the present FRF method would be redundant.

The second factor used to scale the dependent variable in the primary frequency correlation is the distortion intensity factor. This is simply a measure of the intensity, or

total pressure amplitude, of the inlet nonuniformity. The distortion factor used in this study is closely related to that set forth by the Society of Automotive Engineers (SAE) in their Aerospace Information Report (AIR) 1419 document. The SAE AIR1419 distortion criterion, widely quoted throughout the compressor community, was originally developed for thermodynamic performance evaluation. The parameter used in this study modifies the AIR1419 criteria by averaging the pressure deficits caused by each distorted sector, instead of using the sector with strongest deficit as representative of the entire inlet flow-field. The intensity parameter ($\Delta PC/P$) used here is defined as

$$\frac{\Delta PC}{P} = \frac{P_{ring\ avg} - P_{low\ avg}}{P_{ring\ avg}}$$

where $P_{ring\ avg}$ = average circumferential Pt at radius of intrest
$P_{low\ avg}$ = average Pt at all measurement locations with a pressure lower than ring average

Equation 7.2

The FRF's primary frequency magnitudes are normalized for a distortion intensity of unity (divided by $\Delta PC/P$) for use in the correlation.

Computed RDR and scaled primary frequency magnitude for data sets from both the first and second stage rotors used in this study are presented in figure 7.1. Although data from each rotor follows a different relational curve, both sets exhibit the same type of behavior. While rotor 1 data covers a wide range of RDR (enough to define the shape of the fit line), inlet data to rotor 2 occurs over a comparatively small range. Consequently, the behavior of rotor 2 in the RDR- FRF scaled primary frequency plane has not been fully defined. This prevents further use of rotor 2 data in this study. It is maintained that if the experimental data set were larger, the proceeding results could be extended to rotor 2. In developing a test plan to use with this method, one would need to ensure that data were collected over a sufficient RDR range to allow full characterization of rotor response. Note that a fairly small amount of data (three speeds, two screens) were used here to fully characterize the first stage rotor, indicating that a properly structured experimental program could expeditiously acquire the necessary data.

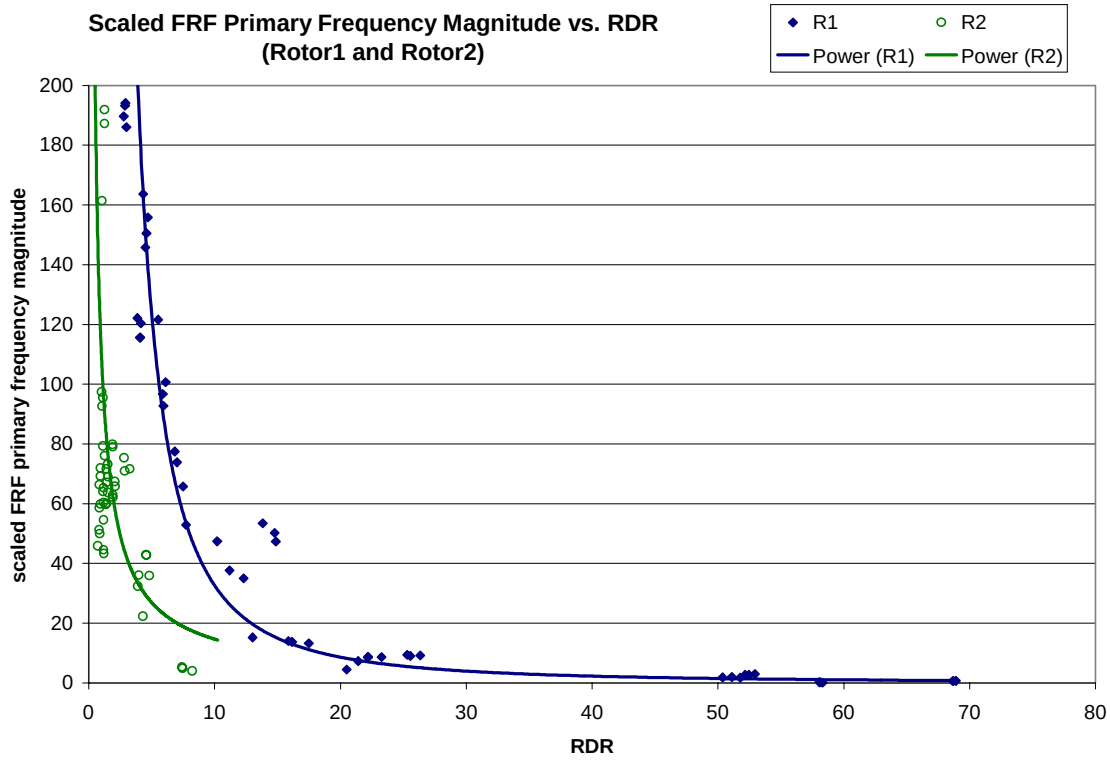

Figure 7.1: Scaled FRF Primary Frequency Magnitude vs. RDR with Best-Fit Lines, Rotors 1&2

A power function fits the first stage rotor data well (the coefficient of determination, R^2=0.89). This indicates that the functional relationship between RDR values and scaled FRF primary frequency magnitude is a function of fundamental interactions among the rotor and distorted flow-field. Dependence on operating condition (rotor speed, downstream throttle setting, distortion frequency and intensity) and span location have been removed. This is a significant step toward generalizing the FRF modeling method.

Examination of figure 7.1 reveals that rotor response as a function of RDR behaves qualitatively like that of reduced frequency. Lower values indicate increased rotor response, while reduced rotor response is expected for higher values. However, it was found that the reduced frequency does not correlate well with scaled FRF magnitude. Figure 7.2 shows the same FRF magnitude data as figure 7.1, except plotted against k (as defined by Bruce, equation 2.4) instead of RDR. It is readily apparent that, in this

application, reduced frequency does not adequately correlate rotor response. Indeed, R^2=0.45 for this fit line.

Since the rate of inlet pressure change interacts with the time dependent blade aerodynamic response to produce the resulting downstream flow distortion, it is expected that the upstream distortion rate of change (as seen by the rotating blade row) is an important parameter. It is proposed that the RDR is superior in this capacity because, through the use of the derivative of total pressure, it more fully characterizes inlet distortion.

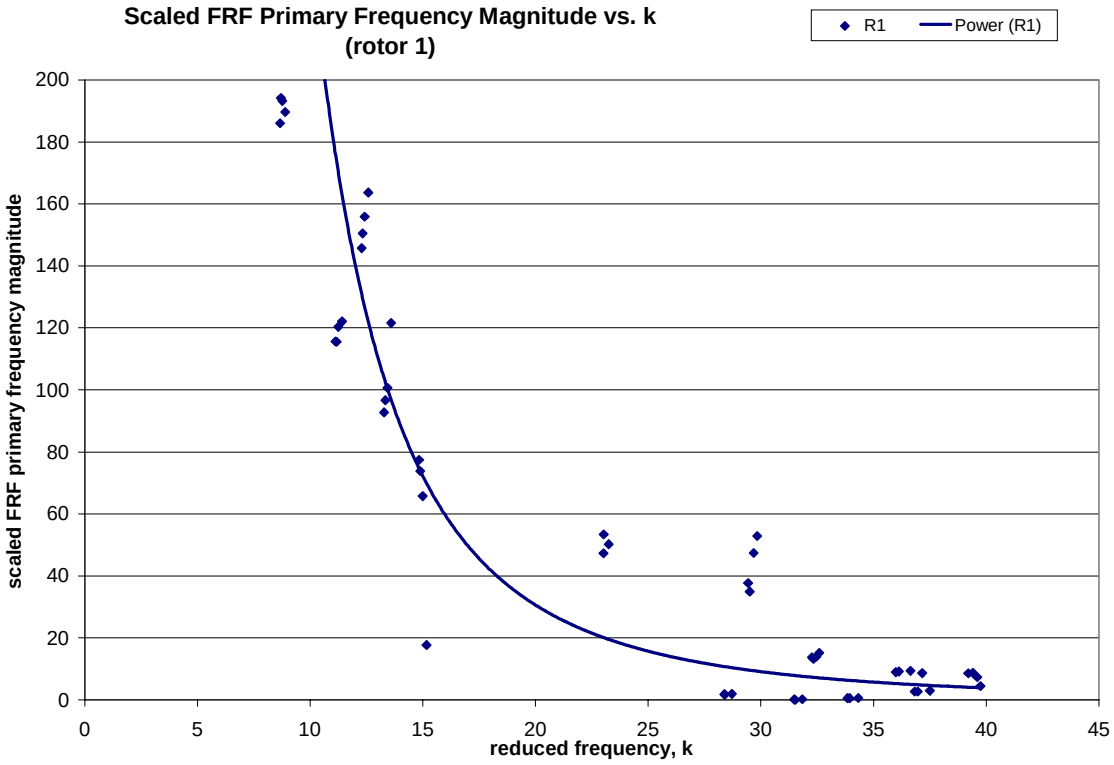

Figure 7.2: Scaled FRF Primary Frequency Magnitude vs. Reduced Frequency with Best-Fit Line, Rotor 1

While the aforementioned procedure provides a means of calculating the appropriate primary frequency magnitude for use in the FRF, the remaining frequency components must also be defined. This is done using the second empirically- based method developed in this study.

In the magnitude plots of output frequency components presented in chapter 5 no pattern or relationship between individual components was readily apparent. Examining the frequency domain representations of inlet data, it is seen that most component magnitudes are much lower than those at the primary frequency. The result of these relatively low component values are seemingly random output frequency magnitudes.

By normalizing output frequency component magnitudes by that at the primary frequency, "noise" caused by low amplitudes is removed. The result of this normalization is a pattern of harmonic behavior that is fairly consistent at all operating conditions examined. Shown in figure 7.3 are outlet frequency component magnitudes for all measured operating conditions, normalized by their respective primary frequency values.

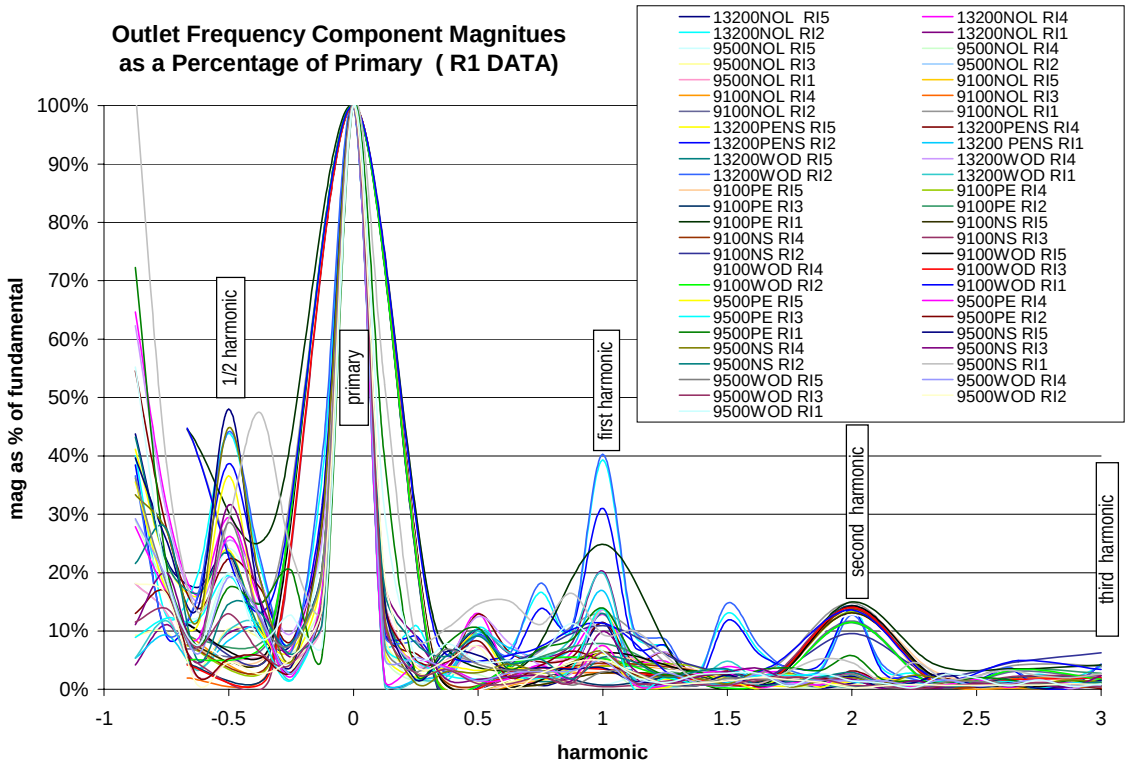

Figure 7.3: Outlet Frequency Component Magnitudes as a Percentage of Primary Frequency Magnitude, all Rotor 1 Data

Data have been aligned at their primary frequencies, indicated by harmonic number zero. When aligned in this manner, it is seen that at most operating conditions, individual normalized frequency component values are within relatively small ranges.

Most non- harmonics have low values, less than 5%, while harmonics fall between 10% to 20%. First component frequency (1/rev) values do have large scatter, but this is attributed to the artificial 1/rev component introduced by the screen rotator (see chapter 4). It is acknowledged that, unlike the FRF primary frequency correlation, this method does not fully generalize rotor response. There are, for example, distortion- type dependencies visible in figure 7.3. Nonetheless, several important features of rotor exit data are found through this method, including the fact that most other component frequency magnitudes are less than 10% of the primary component, and that their variation falls within a relatively small range.

Averaging aligned and normalized rotor 1 data from all measured operating conditions considered in this study creates the empirical correlation between frequency component number and normalized outlet magnitude, figure 7.4. (This is term (2) in equation 7.3 and figure 7.5.)

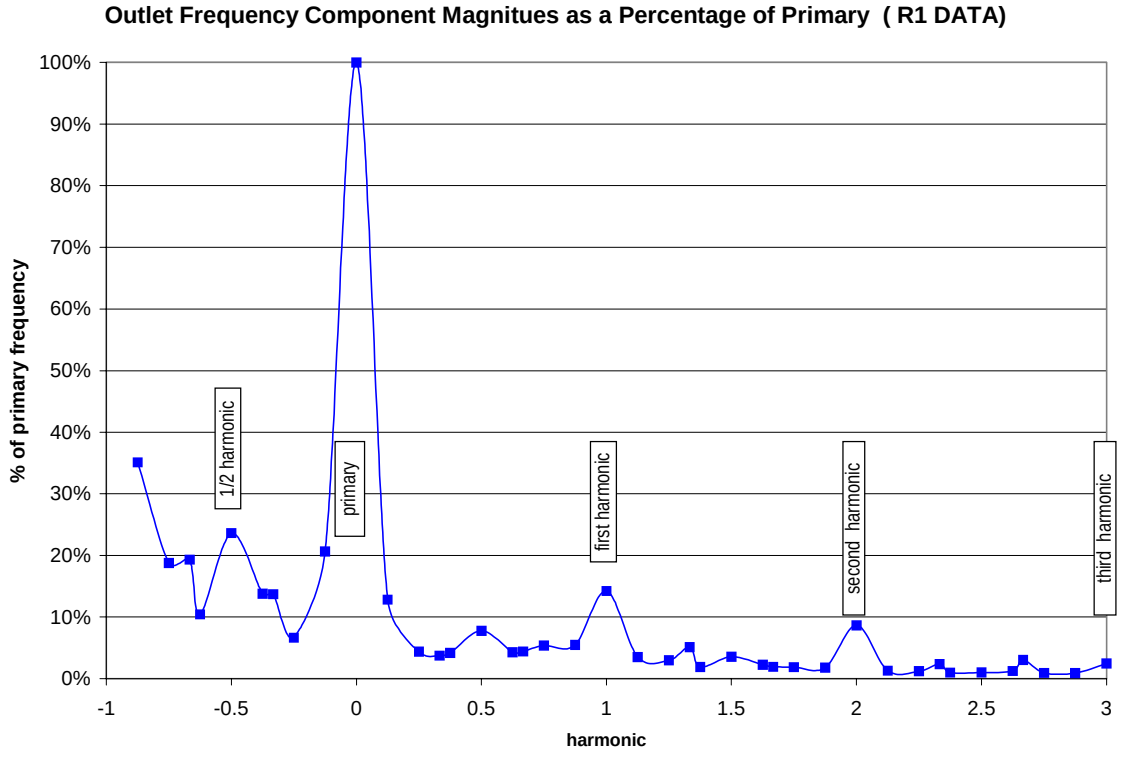

Figure 7.4: Outlet Frequency Component Magnitudes as a Percentage of Primary Frequency Magnitude, Average of all Rotor 1 Data

Two functional correlations have been developed. One provides for calculation of the FRF's primary frequency at a given flow condition, based on characteristics of both the inlet flow-field and rotor. The second correlation gives relative amplitudes of other outlet component frequencies to the magnitude of the outlet primary frequency. For an input total pressure distribution with unknown response, note that the first correlation permits calculation of the corresponding FRF's primary frequency and therefore the primary frequency of the resulting outlet distribution. With that, the remainder of the FRF's frequency components can be tuned, using the second correlation, allowing calculation of outlet frequency magnitudes. An inverse DFT produces the resulting time (and therefore spatial) domain prediction of downstream total pressure. This predictive procedure is examined in the next section.

7.2 Tuned Frequency Response Function Model

The previous section describes the development of two functional correlations derived from experimental data that generalize rotor response to dissimilar flow conditions. In the present section these correlations are incorporated into a method that permits the prediction of rotor exit annular total pressure distributions for given inlet distortions with "unknown" response.

The calculation method leading to a tuned FRF is outlined in figure 7.5. The process begins in the upper left, where an upstream total pressure distribution at a given radial position with unknown response is decomposed into both the time and frequency domains. Time domain information is used, as described in the previous section, to calculate the RDR and thereby the primary frequency magnitude of the corresponding tuned FRF. Inlet frequency domain data is used, along with the second empirical correlation, to calculate the magnitude of the remaining FRF frequency components. (All tuned FRF's presented here include 24 component frequencies.)

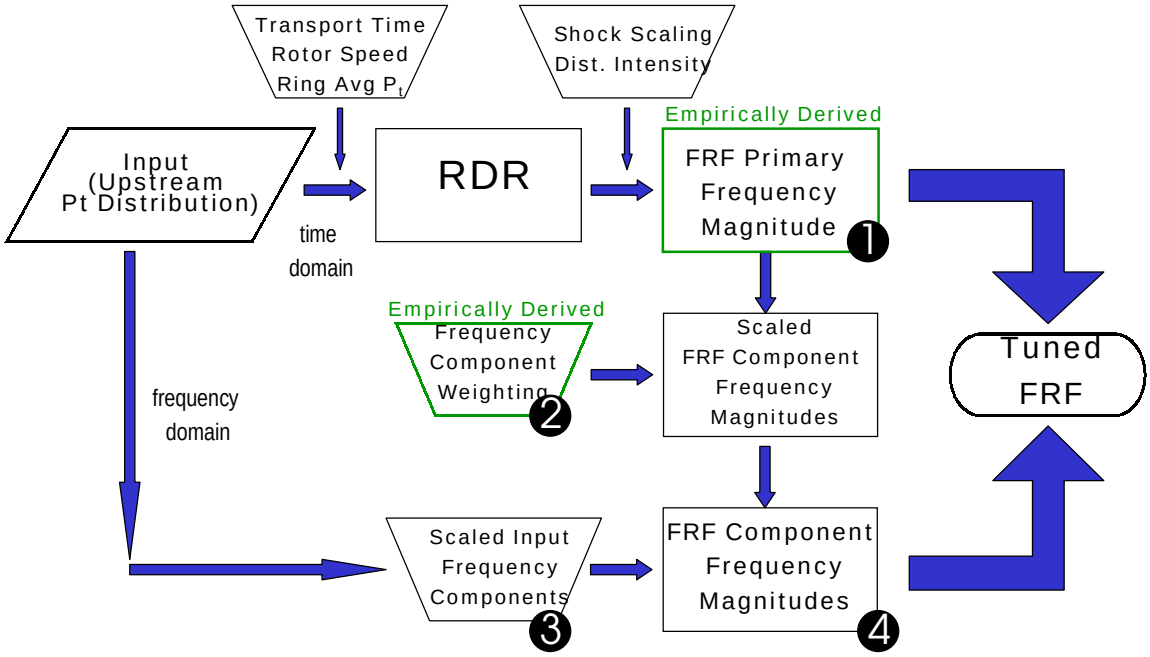

Figure 7.5: FRF Tuning Process

The method used to calculate FRF frequencies other than the primary is further defined by equation 7.3, where the numbered terms correspond to numbered components in figure 7.5.

$$\left(\frac{\text{output}@f_p}{\text{input}@f_p}\right)\left(\frac{\text{output}}{\text{output}@f_p}\right)\left(\frac{\text{input}@f_p}{\text{input}}\right)=\left(\frac{\text{output}}{\text{input}}\right)$$

1 Tuned Primary Frequency Magnitude

2 23 Empirical Weighting Factors

3 23 Upstream Distortion Weighting Factors

4 23 Tuned FRF Magnitudes

where f_p= primary frequency

Equation 7.3

The tuned primary frequency magnitude (1) is combined with the second empirical correlation (2) and frequency domain data of the input (3) to create 23 (24-primary) tuned FRF components (recall that the FRF is defined as the ratio of the output to the input).

The previously computed primary frequency is coupled with the 23 minor frequencies to create an FRF which is tuned to model the rotor exit total pressure distribution, based on the inlet pressure distribution and rotor operating characteristics.

When predicting the response of a given data set, all data measured along the same speed line are removed from both empirically derived correlations. For example, when a prediction of the 9100NOL condition is made, all 9100rpm data is removed from the correlations and corresponding best-fit line equations are recomputed. This is done for two reasons. First, it was seen in chapter 6 that FRF's calculated from data measured along the same speedline produce accurate predictions of rotor exit flow. To prevent "cheating" of the tuning method by including measured FRF data that is known to inherently give accurate predictions (FRF's measured at the same speed, but with different mass flows), FRF's measured at the same rotor speed condition as the prediction are removed. The second reason to handle data this way is a product of the experimental procedure used to collect data. It is unlikely that one would use a model to predict flow behavior at a given mass flow condition if other data points along the same speedline were collected to calibrate the model. A more vigorous treatment of the technique is achieved if it is used in a practical context.

A problem arises if all data at a given speed (essentially 1/3 of the data) is removed from the correlations when a prediction is made. If data taken at equal rotor speeds are highlighted in the R1 RDR vs. scaled FRF primary frequency plot (figure 7.6), it is seen that removal of any set of speed data would markedly change the best-fit line. Since data taken at only three speeds are available, and upstream distortions caused a strong dependence of RDR on rotor speed, removal of one speed group essentially forces the highly nonlinear exponential fit line to be calibrated using only two data "points" (or sets at similar operation). This is a limitation of the available data, and it is anticipated that this could be avoided with a properly structured experimental program.

Nevertheless, the development of this FRF tuning method with a minimal data set is a testament to the method's robustness and is encouraging.

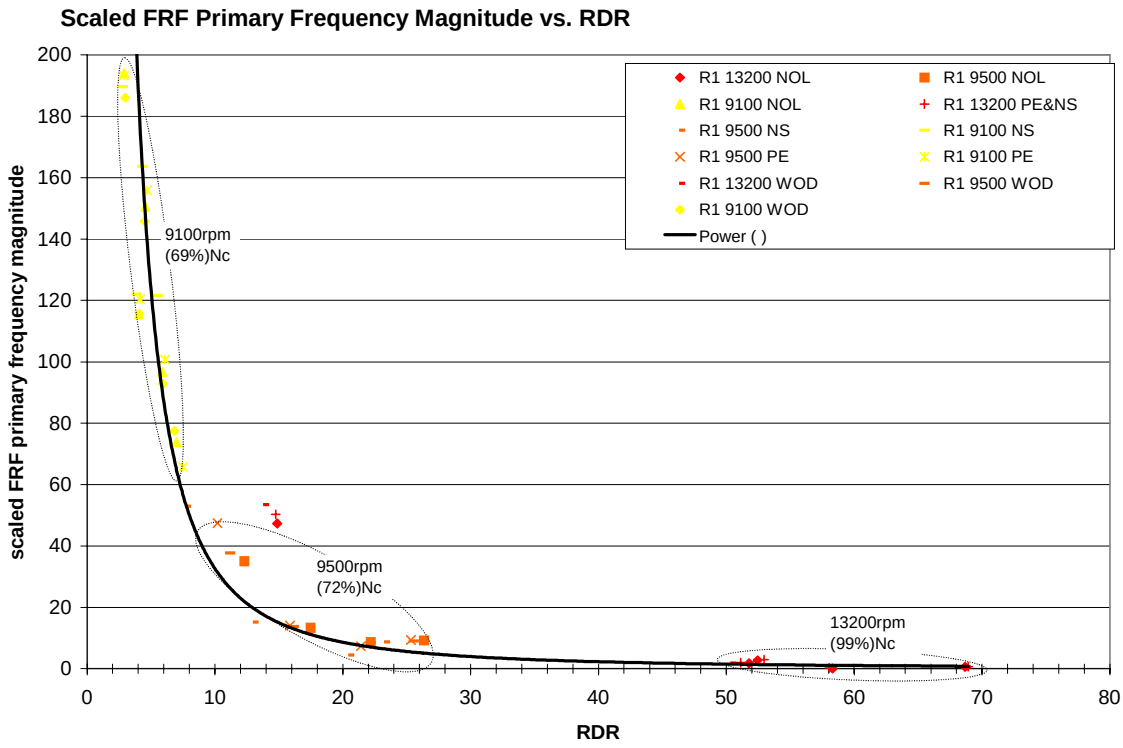

Figure 7.6: Scaled FRF Primary Frequency Magnitude vs. Reduced Frequency with Best-Fit Line, Rotor 1, Rotor Speed Indexed By Color

7.3 Tuned Frequency Response Function Model: Prediction Results

This section presents results of using the FRF tuning procedure to predict total pressure profiles downstream of the first stage rotor.

The first prediction examined is that of the 9100NOL flow condition and is representative of predictions at other mass flows along this speedline. In lieu of the time domain presentation used in chapter 6, prediction accuracy can be examined more closely by comparing tuned prediction accuracy with both measurement and untuned accuracy at individual radial positions. Thus, presented in figure 7.7 are rotor 1 exit total pressure predictions made using a tuned FRF, the corresponding experimental data and predictions made using an untuned (fundamental) FRF calculated at 9500NOL. This operating point creates the most accurate results of those from the fundamental model. Other operating conditions (such as 13200NOL) are quite poor. See section 6.7.

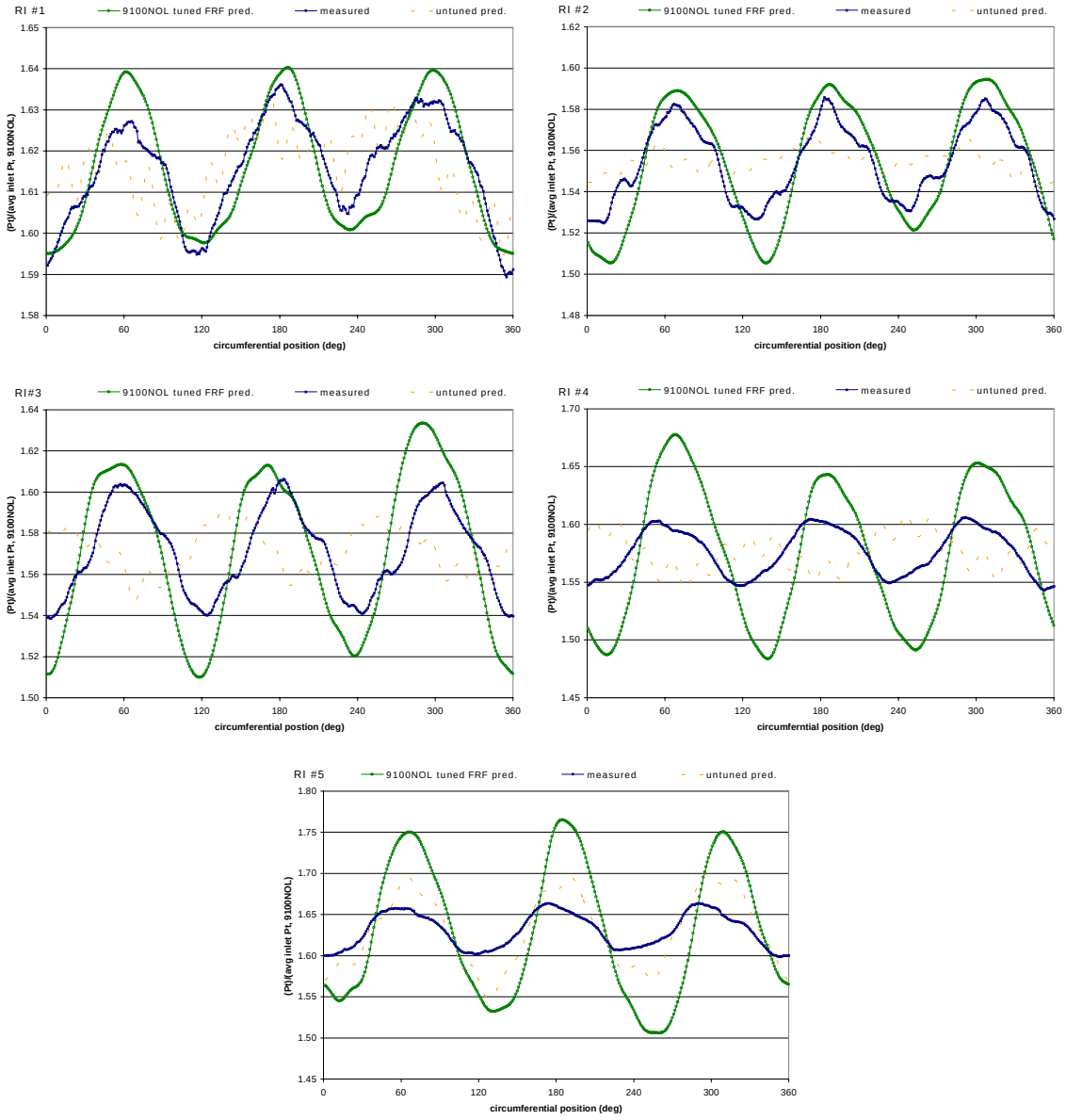

Figure 7.7: Tuned and Fundamental FRF Predictions and Measured Annular Pt Distributions, 24 Frequency Components, 5 Span Locations, R1 Exit, 9100NOL

Prediction accuracy of the tuned FRF model shows significant improvement over that of the fundamental model, especially near the tip (RI's 1 and 2). However, at radial positions near the hub the tuned model overpredicts distortion amplitude. At all radial positions, the frequency content of the tuned predictions is superior to that of the untuned

FRF. A direct comparison of tuned prediction accuracy to that of a fundamental model prediction is presented in table 7.1. The poor accuracy at locations near the hub (RI's 4, 5) is readily apparent. Comparing the table with figure 7.7, the limitation of this tabular presentation is revealed. Note that in figure 7.7, the superiority of the tuned prediction is readily apparent. However, table 7.1 indicates that the fundamental prediction is better (recall that a perfect prediction is denoted by 0.00%). While this tabular method does provide an indication of overall trends, it is imperfect.

9100NOL Prediction Accuracy: Fundamental (at 9500NOL) and Tuned FRF Models					
	RI1	RI2	RI3	RI4	RI5
tuned	0.347%	0.955%	1.571%	3.657%	5.498%
fundamental	0.239%	1.187%	0.920%	0.516%	1.989%

Table 7.1: Tuned and Fundamental Prediction Accuracy, 9100NOL

Examination of rotor exit total pressure frequency component prediction accuracy, figure 7.8, shows that most component values are over predicted. This is consistent with the time domain presentation of figure 7.7. However, scatter of component values, seen in fundamental FRF prediction plots, such as figure 6.18, has been significantly reduced.

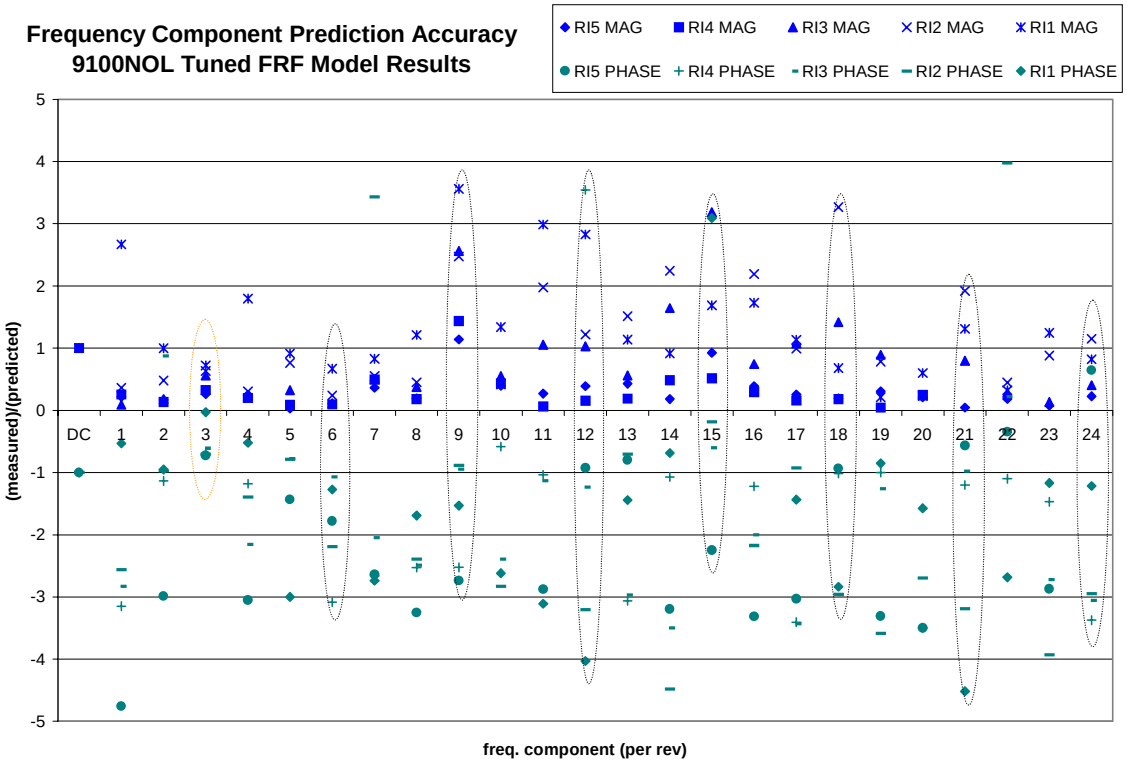

Figure 7.8: Frequency Component Prediction Accuracy, Tuned FRF Model 9100NOL

It is useful to compare the prediction ability of the tuned FRF modeling technique with that of a modern numerical method. A solution to the identical 9100NOL flow condition examined in this study was performed by Hah et al. (1996). Their numerical solution of annular total pressure distribution is compared to tuned model results at a radial position of 11.8in. (approximately part way between RI's 2 and 3) in figure 7.9. Since average total pressure is not included in the FRF prediction, each data set has been normalized by the average inlet total pressure and then vertically aligned for presentation.

Although the numerical solution more accurately predicts peak-to-peak variation of total pressure, like the FRF model, it does not capture fine details (small and medium scale undulations) in the measured data. While the accuracy of the numerical technique exceeds that of the FRF model, the resolution of the two models is equivalent. While no data from the numerical solution were available near the tip, it is expected that the accuracy of the two models in this region (where tuned FRF model prediction is best) is comparable.

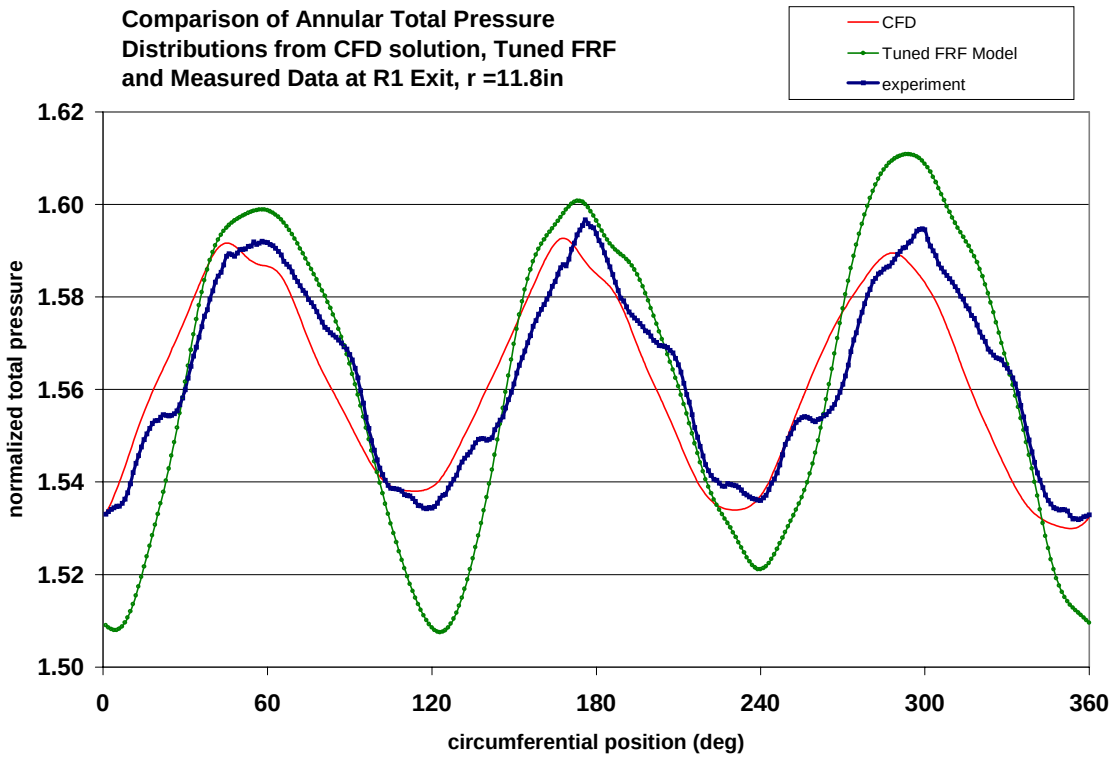

Figure 7.9: Comparison of Numerical Solution with Tuned FRF Model, R1 Exit, 9100NOL

While a phase lag is visible in the numerical solution, the FRF- based prediction is correctly phased; this is an artificial construct. The phase of the FRF prediction both in this figure and in figure 7.7 is adjusted so that results align nicely with measured data. (Recall that phase prediction is not part of the presently developed FRF model.) During FRF tuning, the phase is actually set to arbitrary values.

Although not used extensively in this work, a crude phase model can be incorporated into the tuned FRF model. The model only predicts the circumferential shift of the entire distortion pattern, therefore it assigns the same phase value to each of the FRF's component frequencies and thus does not affect the shape of the resulting downstream distribution.

The phase model is based on the rather modest assumption that the distortion pattern's phase shift through the rotor is due to the amount of time fluid particles spend in the blade row and the rotor's rotational speed. It neglects flow turning and other fluid

dynamic effects. Accordingly, the phase shift θ, in radians, is calculated using equation 7.4. Fluid velocity values for this calculation are taken from SLC solutions.

$$\theta = 2\pi \frac{\Omega l}{w_m}$$

Equation 7.4

where Ω = rotor rotational speed (rev/sec)

l = blade chord length

w_m = mean fluid velocty relative to rotor

The result of incorporating the phase model in the tuned FRF prediction of 9100NOL is presented in figure 7.10 as the green (open circle) traces. The result of setting the FRF's phase shift to zero is shown as black, broken lines. The phase model does a good job predicting the phase shift, although the prediction is lagging at RI2 and leading at RI1.

Comparing the zero phase shift data with measurement reveals that the actual phase shift is nearly constant across the span, having a value of approximately 20^0. In addition, since the model's phase shift is inherently positive in the direction of rotor rotation, these plots reveal that the circumferential measurement direction is also congruent with rotor rotation. Therefore, as seen from a blade in the rotor coordinate frame, these plots are time histories from left to right.

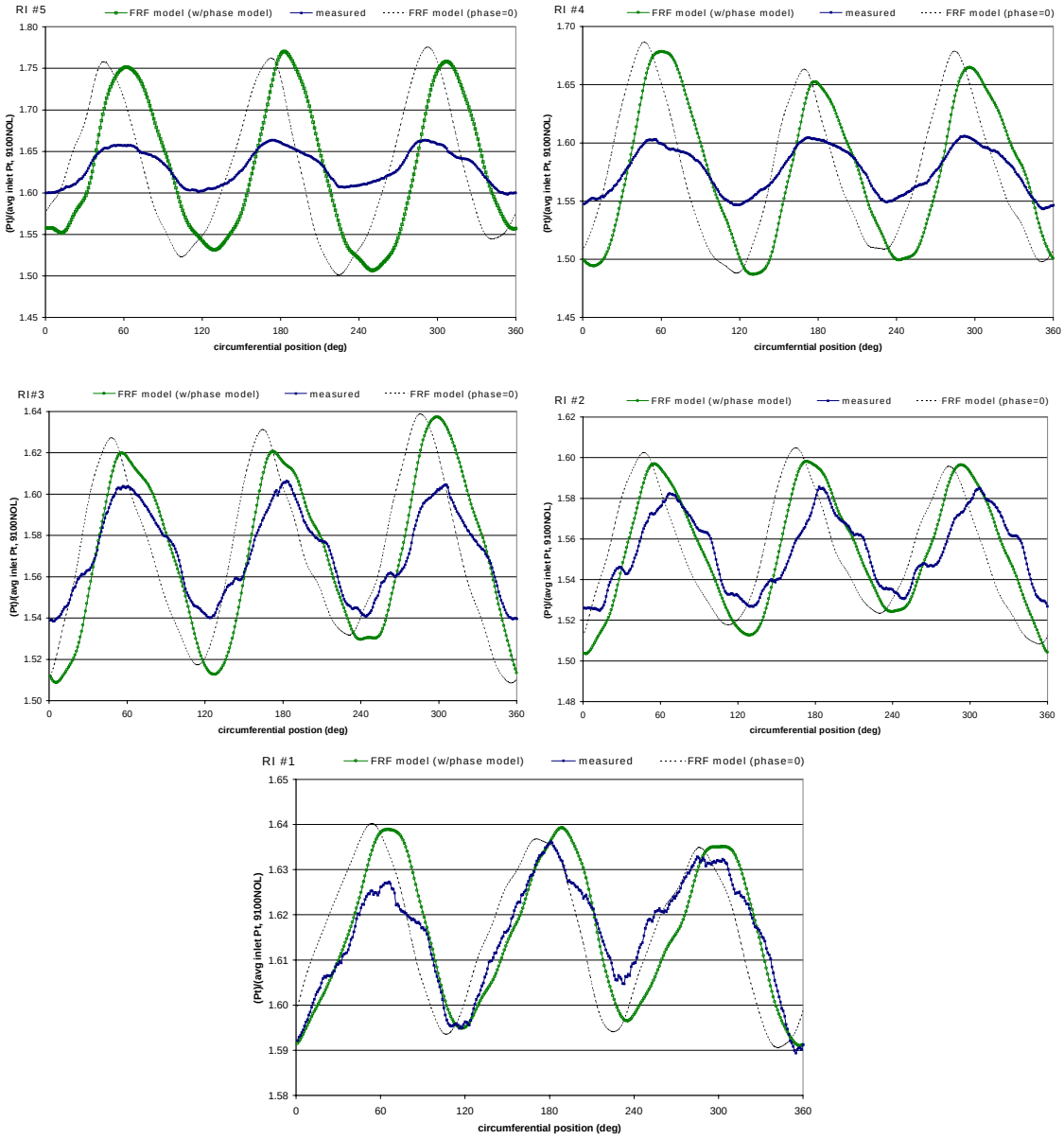

Figure 7.10: Comparison of Tuned FRF Model Results with and without an Incorporated Phase Model, R1 9100NOL

The tuned FRF model's prediction accuracy is next investigated at the 9500rpm (72%Nc) PE flow condition. Recall that this part speed condition was run with an 8/rev upstream distortion. The results of the tuned model (without a phase prediction) are compared to those of a fundamental model whose FRF was calculated at 9100PE; this is the FRF which produces the best fundamental prediction results for this case. Prediction

results are shown in figure 7.11. Results at this aerodynamic loading condition are representative of the results at other mass flows on the same 72%Nc speedline.

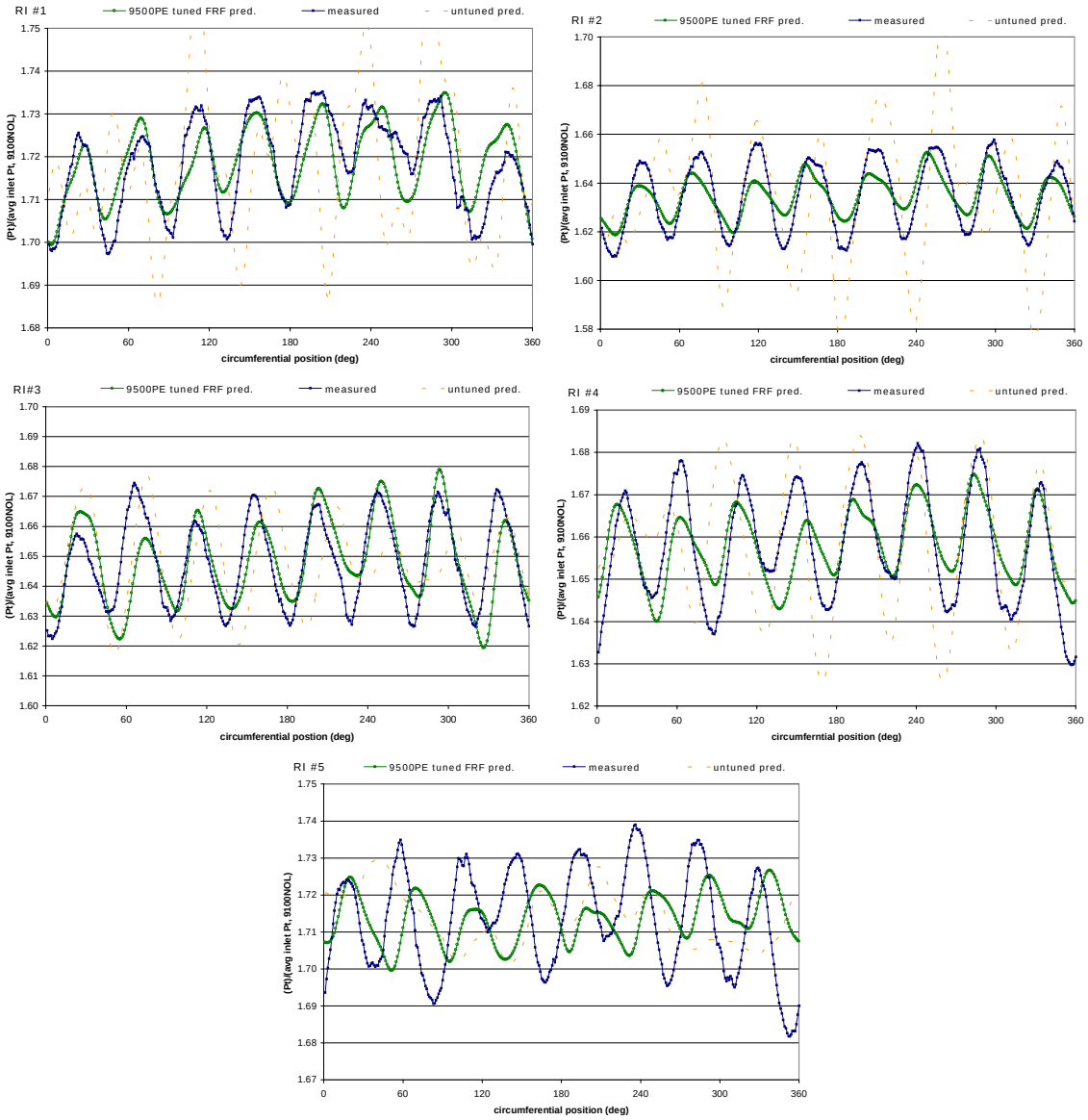

Figure 7.11: Tuned and Fundamental FRF Predictions and Measured Annular Pt Distributions, 24 Frequency Components, 5 Span Locations, R1 Exit, 9500PE

Trends seen in these results are similar to those observed for the tuned 9100NOL prediction. Tuned FRF accuracy is superior to that of the fundamental model for tip and mid-span regions (RI's 1,2 and 3), while prediction accuracy is poor near the hub.

Examination of the frequency component prediction, figure 7.12, reveals greater spanwise differences in accuracy than was seen for the tuned 9100NOL case, although like those in the previous case, few components are predicted with high accuracy.

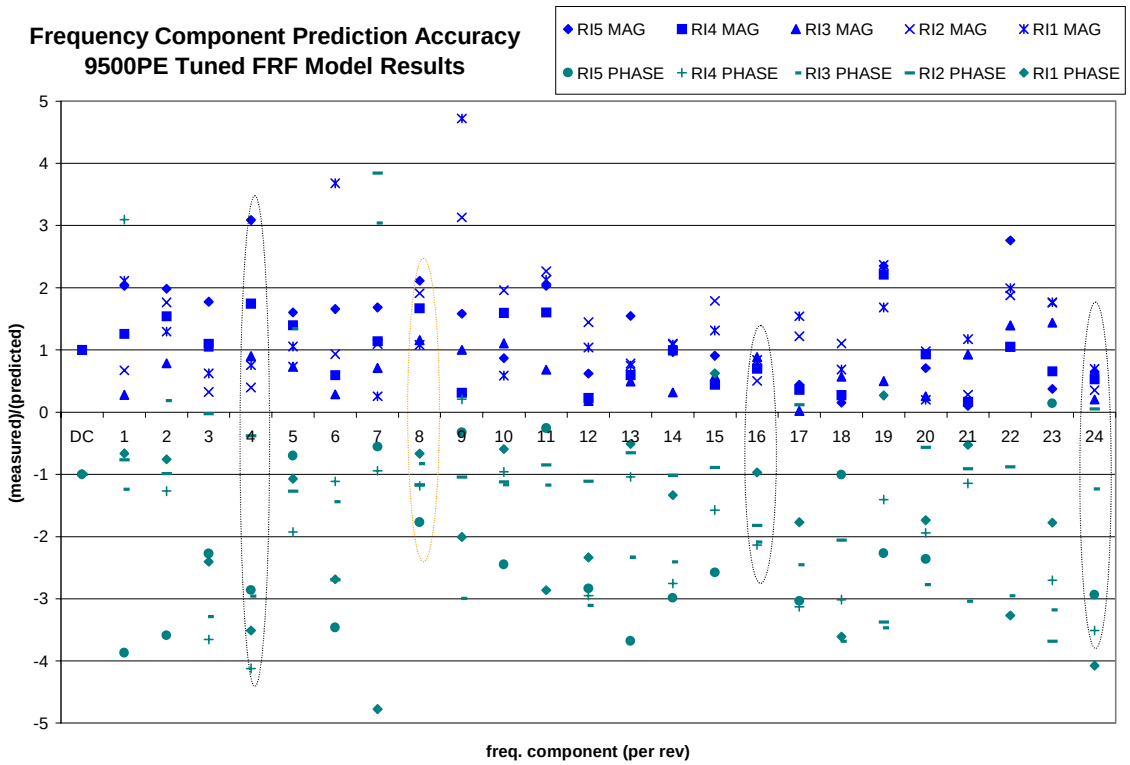

Figure 7.12: Frequency Component Prediction Accuracy, Tuned FRF Model 9500PE

7.4 Tuned Frequency Response Function Model Applied to an Alternate Rotor

Data from a different low aspect ratio rotor tested at the CRF are used to examine the sensitivity of developed empirical correlations to a specific rotor's geometry; namely the rotor with which a given set of correlations were developed. The alternate rotor, whose data are used in this section, replaces the original first- stage rotor in the CRF test compressor and is of similar blisk wide- chord design, but incorporates different blade geometry. It was tested under conditions similar to those described in chapter 3. Specific details of the rotor's design and test conditions are not available for public release.

Nonetheless, releasable results presented here indicate that fundamental flow behavior is captured in the correlation process used to create tuned FRF's.

Inlet annular total pressure distribution to the alternate rotor is very different from that of the original. Upstream distortion screens were configured to produce a two-step square wave, as shown in figure 7.13 at RI2, for an operating point near design. Peak-to-peak pressure variation is large, near 50% of average at some locations.

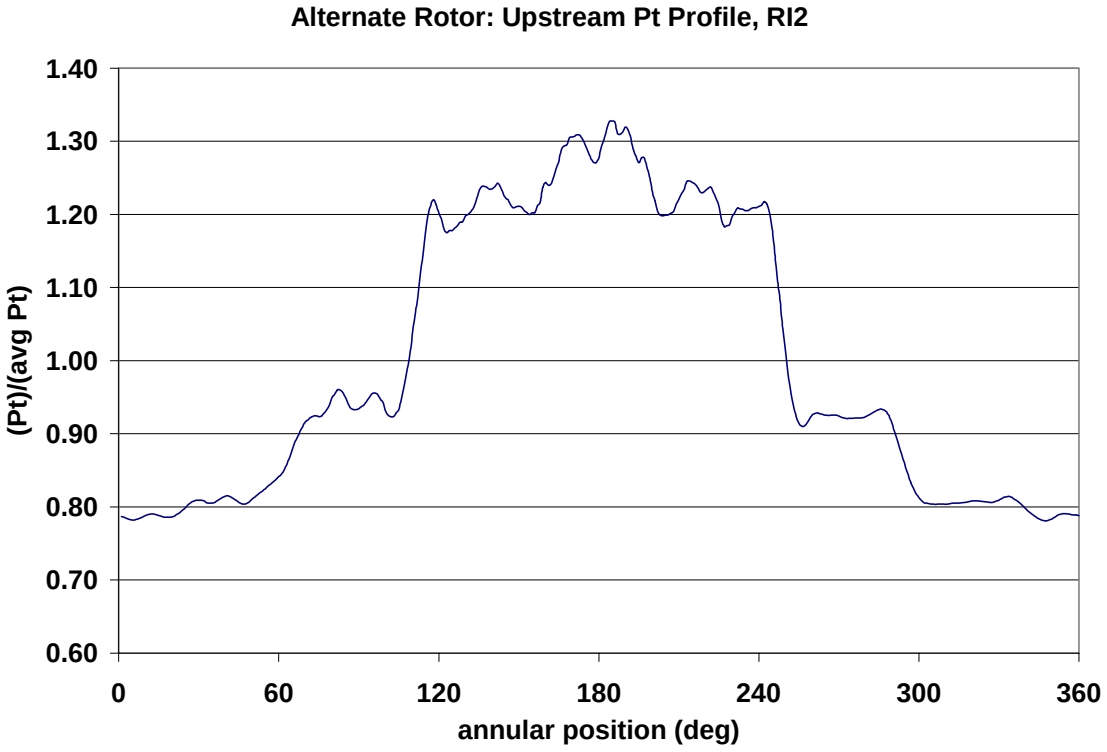

Figure 7.13: Pt Profile Upstream of Alternate Rotor at Near Design Operating Point, RI2 Span Location

In order to make predictions of total pressure downstream of this rotor, the FRF tuning procedure is calibrated using data from the original first stage rotor at 69%, 72% and 99%Nc as described in section 7.2.

Independent variables for use in the predictive mode (section 7.3) are calculated using data from the alternate rotor, albeit with a few exceptions. An SLC solution is currently not available for this rotor, which necessitates the use of the SLC solution from the original rotor to determine several flow characteristics (streamline position, fluid

velocity, shock upstream Mach number). Since the alternate rotor was run in the identical test rig at similar conditions to the original, it is reasonable to assume that streamline position and fluid velocities are alike. Additionally, since the alternate rotor was operated at similar tip speeds, relative Mach numbers are considered comparable.

A new rule for calculating the RDR parameter must be introduced when an inlet distortion profile exhibits jump discontinuities (infinite derivative), as is seen in figure 7.13. The derivative term must be confined to regions where it has a finite value. For example in this data set, derivative values calculated within approximately +/- 10^0 of the 60^0, 110^0, 250^0 and 300^0 positions were not included in the average value used to calculate RDR. Due to a limited data set, an exact rule is not developed in this work. RDR values for the alternate rotor are moderate, and fall within the range of values calculated from the original first stage rotor, figure 7.1.

Prediction results are compared to measured downstream annular total pressure distributions at a mechanical speed near design in figure 7.14. The predictions' mean values have been adjusted to match that of the measured data. Distortion profiles at each span location are predicted well, although some peaks and contours are missed. Most importantly the empirically based tuned FRF procedure, which was calibrated using higher frequency *sinusoids*, correctly predicts the downstream profile of a *square wave* input distortion. This is another indication that the FRF tuning procedure generalizes the method's prediction ability. A prediction made with the fundamental FRF method (FRF derived at 13200NOL) is juxtaposed to the tuned method is included in figure 7.14. Also mean value and phase adjusted, fundamental predictions are nonetheless very poor and- further reinforcing the conclusion in section 6.6- show that an untuned FRF developed on one rotor cannot be used for successful predictions on another.

Accurate predictions of total pressure profiles downstream of the alternate rotor using correlation factors derived from data taken on the original rotor indicate that the FRF tuning method is based on fundamental flow and rotor interactions and their resultant effects.

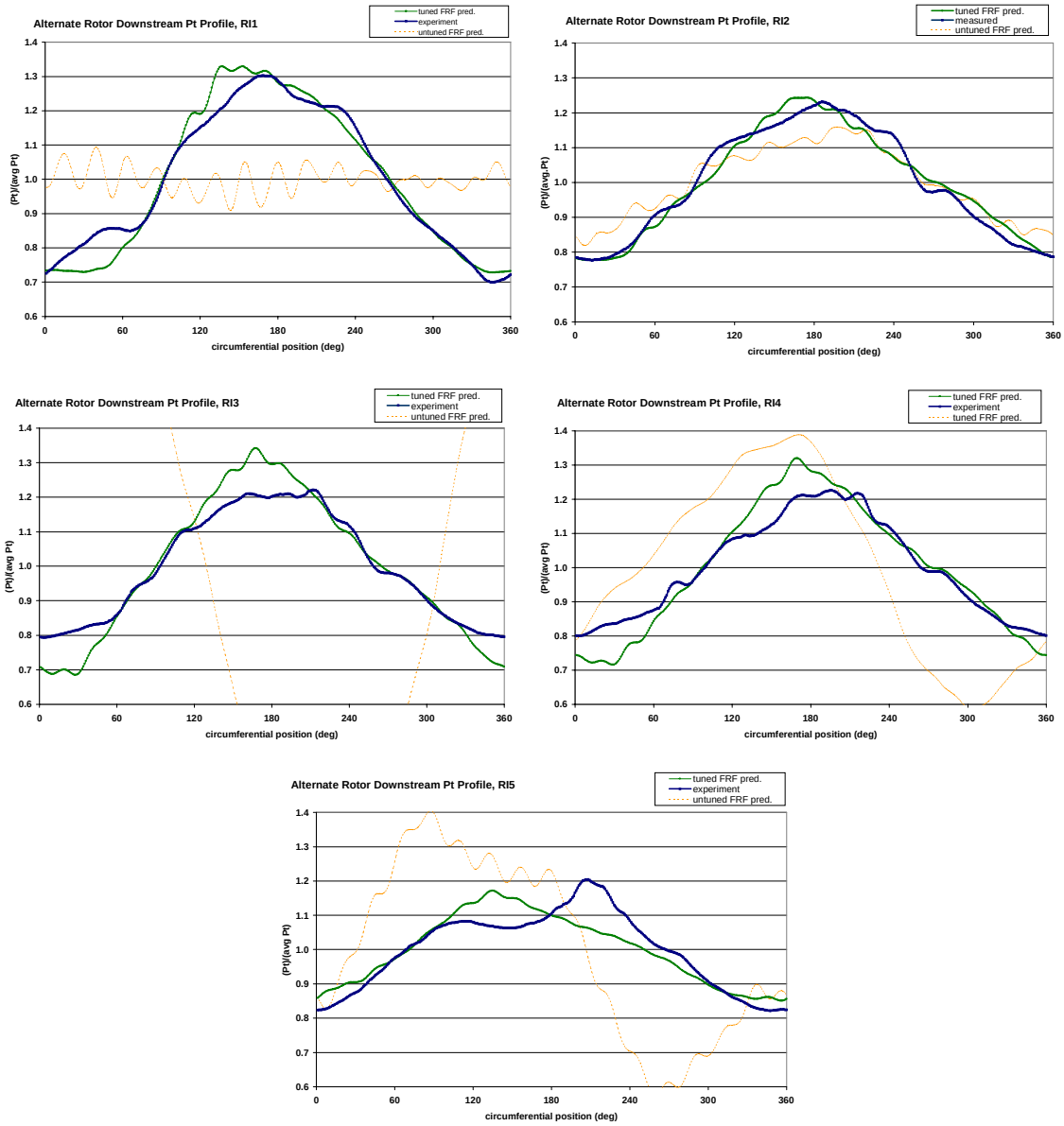

Figure 7.14: Tuned and Fundamental FRF Predictions and Measured Annular Pt Distributions, 24 Frequency Components, 5 Span Locations, Alternate Rotor Exit

8 Summary and Conclusions

The transport of nonuniform annular distributions of total pressure through a transonic axial compressor has been investigated.

Unsteady blade row fluid response at a given operating point can be captured in the frequency domain with a frequency response function.

Fundamental (untuned) FRF's provide good predictions of total pressure transport for small changes in flow conditions away from those at which they were derived. Predictions of rotor exit distortion patterns along a single speed line with similar upstream nonuniformities are very accurate.

Due to the inherent non-linearity of compressor behavior, prediction accuracy was generally poor for conditions further removed from those at which the untuned FRF was derived.

Study of the results led to the observation that the amplitude of the input frequency components were being processed in a manner dependent on the local rate of change of the input distortion and the computed transit time for a convected disturbance through the rotor. A new flow descriptor, the RDR, was defined to characterize this relationship.

A non-linear tuning method was developed that allows an FRF to be calculated that predicts total pressure annular distribution at the rotor exit for a given inlet condition. Best predictive capabilities using the tuned FRF are above 50% span. The method demonstrated the capability of being derived using data from one rotor and making accurate predictions of the flow behavior of another rotor.

Prediction accuracy is expected to improve with a larger baseline data set. Having data from only three distinct operating conditions required tuning the non-linear correlations with two of the three cases, while testing prediction accuracy with the third. The ability of the technique to produce good results when calibrated with only two test conditions is considered promising.

Specific results and conclusions of this study are as follows.

Experimental Data

- Stationary annular total pressure profiles are seen as time histories in the rotor coordinate frame and these discrete, time domain functions can be Fourier Transformed into the frequency domain.
- The amplification or attenuation of the frequency component with the greatest magnitude- the primary frequency- is seen to be strongly dependent on rotor speed and span position, and weakly dependent on blade aerodynamic loading.
- Frequency component magnitudes of the investigated data (with low engine order distortions) typically decay to approximately 2% of the primary frequency magnitude between the 20^{th} and 30^{th} component.
- Limited by Nyquist sampling theory, circumferential data resolution must be such that the equivalent sampling rate in the rotor coordinate frame is at least twice as great as the highest significant frequency component of the distortion. The novel data acquisition method described by Williams (1999), and used in this study, can provide sufficient resolution for disturbances containing very high engine order (on the order of 100/rev).

Frequency Response Functions

- A frequency response function can be calculated by regarding annular total pressure distributions upstream and downstream of the rotor as forcing and response functions, respectively.
- A given frequency response function fully describes rotor transport of total pressure for the flow condition at which it was calculated.
- A fundamental model of total pressure transport through a rotor can be constructed by forcing a previously calculated FRF with an upstream annular total pressure distribution. The output of the FRF is a prediction of the pressure distribution at the rotor's exit.

- The FRF model of compressor behavior is akin to considering the compressor as an analogous digital (due to the discrete upstream and downstream data sets) electronic filter, whose DC offset corresponds to the compressor's pressure ratio. Other frequency components are amplified, attenuated and phase shifted by the compressor just as they would be by an equivalent electronic filter.
- The application of the inherently linear FRF modeling technique to data from an advanced transonic compressor show that accurate predictions of rotor downstream total pressure can be made for other mass flow (aerodynamic loading) points along the same speedline on which the FRF model is calculated.
- Prediction accuracy at rotor speeds and distortion types other than those at which the FRF was calculated is poor. Specifically, the ability of a given FRF to predict flow behavior at conditions other than that at which it was calculated has the following levels of dependence:

    - very weakly dependent on blade row aerodynamic loading
    - strongly dependent on rotor speed
    - strongly dependent on distortion frequency and intensity
    - very strongly dependent on rotor (FRF's can't be used for a different rotor than the one they were calculated across)

- FRF models can be staged, just as their equivalent compressor components are staged, to allow the prediction of flow transport through several stages of compression. In this configuration, the output of an upstream FRF is the input to the corresponding downstream FRF.

Tuned Frequency Response Function Models

- An empirically- based nonlinear method has been developed that improves FRF rotor exit total pressure distribution predictions for dissimilar flow

conditions. The method adjusts individual FRF component frequency magnitudes.

- As a consequence of developing this tuning method, a turbomachinery rotor's FRF was found to be a function of primarily the following five parameters:

    - distortion intensity
    - rate of change in total pressure as seen by the blade row
    - blade passage shock strength
    - fluid axial velocity
    - blade chord length

- A new distortion descriptor, the RDR, was developed for use with the FRF tuning procedure. It was found that the RDR is superior to the reduced frequency for use in the presently developed model. This is attributed to the inclusion of the rate of change of total pressure in RDR.
- Using mean circumferential values, an axisymmetric flow solver, based on streamline curvature methods, was successfully used to determine flow properties (streamline position, blade passage Mach numbers and flow velocities) for integration into the FRF tuning procedure.
- Prediction accuracy of the tuned FRF model is best near the tip, with distortion amplitude commonly over predicted near the hub.
- Mean pressure and phasing are not included in the tuned approach. A crude phase model is presented, and when incorporated into the FRF method, results are reasonably accurate.
- Good prediction results are observed from the tuned FRF method, even though only two data sets were available at each prediction to calibrate the method's highly nonlinear correlations, indicating the robustness of the approach.
- Comparison with a state of the art numerical solution reveals greater accuracy is achieved (at the considered span location) with the numerical model. However, the resolution of the distortion profile predicted by both methods is

similar, suggesting that the less complex FRF model captures at least as much frequency content as the CFD code.

- Successful prediction of pressure distributions downstream of an alternate rotor using the tuning correlations calibrated with data from the original rotor indicate that fundamental distorted flow behavior is captured by these correlations.

Applicability to High Cycle Fatigue

- It is demonstrated that FRF- based modeling methods can successfully predict transport of total pressure nonuniformities through compressor rotors. Thus, possible downstream forcing functions can be characterized.
- The frequency magnitude portion of the FRF quantifies the amplification or attenuation of individual frequency components (each a potential HCF driver) through a given rotor.
- Although developed using data with only low engine order disturbances, the FRF tuning method is not inherently limited to these low frequencies.

9 Recommendations

This study investigates frequency domain methods of predicting compressor flow behavior and develops several original modeling techniques; consequently producing numerous topics for possible future work.

Specific recommendations include the following.

- Repeat tuned FRF correlation development with a larger data set to fully investigate the behavior of scaled primary frequency magnitude vs. RDR. Sufficient investigation may lead to improved correlation parameters and will further validate the procedure.
- Define and implement a test program that would allow the characterization of a given rotor with the minimum combination of distortion types, flow and rotor conditions. This is equivalent to testing the rotor over a wide range of RDR. Distortion screen design is important here, since it (along with rotor speed) determines the rate of change, as seen by the blade row, of upstream total pressure.
- More fully investigate the phase portion of the FRF to determine if rules governing the tuning of individual phase components can be created. This would improve the profile of the resulting prediction, allowing it to better capture subtle undulations.
- Develop a specific rule for calculating the RDR of distortion profiles with jump discontinuities.
- Incorporate a method of predicting the average total pressure (zeroth frequency component) into the tuned FRF method.
- Improve the empirically based correlation for non-primary FRF component frequencies so that it more strongly generalizes flow behavior for dissimilar conditions.
- Develop an improved method of characterizing prediction accuracy in the time domain.

10 Works Cited

Adamczyk, J.J., "Unsteady Fluid Dynamic Response of an Isolated Rotor with Distorted Inflow," AIAA Paper No. 74-49.

Andrew, P.L,"An Experimental Investigation of Unsteady Loss Variation with Reduced Frequency in a Low Speed , Single Stage Axial Compressor," Von Karmen Institute for Fluid Dynamics, Project Report 1988-07, June 1988

Ashby Jr., G.C., "Investigation of the Effect of Velocity Diagram on Inlet Total-Pressure Distortions Through Single-Stage Subsonic Axial-Flow Compressors", NACA RM L57A03

Barr, L.C., "The Unsteady Response of an Axial Flow Turbomachinery Rotor to Inlet Flow Distortions", The Pennsylvania State University Applied Research Laboratory, TM 78-253

Boller, S.M., "One-Dimensional Dynamic Wake Response in an Isolated Rotor Due to Inlet Total Pressure Distortion," M.S. Thesis, Virginia Polytechnic Institute & State University, Blacksburg, Virginia, 1998.

Boyer, K.E., "An Improved Streamline Curvature Approach for Off-Design Analysis of Transonic Compression Systems," Ph.D. Dissertation, Virginia Polytechnic Institute & State University, Blacksburg, Virginia, 2001.

Boyer, K.E., private communication, 2000

Braithwaite, W.M., Graber Jr., E.J., Mehalic, C.M., "The Effect of Inlet Temperature and Pressure Distortion on Turbojet Performance." AIAA Paper No. 73-1316, AIAA/SAE 9th Propulsion Conference, November 5-7, 1973, Las Vegas, Nevada.

Carta, F.O., "Analysis of Unsteady Aerodynamic Effects on Axial Flow Compressor Stage with Distorted Inflow." Project Squid – Technical Rep. UARL – A – UP, 1972.

Colpin, J., Kool, P. "Experimental Study of an Axial Compressor Rotor Transfer Function with Non-Uniform Inlet Flow." ASME Paper No. 78-GT-69, Gas Turbine Conference and Products Show, April 9-13, 1978 London, England.

Cousins, W.T., O'Brien, W.F., "Axial-Flow Compressor Stage Post-Stall Analysis," AIAA Paper No. 85-1349, 1985.

Danforth, C.E., "Distortion- Induced Vibration in Fan and Compressor Blading," Journal of Aircraft, Vol. 12, No. 4, pp. 216-225, April 1975.

Datko Jr., J.T., O'Hara, J.A.,"The Aeromechanical Response of an Advanced Transonic Compressor to Inlet Distortion," ASME 87-GT-189, 1987.

Fleeter, S., Jay, R.L., Bennett, W.A., "Rotor Wake Generated Unsteady Aerodynamic Response of a Compressor Stator," ASME 78-GT-112, 1978.

Graber Jr., E.J.,Braithwaite, W.M., "Summary of Recent Investigations of Inlet Flow Distortion Effects on Engine Stability," AIAA Paper 74-236, AIAA 12th Aerospace Sciences Meeting, January 30-February 14, 1974, Washington, D.C.

Greitzer, E.M.,"Upstream Attenuation and Quasi-Steady Rotor Lift Fluctuations in Asymmetric Flows in Axial Compressors," ASME 73-GT-30, 1973.

Greitzer, E.M., Tan, C.S.,Wisler, D.C., Adamczyk, J.J.,Stazisar, A.J., "Unsteady Flows in Turbomachines: Where's the Beef?," ASME Unsteady Flows in Aeropropulsion, 1994, pp.1-11.

Hah, C., Rabe, D.C., Sulliavan, T.J., Wadia, A.R., "Effects of Inlet Distortion on the Flow Field in a Transonic Compressor Rotor," *ASME Journal of Turbomachinery*, Vol.120, April 1998, pp.233-246.

Henderson, R.E., Shen, I.C. "The Influence of Unsteady Rotor Response on a Distorted Flow Field." ASME Paper No. 81-GT-185, International Gas Turbine Conference and Products Show, March 9-12, 1981 Houston, Texas.

Howard, J.S., "Improved Methods for Modeling Dynamic Stage Characteristics," M.S. Thesis, Virginia Polytechnic Institute & State University, Blacksburg, Virginia, 1999.

Hurad, J., "Determination Experimentale des Lois de Transfert de Perturbations a la Traversee d'un Compresseur Axial," AGARD CP-400, 68th Specialists Meeting, September 8-9, 1986, Munich, Germany.

Kaya,T., Carrere, A., Barenes, R.,"Investigation of the Flow Field Through a Variable Pitch Fan Rotor with an Inlet Total Pressure Distortion," ISABE 93-7029, 1993.

Kimzey, W.F. "An Analysis of the Influence of Some External Disturbances on the Aerodynamic Stability of Turbine Engine Axial Flow Fans and Compressors." AEDC-TR-77-80, August 1977.

Lecht, M., "Improvement of the Parallel Compressor Model by Consideration of Unsteady Blade Aerodynamics," AGARD CP-400, 1986.

Longley, J.P., Greitzer, E.M., "Inlet Distortion Effects in Aircraft Propulsion System Integration," AGARD LS-183, *Steady and Transient Performance Prediction of Gas Turbine Engines*, May 1992.

Ludwig, G.R., "Aeroelastic Considerations in the Measurement of Inlet Distortion," 4th National Turbine Engine High Cycle Fatigue Conference, 1999, Monterey, CA.

Manwaring, S.R., Fleeter, S., "Inlet Distortion Generated Periodic Aerodynamic Rotor Response," ASME 89-GT-299, 1989.

Manwaring, S.R., Fleeter, S., "Forcing Function Effects on Rotor Periodic Aerodynamic Response," *Transactions of the ASME*, Vol. 113, April 1991, pp.312-319.

Manwaring, S.R., Rabe, D.C., Lorence, C.B., Wadia, A.R., "Inlet Distortion Generated Forced Response of a Low Aspect-Ratio Transonic Fan," *ASME Journal of Turbomachinery*, Vol. 119, October, 1997, pp.665-676.

Mazzawy, R.S. "Multiple Segment Parallel Compressor Model for Circumferential Flow Distortion." *ASME Journal of Engineering for Power*, April, 1977.

Melick, H.C., "Analysis of Inlet Flow Distortion and Turbulence Effects on Compressor Stability." NASA CR 114577, 1973.

Mikolajczak, A.A., Pfeffer, A.M., "Methods to Increase Engine Stability and Tolerance to Distortion," AGARD LS No. 72, Sect. 7, 1974.

Mokelke, H., "Prediction Techniques," AGARD LS No. 72, Sect. 5, 1974.

Nagano, S., Takata, H., "Nonlinear Analysis of Rotating Stall," Institute of Space and Aeronautical Science, University of Toyko, Report No. 449, 1970.

Novack, R.A., "Streamline Curvature Computing Procedures for Fluid-Flow Problems," *Transactions of the ASME, Journal of Engineering for Power*, October 1967, pp.478-490.

Peacock, R.E., Overli, J., "Dynamic Flows in Compressors with Pressure Maldistributed Inlet Conditions," AGARD CP-177, 1976.

Pearson, H., McKenzie, A., "Wakes in Axial Compressors." *Journal of the Royal Aeronautical Society*, Vol. 63, July, 1959.

Rabe, D., Bolcs, A., Russler, P., "Influence of Inlet Distortion on Transonic Compressor Blade Loading," AIAA 95-2461, Presented at the 31st Joint Propulsion Conference and Exhibit, July 10-12, 1995, San Diego, CA

Rabe, D.C., Williams, C., Hah, C., "Inlet Flow Distortion and Unsteady Blade Response in a Transonic Axial-Compressor Rotor," ISABE 99-7297, 1999.

Reid, C. "The Response of Axial Flow Compressors to Intake Flow Distortion." ASME Paper No. 69-GT-29, 1969.

Roberts, F., Plourde, G.A., Smakula, F. "Insights into Axial Compressor Response to Distortion." AIAA Paper No. 68-565, 1968.

SAE Aerospace Information Report, AIR-1420. "Inlet Total-Pressure-Distortion Considerations for Gas-Turbine Engines," Rev. A, 1999.

Schwartz, J.R., "An Experimental and Analytical Investigation of Dynamic Flow Response of a Fan Rotor with Distorted Inlet Flow," M.S. Thesis, Virginia Polytechnic Institute & State University, Blacksburg, Virginia, 1999.

Sexton, M.R.,O'Brien, W.F., "A Model for Dynamic Loss Response in Axial-Flow Compressors," ASME Paper 81-GT-154, 1981.

Smith, S.W., The Scientist and Engineer's Guide to Digital Signal Processing, 2nd ed., California Technical Publishing, 1999.

Williams, C., "Turbine Engine Research Center Inlet Distortion Measurement," 4th National Turbine Engine High Cycle Fatigue Conference, 1999, Monterey, CA

Williams, C., private communication, 2000

Yocum, A.M., Henderson, R.E., "The Effects of Some Design Parameters of an Isolated Rotor on Inlet Flow Distortions," *Transactions of the ASME*, Vol. 102, January, 1980, pp.178-186.

VITA

Matthew D. Small

The author, son of David and Janet Small, was born in 1977 in Portland, Maine as a May snowstorm was gathering strength over the nearby Atlantic Ocean. He grew up in South Berwick, Maine and subsequently attended St. Thomas Aquinas High School in Dover, New Hampshire. He then enrolled at the University of Maine, where he was a member of Pi Tau Sigma and Tau Beta Pi and graduated *summa cum laude* with a B.S. in Mechanical Engineering in 1999. During several summer breaks he worked as an intern at Pratt & Whitney in North Berwick, Maine and AlliedSignal Aerospace in Phoenix, Arizona. In the fall of 1999, he began graduate studies in Mechanical Engineering at Virginia Tech. He is a registered Engineer-in-Training in the State of Maine. Upon graduation, he will begin employment at Pratt & Whitney in East Hartford, Connecticut.